Università degli Studi di Cagliari

PHD DEGREE

Cycle XXXIII

Atomistic investigation of conjugated polymers for thermoelectric applications: from morphology to transport properties

Scientific Disciplinary Sector:
FIS03

PhD student: Antonio Cappai

Coordinator of the PhD program: Prof. Paolo Ruggerone

Supervisor: Prof. Claudio Melis

Final exam. Academic Year 2019/2020
Thesis defence: February 2021 Session

Abstract

Two centuries after its first discovery, thermoelectricity, i.e. the phenomenon of direct conversion of thermal power into electrical power, has only recently reached the possibility of implementation in a vast number of practical applications.

This breakthrough was undoubtedly determined by the advent and diffusion of numerical atomistic simulation techniques, allowing a quick survey of large classes of materials as possible candidates for the realization of active parts for thermoelectric generators.

To this aim, two classes of materials have been essentially identified, (I) inorganic thermoelectrics, based on metal alloys, and (II) organic conductive polymers. The latter ones are well suited for implementation in a large-scale economy because of their superior mechanical properties, such as flexibility and low specific weight, as well as simpler synthesis process, as spin coating, and the possibility of tuning the electrical conductivity through chemical doping.

Among the most common conducting polymers, polyethylenedioxythiophene (PEDOT), the subject of this Thesis work, has clearly emerged as one of the most promising thermoelectric material.

Despite its wide use, however, an unanimous and well-established understanding of the link existing between the synthesis process and the corresponding final thermoelectric properties is still missing and it is thus an active field of scientific investigation.

The present Thesis represents a part of this research stream, specifically aiming to shed a light on the role and effect of the combinations of most commonly used polymerizing reagents for PEDOT in determining the micromorphology and the resulting thermal and electrical transport properties. In this respect, the description and development of a new computational algorithm, based on a multiscale approach, is presented, combining a purely quantum description based on the Density Functional Theory (DFT) with Classical Molecular Dynamics (MD).

The comparison of the results obtained by numerical simulation with the experimental data currently available demonstrates the effective possibility of including the chemical description of the synthesis process in the context of an MD simulation, and allows to demonstrate and quantify the impact of the combination of reagents used on (i) micromorphological properties, such as chain length distribution and crystallinity, (ii) thermal transport properties, in particular thermal conductivity, and (iii) carrier transport properties, mainly hole mobility and conductivity, estimated by Marcus' theory of electron transport.

La presente tesi è stata prodotta durante la frequenza del corso di dottorato in Fisica dell'Università degli Studi di Cagliari, XXXIII ciclo, con il supporto di una borsa di studio finanziata con le risorse del P.O.R. Sardegna F.S.E. 2014-2020 - Asse III "Istruzione e Formazione" - Obiettivo Tematico 10, Priorità d'investimento 10ii), Obiettivo Specifico 10.5, Azione dell'accordo di Partenariato 10.5.12.

Antonio Cappai gratefully acknowledges Sardinian Regional Government for the financial support of his PhD scholarship (P.O.R. Sardegna F.S.E. - Operational Programme of the Autonomous Region of Sardinia, European Social Fund 2014-2020 - Axis III Education and training, Thematic goal 10, Investment Priority 10ii), Specific goal 10.5.

Contents

Chapter 1

Introduction

Since 1977, when iodine-doped polyacetylene was first synthesised,[4] interest in conjugated polymers and small-molecule organic materials for electronic and optoelectronic devices has grown exponentially with a large number of research lines set up in order to synthesise new more suitable materials and improve the existent ones.

Organic polymers are currently extensively studied as building blocks for a large number of electronic devices, such as capacitors,[28] photovoltaic cells,[37] OLEDs[2] and thermoelectric generators.[30]

All the electronic and optical properties of organic polymers basically rely on the conjugation length of the constitutive carbon backbone. In other words, the fact that carbon atoms which constitute the underlying common structure of organic polymers' chains can be considered as alternatively bound together by single and double bonds. This topological feature provides a significant $\pi - \pi$ overlap, allowing an sizable delocalisation of electrons occupying the corresponding energy levels.[7,18] This chemical feature allows to better control both transport and optical properties with respect to systems characterized by localized σ bonds.[22]

Among organic polymers, poly(3,4-ethylenedioxythiophene) (PEDOT) has emerged as one of the most promising one. First synthesized in 1988,[34] it has been found to be one of the most promising material for technological applications because of its high stability at relatively high temperature (since it can be synthesised and resist even for 6 hours in boiling benzonitrile, $\simeq$ 188°C[8]) and in presence of humidity,[33] a tunable band gap,[21] low redox potential[39] and good optical properties in the visible spectrum.[27]

PEDOT's applications cover nowadays a large class of devices[23] and it has

been proposed as the active part of thermoelectric generators,[1,14,20] which are at the centre of our attention.

Besides a pure academic interest, in fact, the realization of efficient thermoelectric devices could be strategical in the ongoing search of large available and low-cost sources of energy.

Heat is in fact the final form in which all types of energies convert at the end of any production process of electrical power. For this reason, thermal energy is available in large amounts therefore any efficient process of conversion of heat in electricity can potentially have an enormous impact in the world energy scenario.

In this perspective, thermoelectricity could provide a valuable strategy to (i) increase conversion efficiency of existing power plants and (ii) to successfully exploit the waste heat produced by green technologies, as photovoltaic or geothermal sources.

Even if direct heat to electrical power conversion is generally characterised by a poor efficiency, several research lines were set up and are actually active in order to (i) realise new materials and ii) optimize the thermoelectric properties of the existing ones.

Energy conversion efficiency of heat into electricity is evaluated by means of the *figure-of-merit* ZT, an adimensional parameter first introduced in 1949 by the Soviet physicist Abram F. Ioffe[32] in terms of the operating temperature T, the electrical conductivity σ, the Seebeck coefficient S and the thermal conductivity κ

$$ZT = \frac{S\sigma}{\kappa}T \tag{1.1}$$

In order to maximise the figure-of-merit, a electrical conductors are needed which, at the same time, should be thermal insulators i.e have a low thermal conductivity. Unfortunately, the most common natural materials which are good or bad electrical conductors are, respectively, also good or bad thermal conductors. For this reason, the figure-of-merit is thus generally so small that no useful applications for thermoelectricity have been proposed for a few of decades since thermoelectricity discovery.

The ability of fine tuning electronic density by physical or chemical doping, however, has lead to a new interest in thermoelectricity research: a whole class of materials, organic polymers, has emerged as one of the most probable candidates for thermoelectric devices realisation.

Organic polymers, as PEDOT, show a very low thermal conductivity ($\sim 0.5 - 1\text{W m}^{-1}\text{ K}^{-1}$ [31]) at the same time they exhibit an electrical conductivity which can be chemically tuned by doping in order to make them semi-metallic or almost metallic.[17] ZT can thus increase in order to make

possible many practical applications, which, in the case of PEDOT and its derivatives, are particularly explored since their synthesis appears to be less complicated with respect to different conjugated polymers. This had lead to PEDOT employ in the realization of transport layers[38] and hole injection interfaces[5] for electronic devices.

Several research projects have been set up and are still active with the goal of developing the best procedure to further enhance ZT. In fact, even if σ can be easily increased by increasing the carrier concentration by doping, several studies,[13,29] have found that the S Seebeck coefficient shows an antagonist behaviour with respect σ. Changes induced by free carrier concentration seems detrimental for S.

A weak dependence of S from carrier mobility, $S \propto \mu^{0.2}$, has been reported.[29] For this reason, since conductivity can be expressed as a product of mobility μ, carrier charge q and carrier density n

$$\sigma = n\mu q \tag{1.2}$$

a possible strategy to enhance Seebeck coefficient, once a proper n value is fixed by doping, consists in increasing mobility.

This can be achieved by controlling the chain length and the morphology of the film. Large chain lengths are related to an improved charge mobility[3] affecting both inter-chain and intra-chain hopping. While intra-chain mobility is largely affected by π orbitals delocalisation along the polymer backbone, intra-chain mobility is enhanced when $\pi - \pi^*$ stacking between different chains is largely favoured, a mechanism which can be usually explained by invoking a percolation-like behaviour of charge carriers.[10] Since intra-chain hopping has been found to be one order of magnitude greater than inter-chain one,[26] the creation of a proper number of percolation paths is crucial in order to assure a sufficiently high conductivity.

In both cases, interest in polymerisation mechanism should be emphasised: the way by which PEDOT chains are formed, in fact, deeply influences the morphology of the films and consequently the values of S and σ. An accurate knowledge of this mechanism can thus lead to further investigations on novel synthesis techniques allowing to achieve higher chain lengths and a large number of percolation paths. This condition will definitely guarantee a concurrent σ and S increase.

In order to better understand how synthesis and polymerisation take place, a general overview of the main methods used to synthesize PEDOT is reported.

1.1 PEDOT polymerization

PEDOT is usually synthesised in form of thin bluish films characterised by a high conductivity[9, 24, 35] which have been proved[9, 15] to rapidly vary during accretion (i.e. polymerization), suggesting that the film formation can be regarded as a process in which first the EDOT monomers polymerize in PEDOT chains which eventually, by coalescence, connect with each other in a network.[9]

Four main polymerisation techniques are reported in literature[24] in order to grow PEDOT films: Chemical polymerisation (CP), electrochemical polymerisation, Vapour Phase polymerisation (VPP) and oxidative Chemical Vapor Deposition (CVD).

These techniques mainly differs in the environment in which polymerisation reaction takes place. In CP, all the chemicals involved are in solution. Since EDOT and PEDOT show a very low solubility in water, hydrophilic counterions, such as PSS, are usually added in order to obtain a stable suspension. The presence of PSS determines an appreciable modifications of the film morphology, which appears to have a granular structure:[24] each grain is formed by an inner PEDOT core, formed by charged (doped) PEDOT chains, surrounded by an external PSS shell counterbalancing all internal charge, a configuration which is usually referred to as *phase-segregated*.

Even if other counterions can be used in place of PSS, such as tosylate anions, MD simulations seems to suggest that this structure can be observed even in these cases.[10]

Solvents (such as water or acetonitrile) are also involved in EP technique, which significantly differs from CP because oxidative reactions are driven by a metallic anode which provides the electron subtraction. In this case, the morphology is affected by the electrical connections of PEDOT chains with the electrode giving rise to a dendritic-like structure instead of a granular one.[24]

In VPP and CVD, monomeric EDOT units are not in contact with the oxidising agent directly in solution which is instead vaporised in a vacuum chamber on a substrate. The most used oxidising agents are iron(III) salts, as $FeCl_3$ or iron(III)tosylate which can both deposited on the substrate (VPP) or vaporised on it (CVD). The second choice is reported to bring to thicker films formation.[24]

Besides the involved technique, PEDOT polymerisation is essentially oxidative, following the general reaction scheme

$$HX_{n\text{-}1}H^+ + HXH^+ + B + B' \rightleftharpoons HX_nH + BH + BH' \qquad (1.3)$$

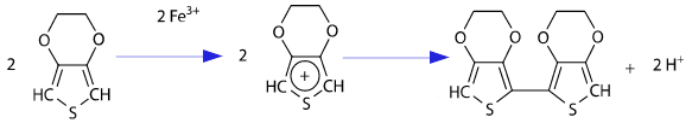

Figure 1.1: Fundamental steps of the chemical pathway for EDOT polymerisation. Iron(III) cations provide initial EDOT units charging.

where HX_nH stands for the olygomer containing n monomeric units (reducing to the monomer itself for n=1) and B, B' for the chemical species acting as collectors of terminal hydrogen removed to create a new bond.

The process as reported in literature[8] involves three main steps, as depicted in Figure 1.1. Starting from EDOT $HX_{n-1}H$ and HXH molecules, first (step 1) charging is achieved by an electron transfer toward an oxidant agent present in the chemical environment. The resulting two EDOT radical cations $HX_{n-1}H^+$ and HXH^+ are formed and then (step 2) bind together in a radical dication, an unstable intermediate reaction. The first two steps should be characterised by a positive reaction energy since in the first stage EDOT's thiophene ring is forced to loss aromaticity and in the second one two cations must approach in order to make binding possible.

Finally, (step 3) by the release of the two protons in the unstable reaction intermediate, the neutral product HX_nH is finally formed. Decharging process is assisted by the two molecules B,B' absorbing the hydron cations produced and thus commonly referred to as "proton scavengers". Since each thiophene ring can now regain aromaticity, energitically stabilizing the product, this step is probably the one which allows to the overall reaction to occur.

A charged monomer can eventually react with an olygomer composed by $n-1$ EDOT units ($n \geq 3$), provided it has been oxidised in order to achieve a +e charge. Following with the same mechanism described above, at the end a neutral olygomer made up of n EDOT units is formed.

Since charging of monomers and olygomers is crucial in order to trigger the reaction, many oxidant agents have been tested during the time, such as H_2O_2[25] and iron(III) salts, especially iron(III)chlorine[11] and iron(III)tosylate. Iron(III) sulfonates, as tosylate, allows the formation of films instead of highly conductive powders such as iron(III)chlorine in boiling benzonitrile.[8] Tosylate is currently one of the most used oxidant because it can be easily dissolved in aliphatic alcohols, mainly buthanol and ethanol, without reacting and forming precipitates and forming long pot-life solution.[8]

While iron(III)chlorine could crystallise during the EDOT polymerisa-

tion, affecting the overall film formation,[9] tosylate does not show any tendency to create crystalline structures.

Even if VPP technique makes possible to realise PEDOT films using $FeCl_3$ as oxidant, reported conductivity ($70\ \Omega^{-1}cm^{-1}$) is usually poor if compared to tosylate-based films, unless a base inhibitor as pyridine is used.[19]

The role of pyridine as a polymerization inhibitor is shown experimentally by Winther-Jensen et al.[36] The authors report[36] that monomers can participate in *acidity-driven* reactions resulting in partially conjugated chains.

The introduction of pyridine is therefore motivated with the specific aim of preventing the occurrence of these reactions. It is also stated[36] that pyridine is chosen in place of other bases, such as imidazole, both because of its volatility, sufficiently high to guarantee its subsequent removal, both because it does not show a tendency to crystallize with tosylate, a process that would interfere with the polymerization process.

The results obtained are that the increase in pH caused by pyridine largely affects the rate of polymerization.[36]

This is in agreement with that obtained by de Leeuw et al.[6] by means of an electroplating technique suggesting that as long as the base used, imidazole, is not removed, the polymerization does not take place.

The role of pH was investigated by Reuter et al.[16] They report that the EDOT polymerization process is characterized by a slow phase and a rapid phase: the slowest phase, as reported, is the one in which the monomers are oxidized while the rapid phase is represented by the dimerization.[16] The oxidation of the oligomers, on the other hand, is significantly faster than that of the monomers and is assumed independent of the length of the oxidized chain.

The acidification of the reaction environment catalyzes the polymerization. In particular, the acids lead to an equilibrium reaction in which the products are dimers or trimers, without further oxidation.[16]

1.1.1 The role of water

Since pyridine is assumed as reaction inhibitor, both tosylate anion and water could possibly act as proton scavengers.

The role played by water in the polymerization reaction was extensively studied by Fabretto et al. using the Vapor Phase Polymerization technique. In their work,[9] water is clearly identified as the proton scavenger but, in dry phase, pyridine alone is reported to produce films with reduced length of the PEDOT chains.

In Winther work,[35] instead, tosylate is recognized as the proton scavenger for PEDOT polymerization.

1.2 Open questions

Even if the generally adopted microscopic model is able to capture the main features of PEDOT polymerization, there are still many open questions that need to be addressed:

- **the identification of the proton scavenger**. Referring to the described polymerisation process, we found several works in literature reporting experimental studies which try to elucidate the identity of the proton scavenger, supposed to be water[9] or tosylate anion.[35] However the exact nature of the proton scavenger is still not clearly identified in Literature;

- **the influence of proton scavenger on average chain length and on chain length distribution.** Average chain length could be in fact crucial in determining many physical properties of interest of the polymer, such as electrical conductivity. However the reported values for PEDOT are reported to vary from 7 up to 20 monomeric units,[10,24] with no clear evidence showing if and especially how the chain length could be tuned by acting on the reactant choice or concentration.;

- **the impact of chain length distribution on morphology.** This corresponds to explain the influence of the scavenger on the final morphology, a correlation clearly observed if pyridine is used[19,35] and explained as due by the suppression of acidic unwanted side reactions;

- **the impact of morphology and chain length distribution on thermal and electronic transport properties**, as suggested in Salleo's work,[12] in which the role of chains connecting two crystallite separated by an amorphous phase is emphasized. According to the authors, in fact, this could allow to achieve high electrical conductivity with no significant increase of thermal transport.

Questions we address are probably very difficult (if not impossible) to be answered only by experiments due to the impossibility of disentangling the contribution of each chemical species in solution since the remotion of even a single reactant should stop the polymerization process.

A novel computational approach to simulate the polymerization process was thus developed, as explained in Chapter 3, to address the question on the identity of the proton scavenger and its influence on micromorphology.

Heat and carrier transport properties on each specific sample generated with a unique combination of scavengers were also analyzed in Chapter 4 and 5, respectively.

1.3 Outline of the Thesis

The work of this Thesis is organized as follows.

In Chapter 2 a brief review of the theoretical methods is provided, the Density Functional Theory (DFT), the classical Molecular Dynamics (MD) and the Marcus theory applied to estimate the hopping rates.

In Chapter 3 a novel computational tool, based on a combination of pure Density Functional Theory calculations and classical Molecular Dynamics is described. The present methodology is then used to characterize the influence of reactants used in polymerization on PEDOT chain length distribution.

In Chapter 4 the PEDOT samples generated "in silico" are characterized in terms of their thermal transport properties. It is here shown that the chain length distribution and the degree of crystallinity are related to an intrinsic anisotropy of the thermal conductivity κ and to modifications in the vibrational frequencies involved.

In Chapter 5 the problem of estimating the electrical conductivity σ for each sample is addressed in the context of the hopping model in which the hopping rates are calculated with DFT techniques. Carrier transport appears to be greatly influenced by the choice of reactants, in some cases in a very non-trivial way.

In Chapter 6, finally, a resume of the results obtained and the future perspectives for this work are presented.

Bibliography

[1] Eun Jin Bae, Young Hun Kang, Kwang-Suk Jang, Changjin Lee, and Song Yun Cho. Solution synthesis of telluride-based nano-barbell structures coated with pedot: Pss for spray-printed thermoelectric generators. *Nanoscale*, 8(21):10885–10890, 2016.

[2] Amare Benor, Shin-ya Takizawa, César Pérez-Bolívar, and Pavel Anzenbacher Jr. Efficiency improvement of fluorescent oleds by tuning the working function of pedot: Pss using uv–ozone exposure. *Organic Electronics*, 11(5):938–945, 2010.

[3] Aimee M. Bryan, Luciano M. Santino, Yang Lu, Shinjita Acharya, and Julio M. D'Arcy. Conducting polymers for pseudocapacitive energy storage. *Chemistry of Materials*, 28(17):5989–5998, 2016.

[4] C. K. Chiang, C. R. Fincher, Y. W. Park, A. J. Heeger, H. Shirakawa, E. J. Louis, S. C. Gau, and Alan G. MacDiarmid. Electrical conductivity in doped polyacetylene. *Phys. Rev. Lett.*, 39:1098–1101, Oct 1977.

[5] MM De Kok, M Buechel, SIE Vulto, P Van de Weijer, EA Meulenkamp, SHPM De Winter, AJG Mank, HJM Vorstenbosch, CHL Weijtens, and V Van Elsbergen. Modification of pedot: Pss as hole injection layer in polymer leds. *physica status solidi (a)*, 201(6):1342–1359, 2004.

[6] D.M. de Leeuw, P.A. Kraakman, P.F.G. Bongaerts, C.M.J. Mutsaers, and D.B.M. Klaassen. Electroplating of conductive polymers for the metallization of insulators. *Synthetic Metals*, 66(3):263 – 273, 1994.

[7] K Deshmukh, M Basheer Ahamed, RR Deshmukh, SK Khadheer Pasha, PR Bhagat, and K Chidambaram. Biopolymer composites with high di-

electric performance: interface engineering. In *Biopolymer composites in electronics*, pages 27–128. Elsevier, 2017.

[8] A. Elschner, S. Kirchmeyer, W. Lovenich, U. Merker, and K. Reuter. *PEDOT: Principles and Applications of an Intrinsically Conductive Polymer*. CRC Press, 2010.

[9] Manrico Fabretto, Kamil Zuber, Colin Hall, and Peter Murphy. High conductivity pedot using humidity facilitated vacuum vapour phase polymerisation. *Macromolecular Rapid Communications*, 29(16):1403–1409, 2008.

[10] Juan Felipe Franco-Gonzalez and Igor V. Zozoulenko. Molecular dynamics study of morphology of doped pedot: From solution to dry phase. *The Journal of Physical Chemistry B*, 121(16):4299–4307, 2017. PMID: 28380297.

[11] Heywang Gerhard and Jonas Friedrich. Poly(alkylenedioxythiophene)s—new, very stable conducting polymers. *Advanced Materials*, 4(2):116–118.

[12] Scott Himmelberger, Koen Vandewal, Zhuping Fei, Martin Heeney, and Alberto Salleo. Role of molecular weight distribution on charge transport in semiconducting polymers. *Macromolecules*, 47(20):7151–7157, 2014.

[13] Zia Ullah Khan, Olga Bubnova, Mohammad Javad Jafari, Robert Brooke, Xianjie Liu, Roger Gabrielsson, Thomas Ederth, Drew R Evans, Jens W Andreasen, Mats Fahlman, et al. Acido-basic control of the thermoelectric properties of poly (3, 4-ethylenedioxythiophene) tosylate (pedot-tos) thin films. *Journal of Materials Chemistry C*, 3(40):10616–10623, 2015.

[14] Jae-Yeop Kim, Woohwa Lee, Young Hun Kang, Song Yun Cho, and Kwang-Suk Jang. Wet-spinning and post-treatment of cnt/pedot: Pss composites for use in organic fiber-based thermoelectric generators. *Carbon*, 133:293–299, 2018.

[15] Jinyeol Kim, Daewon Sohn, Yuneyoung Sung, and Eung-Ryul Kim. Fabrication and characterization of conductive polypyrrole thin film prepared by in situ vapor-phase polymerization. *Synthetic Metals*, 132(3):309 – 313, 2003.

[16] Stephan Kirchmeyer and Knud Reuter. Scientific importance, properties and growing applications of poly (3, 4-ethylenedioxythiophene). *Journal of Materials Chemistry*, 15(21):2077–2088, 2005.

[17] Renee Kroon, Desalegn Alemu Mengistie, David Kiefer, Jonna Hynynen, Jason D. Ryan, Liyang Yu, and Christian Müller. Thermoelectric plastics: from design to synthesis, processing and structure–property relationships. *Chem. Soc. Rev.*, 45:6147–6164, 2016.

[18] Thanh-Hai Le, Yukyung Kim, and Hyeonseok Yoon. Electrical and electrochemical properties of conducting polymers. *Polymers*, 9(4):150, 2017.

[19] Thuy Le Truong, Nguyen Dang Luong, Jae-Do Nam, Youngkwan Lee, Hyouk Ryeol Choi, Ja Choon Koo, and Huu Nieu Nguyen. Poly (3, 4-ethylenedioxythiophene) vapor-phase polymerization on glass substrate for enhanced surface smoothness and electrical conductivity. *Macromolecular research*, 15(5):465–468, 2007.

[20] Jung Joon Lee, Dohyuk Yoo, Chanil Park, Hyang Hee Choi, and Jung Hyun Kim. All organic-based solar cell and thermoelectric generator hybrid device system using highly conductive pedot: Pss film as organic thermoelectric generator. *Solar Energy*, 134:479–483, 2016.

[21] Sunghwan Lee and Karen K Gleason. Enhanced optical property with tunable band gap of cross-linked pedot copolymers via oxidative chemical vapor deposition. *Advanced Functional Materials*, 25(1):85–93, 2015.

[22] David Lewis and Samuel Glasstone. *Elements of physical chemistry*. Macmillan, 1960.

[23] Wilfried Lövenich. Pedot-properties and applications. *Polymer Science Series C*, 56(1):135–143, 2014.

[24] David C Martin, Jinghang Wu, Charles M Shaw, Zachary King, Sarah A Spanninga, Sarah Richardson-Burns, Jeffrey Hendricks, and Junyan Yang. The morphology of poly (3, 4-ethylenedioxythiophene). *Polymer Reviews*, 50(3):340–384, 2010.

[25] A. Mohammadi, I. Lundström, W.R. Salaneck, and O. Inganäs. Polypyrrole prepared by chemical vapour deposition using hydrogen peroxide and hydrochloric acid. *Synthetic Metals*, 21(1):169 – 173, 1987. Proceedings of the Conference on Electronic Processes in Conducting Polymers.

[26] W. A. Muñoz, Sandeep Kumar Singh, J. F. Franco-Gonzalez, M. Linares, X. Crispin, and I. V. Zozoulenko. Insulator to semimetallic transition in conducting polymers. *Phys. Rev. B*, 94:205202, Nov 2016.

[27] Burhan Muhsin, Roland Roesch, Gerhard Gobsch, and Harald Hoppe. Flexible ito-free polymer solar cells based on highly conductive pedot:pss and a printed silver grid. *Solar Energy Materials and Solar Cells*, 130:551 – 554, 2014.

[28] Dan Ni, Haijun Song, Yuanxun Chen, and Kefeng Cai. Free-standing highly conducting pedot films for flexible thermoelectric generator. *Energy*, 170:53–61, 2019.

[29] Ioannis Petsagkourakis, Eleni Pavlopoulou, Eric Cloutet, Yan Fang Chen, Xjianjie Liu, Mats Fahlman, Magnus Berggren, Xavier Crispin, Stefan Dilhaire, Guillaume Fleury, et al. Correlating the seebeck coefficient of thermoelectric polymer thin films to their charge transport mechanism. *Organic Electronics*, 52:335–341, 2018.

[30] Boris Russ, Anne Glaudell, Jeffrey J Urban, Michael L Chabinyc, and Rachel A Segalman. Organic thermoelectric materials for energy harvesting and temperature control. *Nature Reviews Materials*, 1(10):1–14, 2016.

[31] Phil M. Smith, Laisuo Su, Wei Gong, Nathan Nakamura, B. Reeja-Jayan, and Sheng Shen. Thermal conductivity of poly(3,4-ethylenedioxythiophene) films engineered by oxidative chemical vapor deposition (ocvd). *RSC Adv.*, 8:19348–19352, 2018.

[32] M. V. Vedernikov and E. K. Iordanishvili. A.f. ioffe and origin of modern semiconductor thermoelectric energy conversion. In *Seventeenth International Conference on Thermoelectrics. Proceedings ICT98 (Cat. No.98TH8365)*, pages 37–42, May 1998.

[33] Yi-Fei Wang, Tomohito Sekine, Yasunori Takeda, Koji Yokosawa, Hiroyuki Matsui, Daisuke Kumaki, Takeo Shiba, Takao Nishikawa, and Shizuo Tokito. Fully printed pedot: Pss-based temperature sensor with high humidity stability for wireless healthcare monitoring. *Scientific reports*, 10(1):1–8, 2020.

[34] Qingshuo Wei, Masakazu Mukaida, Kazuhiro Kirihara, Yasuhisa Naitoh, and Takao Ishida. Recent progress on pedot-based thermoelectric materials. *Materials*, 8(2):732–750, 2015.

[35] Bjørn Winther-Jensen and Keld West. Vapor-phase polymerization of 3, 4-ethylenedioxythiophene: a route to highly conducting polymer surface layers. *Macromolecules*, 37(12):4538–4543, 2004.

[36] Bjørn Winther-Jensen, Dag W. Breiby, and Keld West. Base inhibited oxidative polymerization of 3,4-ethylenedioxythiophene with iron(iii)tosylate. *Synthetic Metals*, 152(1):1 – 4, 2005. Proceedings of the International Conference on Science and Technology of Synthetic Metals.

[37] Yijie Xia, Hongmei Zhang, and Jianyong Ouyang. Highly conductive pedot: Pss films prepared through a treatment with zwitterions and their application in polymer photovoltaic cells. *Journal of Materials Chemistry*, 20(43):9740–9747, 2010.

[38] Jae Choul Yu, Ji A Hong, Eui Dae Jung, Da Bin Kim, Soo-Min Baek, Sukbin Lee, Shinuk Cho, Sung Soo Park, Kyoung Jin Choi, and Myoung Hoon Song. Highly efficient and stable inverted perovskite solar cell employing pedot: Go composite layer as a hole transport layer. *Scientific reports*, 8(1):1–9, 2018.

[39] Xinyu Zhang, Jeong-Soo Lee, Gil S Lee, Dong-Kyu Cha, Moon J Kim, Duck J Yang, and Sanjeev K Manohar. Chemical synthesis of pedot nanotubes. *Macromolecules*, 39(2):470–472, 2006.

Chapter 2

Methods

2.1 Density Functional Theory (DFT)

2.1.1 Theoretical foundations

Quantum mechanical calculations for thermochemical and for charge transport properties involving a molecule or an ion can be stated in the form of resolution of the general time independent Schrödinger equation[6]

$$\hat{\mathcal{H}}_{\text{tot}}\Psi = E\Psi \tag{2.1}$$

where Ψ and H are the global wavefunction and the Hamiltonian of the system formed by all the nuclei and all the electrons constituting the molecule (ion) at a global energy E.

The Hamiltonian $\hat{\mathcal{H}}_{\text{tot}}$ can be written as a function of nuclear $\boldsymbol{R_\alpha}$ and electronic $\boldsymbol{r_n}$ coordinates as the sum of kinetic, potential and interaction contributions, namely[35]

$$\begin{aligned}\hat{\mathcal{H}}_{\text{tot}} = -\frac{\hbar^2}{2}\sum_{\alpha}\frac{\nabla^2_{\boldsymbol{R_\alpha}}}{M_\alpha} - \frac{\hbar^2}{2m_e}\sum_{n}\nabla^2_{\boldsymbol{r_n}} + \frac{e^2}{2}\sum_{\alpha}\sum_{\beta\neq\alpha}\frac{Z_\alpha Z_\beta}{|\boldsymbol{R_\alpha}-\boldsymbol{R_\beta}|} \\ +\frac{e^2}{2}\sum_{m}\sum_{n\neq m}\frac{1}{|\boldsymbol{r_m}-\boldsymbol{r_n}|} - e^2\sum_{\alpha}\sum_{n}\frac{Z_\alpha}{|\boldsymbol{R_\alpha}-\boldsymbol{r_n}|}\end{aligned} \tag{2.2}$$

where summations on Latin m, n indexes run over the total number of electrons and summations on Greek indexes over the total number of nuclei, each one with mass M_α and nuclear charge Z_α.

In most of the applications, it can safely assumed that the contribution arising from the motion of nuclei is negligible compared with its electronic

counterpart. Starting from this assumption, called the Born-Oppenheimer approximations, the total Hamiltonian takes the form[35]

$$\hat{\mathcal{H}}_{\text{tot}} = -\frac{\hbar^2}{2m_e}\sum_n \nabla^2_{\boldsymbol{r_n}} + \frac{e^2}{2}\sum_m \sum_{n\neq m} \frac{1}{|\boldsymbol{r_m} - \boldsymbol{r_n}|} - e^2 \sum_\alpha \sum_n \frac{Z_\alpha}{|\boldsymbol{R_\alpha} - \boldsymbol{r_n}|} \quad (2.3)$$

which differs from Eq. 2.2 because no kinetic and no potential contribution arising from nuclear motion is now present (frozen-nuclei approximation).

Several techniques have been developed in order to solve Eq. 2.3, as the Hartree-Fock (HF) method, Multi-Configuration Self Consistent Field (MCSCF),[10,35] Configuration Interactions (CI),[37] but all of them shares a common issue, the fact that the calculation of the global wavefunction for the Hamiltonian 2.3 is very difficult in terms of computational power required even for very small (~ 10 atoms) molecules.

This difficult was overcome by the Density Functional theory developed by Hohenberg and Kohn[16] by radically rethinking the entire approach to the calculation of quantum properties on the basis of a fundamental key idea and two powerful theorems, the HK theorems.

The first seminal idea, which can be retraced in the work of Fermi and Thomas,[12,19,42] consists in replacing the wavefunction Ψ with the corresponding electron charge density $n(\boldsymbol{r})$ to describe and extract all the properties of interest.

In the most common cases, in fact, the wavefunction provides an amount of information redundant[35] and excessively high compared to the properties under examination, as for the calculation of electric dipole moment of a molecule.

Instead of focusing on a multidimensional function of all the electronic spatial coordinates of the systems, Fermi and Thomas proposed to start from the simpler description of an atom in terms of a three dimensional function, the charge density $n(\boldsymbol{r})$.

Even if the Fermi-Thomas model was very rough and not sufficiently accurate to predict even very simple properties, as the molecular bonds,[41] their key idea was further refined in 1964 when Hohenberg and Kohn finally provided the theoretical basis to the actual successful and large scale implementation.

The first HK theorem[16,21] states that, given a system of N interacting particles under the action of an external potential $V_{\text{ext}}(\boldsymbol{r})$, the potential applied is a unique functional of the charge density $n(\boldsymbol{r})$ within an additive constant.

The energy of a quantum systems with a given electronic density $n(\boldsymbol{r})$, usually written in terms of the Hamiltonian and the wavefunction as

$$E[n(\boldsymbol{r})] = \langle \Psi | \hat{\mathcal{H}} | \Psi \rangle \tag{2.4}$$

can thus be restated in the form

$$E[n(\boldsymbol{r})] = \int n(\boldsymbol{r}) V_{\text{ext}}(\boldsymbol{r}) d\boldsymbol{r} + F[n(\boldsymbol{r})] \tag{2.5}$$

where $F[n(\boldsymbol{r})]$ is the more general form for the arbitrary constant energy shift.

Referring to Eq. 2.3, the external potential $V_{\text{ext}}(\boldsymbol{r})$ can be easily identified with the last term of the sum

$$V_{\text{ext}}(\boldsymbol{r}) = -e^2 \sum_{\alpha} \sum_{n} \frac{Z_\alpha}{|\boldsymbol{R_\alpha} - \boldsymbol{r_n}|} \tag{2.6}$$

while the sum of electronic kinetic energy and inter-electronic repulsion constitutes the $F[n(\boldsymbol{r})]$ so called *universal functional*, since it depends only by kinetic and repulsion energy of electrons.

The existence of the universal functional, sum of the kinetic $T[n(\boldsymbol{r})]$ and interaction $E_{\text{int}}[n(\boldsymbol{r})]$ functionals, is assured by the second HK theorem,[21] which also states that the global minimum $n_0(\boldsymbol{r})$ for the functional in Eq. 2.5 corresponds exactly to the ground state (GS) of the system.

Another important conceptual step in building a computationally accessible technique for quantum mechanical problems was posed by Kohn and Sham and usually referred to as the Kohn-Sham ansatz (KS ansatz),[18] which consists in rewriting the problem of N interacting particles in an external potential V_{ext} in terms of a non-interacting gas of N particles in the same effective potential which reproduce the total effect of nuclear and inter-electron interactions.

It can be proved that, for closed shell N-electrons structures, replacing the electronic density $n(\boldsymbol{r})$ with the sum of the square modulus of atomic orbitals (AO)

$$n(\boldsymbol{r}) = 2 \sum_{i}^{N/2} |\phi_i|^2 \tag{2.7}$$

allows to write

$$E_{\text{KS}}[n] = 2 \sum_{i}^{N/2} \int d\boldsymbol{r}' \phi^*(\boldsymbol{r}') \left(-\frac{\hbar^2}{2m_e} \nabla^2 \right) \phi(\boldsymbol{r}') + E_{\text{H}}[n] + E_{\text{ext}}[n] + E_{\text{xc}}[n] \tag{2.8}$$

The variational principle is applied on Eq. 2.8, using the Lagrange multipliers technique to impose on minimization the constrains due by the orthonormality of ϕ_i. For the resulting Ω_{KS} Lagrangian containing the λ_{ij} Lagrange multipliers

$$\Omega_{\mathrm{KS}} = E_{\mathrm{KS}}[n] - 2\sum_{i,j}^{N/2} \lambda_{ij} \left(\int d\boldsymbol{r}' \phi_i^*(\boldsymbol{r}')\phi_j(\boldsymbol{r}') - \delta_{ij} \right) \tag{2.9}$$

the stationary condition

$$\frac{\delta \Omega_{\mathrm{KS}}[n]}{\delta \phi_j^*(\boldsymbol{r}')} = 0 \tag{2.10}$$

which can be expanded as

$$\frac{\delta \Omega_{\mathrm{KS}}[n]}{\delta n(\boldsymbol{r}')} \frac{\delta n(\boldsymbol{r}')}{\delta \phi_j^*(\boldsymbol{r}')} = 2\frac{\delta \Omega_{\mathrm{KS}}[n]}{\delta n(\boldsymbol{r}')} \phi_j(\boldsymbol{r}') = 0 \tag{2.11}$$

is satisfied when

$$\left(-\frac{\hbar^2}{2m_e}\nabla_i^2 + V_{\mathrm{KS}}(\boldsymbol{r}) - \epsilon_i \right) \psi_i(\boldsymbol{r}) = 0 \tag{2.12}$$

where ψ_i is the wavefunction for the ith electron in the potential V_{KS} (Kohn-Sham potential), containing the functional derivatives of Hartree-Fock[1,13,15] (H), external (ext) and exchange-correlation (xc) functionals

$$V_{\mathrm{KS}} = \frac{\delta E_{\mathrm{H}}}{\delta n} + \frac{\delta E_{\mathrm{ext}}}{\delta n} + \frac{\delta E_{\mathrm{xc}}}{\delta n} \tag{2.13}$$

Each of the ψ_i can be regarded as the ith orbital with ϵ_i energy occupied by the corresponding electron and are thus usually known as Kohn-Sham orbitals.

Since the total electron density can be written as the square modulus of the normalized orbitals

$$n(\boldsymbol{r}) = \sum_i |\psi_i(\boldsymbol{r})|^2 \tag{2.14}$$

the universal functional in Eq. 2.5 assumes the form

$$F[n(\boldsymbol{r})] = T[n(\boldsymbol{r})] + E_{\mathrm{H}}[n(\boldsymbol{r})] + E_{\mathrm{XC}}[n(\boldsymbol{r})] \tag{2.15}$$

where the first terms is the functional for kinetic energy

$$T[n(\boldsymbol{r})] = -\frac{\hbar^2}{2m_e} \sum_i \langle \psi_i | \nabla^2 | \psi_i \rangle \tag{2.16}$$

The kinetic term can further restated in terms of the Kohn-Sham energies of orbitals ϵ_i as

$$T[n(\boldsymbol{r})] = \sum_i \epsilon_i - \int d\boldsymbol{r}' n(\boldsymbol{r}') V_{\text{ext}}[n(\boldsymbol{r}')] \tag{2.17}$$

the second term the usual Hartree-Fock electrostatic energy

$$E_{\text{H}}[n(\boldsymbol{r})] = \frac{1}{2} \iint d\boldsymbol{r} d\boldsymbol{r}' \frac{n(\boldsymbol{r}) n(\boldsymbol{r}')}{|\boldsymbol{r} - \boldsymbol{r}'|} \tag{2.18}$$

and the last term is the so called exchange-correlation energy since includes all non-electrostatic contributions, as the exchange interaction.

It can be finally proved that the Kohn-Sham interaction potential V_{KS} for the system of non-interacting electrons includes both the external and the electrostatic (Hartree-Fock) potential

$$V_{\text{KS}} = V_{\text{ext}} + V_{\text{H}} + \frac{\delta E_{\text{XC}}[n(\boldsymbol{r})]}{\delta n(\boldsymbol{r})} \tag{2.19}$$

where

$$V_{\text{H}} = \int d\boldsymbol{r}' \frac{n(\boldsymbol{r})}{|\boldsymbol{r} - \boldsymbol{r}'|} \tag{2.20}$$

The proper form for the exchange-correlation functional $E_{\text{XC}}[n(\boldsymbol{r})]$ is crucial in order to obtain accurate results.

Several approximations have been developed since the introduction of Kohn-Sham equations. One of the first proposed was the Local Density Approximation[33] (LDA) based on the approximation of a system called homogeneous electron liquid. an infinite extending ensemble of interacting electrons with constant fixed density n_0. For this system, accurate computational calculations of exchange-correlation contribution $e^{\text{h}}_{\text{XC}}(\bar{n})$, based on extrapolation and fitting, are available as function of the density $\bar{n}$, and are used in LDA for a non-homogeneous system in the form

$$E^{\text{LDA}}_{\text{XC}}[n] = \int d\boldsymbol{r}' e^{\text{h}}_{\text{XC}}(n(\boldsymbol{r}')) \tag{2.21}$$

where the electron density is calculated for each $\boldsymbol{r}'$ point in the integration domain.

Starting from LDA and taking into account the spin polarization state, two separate electron densities $n^{\uparrow}(\boldsymbol{r}')$, $n^{\downarrow}(\boldsymbol{r}')$ are defined and used to define the Local Spin Density Approximation[33] (LSDA)

$$E^{\text{LSDA}}_{\text{XC}}[n^{\uparrow}, n^{\downarrow}] = \int d\boldsymbol{r}' e^{\text{h}}_{\text{XC}}(n^{\uparrow}(\boldsymbol{r}'), n^{\downarrow}(\boldsymbol{r}')) \tag{2.22}$$

A more refined approximation for the real (and still unknown) form of the exchange-correlation functional is represented by the family of the Generalized Gradient Approximations (GGA's),[26] collecting all the functionals that parameterize the exchange-correlation contribution in terms not only of the local density $n(\boldsymbol{r}')$ but also of its gradient $\vec{\nabla} n(\boldsymbol{r}')$

$$E_{\mathrm{XC}}^{\mathrm{GGA}}[n] = \int d\boldsymbol{r}' e_{\mathrm{XC}}(n(\boldsymbol{r}'), \vec{\nabla} n(\boldsymbol{r}'))n(\boldsymbol{r}') \tag{2.23}$$

In many cases, the spin polarization is also taken into account and . The GGA's are thus written as

$$E_{\mathrm{XC}}^{\mathrm{GGA}}[n^{\uparrow}, n^{\downarrow}] = \int d\boldsymbol{r}' e_{\mathrm{XC}}(n^{\uparrow}, n^{\downarrow}, \vec{\nabla} n^{\uparrow}, \vec{\nabla} n^{\downarrow})n(\boldsymbol{r}') \tag{2.24}$$

where in the formulation of e_{XC} are frequently used parameters fitted on experimental data.

Two examples of GGA functionals are the Becke's exchange functional, B88,[4] explicitly containing the reduced gradient spin density ω_s

$$\omega_s = \frac{|\vec{\nabla} n_s(\boldsymbol{r})|}{n_s(\boldsymbol{r})^{\frac{4}{3}}} \tag{2.25}$$

with s being the index for spin up and spin down, in the general form

$$E_{\mathrm{X}}^{\mathrm{B88}}[n^{\uparrow}, n^{\downarrow}] = E_{\mathrm{X}}^{\mathrm{LSDA}}[n^{\uparrow}, n^{\downarrow}] - \beta \sum_s \int d\boldsymbol{r}' n_s^{\frac{4}{3}} \frac{\omega_s^2}{1 + 6\beta\omega_s \mathrm{sinh}^{-1}(\omega_s)} \tag{2.26}$$

with β obtained by fit of Hartree-Fock exchange energies, and the LYP correlation functional of Lee, Yang and Parr[20, 30]

$$E_{\mathrm{c}}^{\mathrm{LYP}} = -a \int \frac{d\boldsymbol{r}'}{1 + dn} \left[n + bn^{-\frac{1}{3}} \left(C_F n^{\frac{5}{3}} - 2t_W + \frac{1}{9} \left(t_W + \frac{\nabla^2 n}{2} \right) \exp\left(-cn^{-\frac{1}{3}} \right) \right) \right] \tag{2.27}$$

with a, b, c, d fiiting parameters, C_F a numerical constant and t_W the combination of the gradient and the Laplacian of electron density

$$t_W = \frac{1}{8} \left(\frac{|\vec{\nabla} n|}{n} - \nabla^2 n \right) \tag{2.28}$$

By properly summing the exchange and the correlation contribution from GGA and LDA functional, obtaining the so-called hybrid functionals, very

accurate results can be obtained. One of the most popular hybrid functional, which combines the LDA and B88 exchange contributions with LYP exchange-functional, is the B3LYP,[39] where B indicates the presence of Becke's functional, LYP denotes the LYP exchange and 3 is the number of parameters involved

$$\begin{aligned} E_{\mathrm{XC}}^{\mathrm{B3LYP}} &= aE_{\mathrm{X}}^{\mathrm{H}} + bE_{\mathrm{X}}^{\mathrm{B88}} + (1-a)E_{\mathrm{X}}^{\mathrm{LDA}} \\ &+ cE_{\mathrm{C}}^{\mathrm{LYP}} + (1-c)E_{\mathrm{X}}^{\mathrm{LDA}} \end{aligned} \tag{2.29}$$

with $a = 0.20$, $b = 0.72$, $c = 0.81$ and $E_{\mathrm{X}}^{\mathrm{H}}$ the Hartree-Fock exchange functional.

2.1.2 Basis set

In order to perform a DFT calculation, a set of functions to express the Kohn-Sham orbitals entering in Eq. 2.12 is required.

Besides the functions used to describe the orbitals, additional requirements are needed, mainly dictated by considerations about computational efficiency. It is well known since the development of Hartree-Fock theory[1,13,15] that, as consequence of adopting the variational principle to solve Schrödinger equation, the accuracy in energy and quantum properties increases with the number of function in the basis set used to expand the orbitals. However, this comes with a cost that increases roughly as N^4 for Hartree-Fock method and N^3 for DFT,[35] where N is the number of function in the basis set, mainly due by the calculation of the two-electron integrals in the Self-Consistent Field (SCF) procedure.

Additionally, the functions employed in expansion should have a clear physical and chemical meaning, in the sense that they would describe as accurate as possible the correct probability of finding an electron in each point of the quantum system.

In order to address to all these requirements, several approaches have been developed. The most common choice for calculation of quantum properties of single molecules is represented by the Gaussian-Type Orbitals (GTO), introduced as computational more affordable alternative for Slater-Type Orbitals (STO).

The most simple form of GTO is called primitive Gaussian ψ and can be expressed as

$$\psi = \underbrace{\left(\frac{2\alpha}{\pi}\right)^{\frac{3}{4}} \left[\frac{(8\alpha)^{i+j+k} i!j!k!}{(2i)!(2j)!(2k)!}\right]^{\frac{1}{2}}}_{\text{normalization constant}} x^i y^j z^k \exp\left(-\alpha(x^2+y^2+z^2)\right) \tag{2.30}$$

where α is related with the orbital spatial extension and i, j, k integer coefficients related with the final symmetry of the orbital and the orbital angular momentum L via

$$L = i + j + k \tag{2.31}$$

Following the common notation for hydrogen-like orbitals, if all the indexes are zero ($L = 0$) ψ is spherical and referred to as s-type orbital. If only one index is 1 ($L = 1$) the orbitals is p-type (with all the three possibilities, p_x, p_y, p_z possible), and finally if the sum of two indexes is 2 ($L = 2$) the orbital is d-type.

To reproduce the correct asymptotic decay as ($\exp(-r)$), it is common practice to sum n primitive Gaussians in a linear combination. This defines a new basis function ϕ_{CGTO}, which is called Contracted Gaussian-Type Orbitals (CGTO's) with n degree of contraction, namely

$$\phi_{\mathrm{CGTO}} = \sum_{i=1}^{n} w_i \psi_i \tag{2.32}$$

where w_i are the coefficients entering in the linear combination.

The number of basis function ϕ_{CGTO} used to describe each Atomic Orbital (AO) defines an important subdivision among the family of GTO. If exactly one basis function is used to describe an AO, the set is referred to as single-ζ, while in multiple-ζ basis sets an increasing number of basis function is used to describe each AO.

For physical-chemistry applications, however, a sufficient increase in accuracy while maintaining a reasonable computational cost is achieved by increasing the basis function ϕ_{CGTO} per AO only on the subset of functions describing the valence electrons, while the one-to-one correspondence is conserved for all core electrons.

This subfamily of basis sets are called split-valence basis sets and includes one of the most common used, are Pople's basis set.[11,28]

Pople's basis set is characterized by a sequence of number and the final G letter, each number denoting the number of primitive Gaussian function used for the description of AO. As case of interest, one of the most used basis set (as described in Chapter 3 and 5 of the present thesis) is 6-311G, where 6 denotes the number of primitive Gaussians (Eq. 2.30) contracted in the single ϕ_{CGTO} function for the core AO. The three subsequent numbers, 3 1 1, denotes that a triple-ζ valence scheme is adopted, i.e. that each valence AO is described by three ϕ_{CGTO}, one of each is the contraction of 3 primitive Gaussians, while the remaining two are made up by 1 primitive Gaussian.

To increase flexibility and accuracy in determining effects related to polarization, an extra basis function is added to each AO. Generally, to polarize a basis function with angular momentum L, a basis functions with angular momentum $L+1$ is combined with the pre-existing basis set. Polarization of s orbital of hydrogen is thus achieved by mixing with a p-type GTO while for p orbitals of carbon a d-type function is used. In this case, the Pople's basis set reads as 6-311G(p,d), with d and p indicating the type of polarization function added to hydrogen and *heavy* (non-hydrogen) atoms, respectively.

2.1.3 Self Consistent Field procedure in DFT

To find the numerical solutions of Eq. 2.12, a proper and iterative methodology must be set up to calculate the $\psi_i(\boldsymbol{r})$ Kohn-Sham orbitals.

The most common strategy adopted is the Self Consistent Field (SCF) procedure, conceptually based on the fact that the energy is a functional of KS orbitals. The following iterative approach is thus applied

1. an initial trial set of Kohn-Sham orbitals, $\psi_i^{(n=0)}$ is generated;
2. Kohn-Sham operator $\hat{h}_{\mathrm{KS}}^{(n)}$ is constructed using the selected orbital set;
3. solution fo Kohn-Sham equation is obtained by diagonalization of the resulting matrix, obtaining a new $\psi_i^{(n+1)}$ set of orbitals;
4. a target properties is calculated (i.e. the total energy). If the deviations of the calculated value at iteration $n+1$ from the value calculated at iteration n is below a fixed cut-off, the procedure is considered converged. Otherwise, the $\psi_i^{(n+1)}$ set is used as new $\psi_i^{(n)}$ and steps 2, 3 and 4 are repeated until convergence.

2.1.4 Theoretical background of the solvation problem

In the study of the problem of PEDOT polymerization using ab initio techniques, particular care should be posed to the fact that the all chemical processes of interest take place in a solution environment.

For this reason, the determination of accurate and realistic reaction free energies must include the contribution of microscopical interactions of both the reactants and products molecules with the surrounding solvent molecules, a problem which in its more general form can be stated as the search for the ground state of the total Hamiltonian operator

$$H(\vec{f_i}, \vec{r_i}) = H^{\mathrm{M}}(\vec{f_i}) + H^{\mathrm{S}}(\vec{r_i}) + H^{\mathrm{int}}(f_i, r_i) \tag{2.33}$$

where the superscripts M and S denote the solute and solvent molecules, respectively, with r_i, f_i degrees of freedom, the third and final term describing their mutual interaction.

To achieve this goal, several quantum chemistry approaches have been developed so far starting from the first decades of the past century and progressively refined. All these approaches share the common features of adopting a method to approximate the general Hamiltonian Eq. 2.33. In fact, in the absence of any approximation, the number of degrees of freedom of the solvent would be so high to make the problem itself untreatable and, by the other hand, will provide an amount of information which in itself is redundant, since the main interest is focused in obtaining an accurate description of the solute, rather than all the exact configurations of the solvent.

According to the approximation introduced at this initial step, all the known approaches can be roughly divided in three main classes: implicit, explicit and mixed solvation models.

In implicit solvation models, usually referred to continuum solvation models, only the molecule of interest is explicitly simulated while the effect of all the surrounding solvent molecules is described in terms of a continuous dielectric medium extending, conceptually, to infinity in all the three dimensions. Under this approximation, the Hamiltonian term $H^S(\vec{r}_i)$ in Eq. 2.33 describing the solvent, simply reduces to a constant and every influence of the medium on the solvated molecules is described in the interaction term, in which the degree of freedom of the solvent are, at this stage, still present in the resulting effective Hamiltonian, according to[23]

$$H^{\text{eff}}(\vec{f}_i, \vec{r}_i) = H^{\text{M}}(\vec{f}_i) + H^{\text{int}}(f_i, r_i) \tag{2.34}$$

It is very common literature to refer to the last term in Eq. 2.34 as the *solvent reaction potential* V^{R} because it can be seen as a perturbation produced by dielectric medium acting on the unperturbed solute Hamitonian describing the quantum mechanical states in vacuo, which can be rewritten in the form

$$H^{\text{eff}} = H_0^{\text{M}} + V^{\text{R}} \tag{2.35}$$

The formulation of the problem of solvation in terms of diagonalization of the effective Hamiltonian composed by an unperturbed H_0^{M} term describing the solute molecule in vacuo and a solvent reaction potential V^{R} can be viewed as an application of the mean field approximation to the complex character of solvation. In the perturbation term, in fact, the effects of different physical processes contributing to the solvation of the M molecule of interest can

be included. These contributions are usually written in a form suitable for a statistical average by properly using the thermally averaged distribution function $g_{\mathrm{S}}(\Omega)$ for the quantity described.

In this perspective, implicit solvation models overcome an aspect which is, in contrast, common in explicit solvation models, where a convenient subset of the solvent molecules (usually the nearest to the solute molecules, konwn as the *first solvation shell*), are explicitly described, posing the problem to sample and then to average *a posteriori* the configuration space describing the entire simulated aggregate.

In implicit model, instead, the averaging is provided in the evaluation of the interaction potential V^{R} using the $g_{\mathrm{S}}(\Omega)$ in a procedure called *charging parameter method*,[23] by introducing an adimensional charging parameter $0 \leq \lambda \leq 1$ to retrieve the reversible coupling work of the solute M in the solvent

$$w = \int_0^1 d\lambda \int d\Omega \rho_{\mathrm{S}}(\lambda) V^{\mathrm{R}}(\Omega, \lambda) g_{\mathrm{S}}(\Omega, \lambda) \tag{2.36}$$

which enters in the general expression[23] of the free energy of solvation ΔG_{sol}

$$\Delta G_{\mathrm{sol}} = w + N_{\mathrm{A}} k_{\mathrm{B}} T \left(\frac{(q_{\mathrm{rot}} q_{\mathrm{vib}})_{\mathrm{gas}}}{(q_{\mathrm{rot}} q_{\mathrm{vib}})_{\mathrm{sol}}} \right) - N_{\mathrm{A}} k_{\mathrm{B}} T \left(\frac{(\Lambda_{\mathrm{M}})_{\mathrm{gas}}}{(\Lambda_{\mathrm{M}})_{\mathrm{sol}}} \right) \tag{2.37}$$

Historically, according to Tomasi et al.,[43] the first attempt to find a solution for the solvation problem mainly addressed to the mathematical formalization and calculation of the electrostatic contribution in V^{R}, which however, it's not unique.

This formulation of the problem can be explained by considering that most of the solvation process of interest usually takes place in water, a strongly polar solvent of huge practical utility as well as biological importance. Furthermore, the energetic contribution of the pure electrostatic interaction between the solute and the dielectric medium can be relatively easy understood in a classical macroscopic framework and the problem can be stated in terms of the mutual influence of charge distributions and polarizabilities.

By modelling the solute molecule as a charge distribution ρ_{M} placed in a cavity embedded in a dielectric bulk (the solvent environment), the electrostatic interaction energy can be in fact represented in the form[44]

$$W_{\mathrm{MS}} = \int_{\Omega} \rho_{\mathrm{M}}(\vec{r}) \Phi(\vec{r}) d^3\vec{r} \tag{2.38}$$

where $\Phi(\vec{r})$ is the electrostatic reaction potential generated by the dielectric medium, originated by the presence of the solute charge distribution ρ_{M} in

the volume Ω of the cavity. The reaction potential is calculated by exploiting the fact that the total potential $V(\vec{r})$, which is the sum of the reaction potential plus the potential generated by the solute itself, must obey the non-homogeneous Poisson equation (NPE)[22]

$$\nabla[\varepsilon(\vec{r})\nabla V(\vec{r})] = -4\pi\rho_{\mathrm{M}}(\vec{r}) \tag{2.39}$$

The equation can be simplified if all the solute distribution charge is contained inside the cavity.

The definition itself of a proper cavity, however, is a problem *per se* and several approaches have been presented in the literature. One of the problems is the fact that even if in the large majority of implicit (continuous) models, the cavity is specifically built around the molecule of interest in order to exactly contain all the charge distribution of the solute, this automatically exclude any overlap between the solvent and solute electronic distribution, which in reality exists and originates quantum effects of relevance. Their contribution to the solvation process is thus recovered by adding to the electrostatic term other non-electrostatic terms. The shape itself, even if reported in literature to play a role in determining the quality of the resulting data, is not univocally determined. However, the most common common approach, as provided in the GEPOL[34] algorithm implemented in Gaussian 16,[14] consists in modelling the surface by a series of interlocked van der Waals spheres. The radii of the spheres are usually, as in SMD solvation model,[25] based both on more sophisticate calculations involving partial charges (intrinsic Coulomb radii) for which a full explanation is beyond the scope of this Thesis. Alternative approaches, based on the use of an isodensity surface with given threshold are possible but seldom adopted.

When a suitable cavity fulfilling the desired properties is built, in the case of isotropic solvent ($\varepsilon(r) = \varepsilon$) the NPE can be reduced to the two equation defined in two spatial domains

$$\begin{aligned} \nabla^2 V(\vec{r}) &= -4\pi\rho_{\mathrm{M}} \quad \text{inside cavity } (\varepsilon = 1) \\ -\varepsilon\nabla^2 V(\vec{r}) &= 0 \qquad\qquad\quad \text{outside} \end{aligned} \tag{2.40}$$

The solution must obey the boundary conditions at infinity and at the cavity surface Γ

$$\begin{aligned} &\lim_{r\to\infty} rV(r) = \alpha \\ &\lim_{r\to\infty} r^2 V(r) = \beta \\ &V_{\Gamma,\mathrm{in}} = V_{\Gamma,\mathrm{out}} \\ &\left(\frac{\partial V}{\partial \vec{n}}\right)_{\Gamma,\mathrm{in}} = \varepsilon \left(\frac{\partial V}{\partial \vec{n}}\right)_{\Gamma,\mathrm{out}} \end{aligned} \tag{2.41}$$

The resolution of the equations Eq. 2.40 represents one of the final step to calculate the electrostatic contribution and can be achieved with a variety of method sharing a common feature, the non-linearity due by the mutual dependence of ρ_{M} and the corresponding electrostatic reaction potential Φ. In order to obtain the solution a self-consistent procedure is thus applied, which justifies the currently adopted name of *self consistent reaction field* for the continuum solvation models.

Among these methods, we will focus on the Integral Equation Formalism Polarizable Continuum Model (IEF-PCM) which we used in Gaussian 16[14] suite of programs to calculate estimates of the Free Reaction Energy for PEDOT polymerization, schematizing the main conceptual steps as reported in the original exposition of Cancès and Tomasi work.

In IEF-PCM, developed on the same conceptual foundations of the previous D-PCM model (Dielectric Polarizable Continuum Model), the key idea is to reproduce the electrostatic reaction potential $\Phi(r)$ by constructing on the cavity surface Γ an auxiliary charge density $\sigma(\vec{s})$ which must fulfil

$$\Phi(r) = \int_{\Gamma} \frac{\sigma(\vec{s})}{|\vec{r} - \vec{s}|} d^2 s \tag{2.42}$$

under the previous stated assumption that no charge is present outside the cavity itself. The use of this definition reduces the solution of equations Eq.2.40 under Eq. 2.41 boundary conditions to the search for a surface charge distribution self consistent with the total electrostatic potential which determines precisely its presence on the cavity surface. It can in fact demonstrated that

$$\sigma(\vec{s}) = \frac{\epsilon - 1}{4\pi\epsilon} \frac{\partial}{\partial \vec{n}} \left(V_{\mathrm{M}} + \Phi\right)_{\vec{s},\mathrm{in}} \tag{2.43}$$

Computational implementation of Eq. 2.42 is achieved by partitioning the Γ surface obtained via GEPOL[34]algorithm in a discrete ensemble of N surface elements (*tesserae*) each one characterized by A_k surface area, sufficiently small to consider $\sigma(\vec{s})$ constant on the entire element. This leads to the replacing of integral into discrete summation

$$\Phi(r) \simeq \sum_{i=1}^{N} \frac{\sigma(\vec{s}_k) A_k}{|\vec{r} - \vec{s}|} = \sum_{i=1}^{N} \frac{q_k}{|\vec{r} - \vec{s}_k|} \tag{2.44}$$

where q_k denotes the charge distributed in the A_k tessera. The set of q_k charges can be determined by an iterative approach which can be summarized in this way. First, using a trial set q_k^{00} (which can be obtained, for example, from ρ_0 arising from a previous DFT calculation in vacuo), a $\Phi^0(r)$

is calculated from Eq. 2.44. By inserting the $\Phi^0(r)$ in Eq. 2.43, properly recasted in the form

$$q_k^{0n} = \frac{\epsilon - 1}{4\pi\epsilon}\vec{\nabla}(V_{\mathrm{M}} + \Phi^n)_{\vec{s},\mathrm{in}} \cdot \vec{n}_k A_k \tag{2.45}$$

a new charge distribution is obtained which gives rise to a new q_k^{01} set. By repeating the cycle for n steps, a final set of q_k^{0n} consistent with the n-th estimate of the potential $\Phi^n(r)$. At this point, the reaction potential is used iteratively in the effective Hamiltonian Eq. 2.35 from which ρ^1 is obtained, and subsequently used for defining q^{10}.

Thus, as we can see, the solution of the problem can be obtained by performing two different SCF cycles, with the cycle for partial charges calculation included in the more general cycle to solve the Hamiltonian Eq. 2.35 performed for a given interaction potential.

The peculiarity of the IEF-PCM in this very general approach to the solution resides in the inner cycle for partial charge calculation: the effect of each iteration starting from q^{00} to q^{0k} can in fact be described in a matricial form[7]

$$\mathbf{q^{0,f}} = -\mathbf{\Sigma D^{-1}} \mathbf{E}_n \tag{2.46}$$

where $\mathbf{q^{0,f}}$ is a vector containing the q_k partial charges, $\mathbf{E}_n$ the corresponding total electric field E_k at each k site. Σ is a diagonal square matrix containing the A_k tesserae areas tesserae and $\mathbf{D}$ a nonsymmetric square matrix with dimension equal to the number of tesserae, which accounts for geometrical cavity parameters, including if necessary corrections for the fact that the charge is not in a single point, and the dielectric constant ϵ.

In IEF-PCM an extensive and crucial use of Green's functions to describe both the solute and solvent reaction field potential makes possible to determine the matrix elements of $\mathbf{\Sigma D^{-1}}$ as combinations of the Caldéron projectors of the Green's functions,[7,29] which can be written in the form reported by Scalmani[38]

$$\begin{aligned}
\hat{S}\sigma(\vec{s}) &= \int_\Gamma \frac{\sigma(\vec{s}')}{|\vec{s} - \vec{s}'|} d^2\vec{s}' \\
\hat{D}^*\sigma(\vec{s}) &= \int \Gamma \left(\frac{\partial}{\partial \hat{n}_\mathrm{s}} \frac{1}{|\vec{s} - \vec{s}'|} \right) \sigma(\vec{s}') d^2\vec{s}' \\
\hat{D}\sigma(\vec{s}) &= \int \Gamma \left(\frac{\partial}{\partial \hat{n}'_\mathrm{s}} \frac{1}{|\vec{s} - \vec{s}'|} \right) \sigma(\vec{s}') d^2\vec{s}'
\end{aligned} \tag{2.47}$$

which are identified as the electrostatic potential, the normal component of the electric field and the integral of the normal field evalueated at the surface of the cavity Γ.[38]

It's important to note that, how stated in,[7,29] the IEFPCM formally reduces to the D-PCM approach in the case of isotropic dielectrics but it's very useful and general if applied to anisotropic and polar and ionic solutions, where the properties of the dielectric medium are described in terms of a tensor instead of a scalar.

In the latter more complex cases, it have been demonstrated that the charge distribution can be obtained from the more general matricial equation[7,29]

$$\mathbf{A}\sigma = \mathbf{g} \tag{2.48}$$

with the dependence from the electric field and potential contained in the $\mathbf{g}$ vector and σ vector containing the charge density at each single tessera. It also possible and useful to impose appropriate conditions in order to retain only the dependence from electrostatic potential generated by the solute molecule V_{M} in $\mathbf{g}$, a choice which leads to a reduction of computational power required, increased stability in solving implicitly correct the discrepancies arising from outlying charge.

In conclusion, resolution of Eq, 2.48 represents the most inner cycle for the two step SCF procedure: after solution for σ are find, in fact, it is possible to evaluate the electrostatic interaction term which is present in Eq. 2.35, and obtain a new value for V_{M} used to update the $\mathbf{g}$ vector until full self consistency is reached.

The electrostatic contribution to the free energy of solvation (electrostatic free energy) ΔG_{el} is finally calculated as the difference[44]

$$\Delta G_{\mathrm{ele}} = G_{\mathrm{ele}} - E_0 \tag{2.49}$$

where E_0 is the ground state energy of the isolated solute in vacuo and G_{ele} is obtained by constrained minimization, using Lagrange multipliers, of the functional[45]

$$G_{\mathrm{ele}}[\Psi] = \langle\Psi|H_0 - \frac{\Phi}{2}|\Psi\rangle \tag{2.50}$$

the factor $\frac{1}{2}$ being introduced to take into account only the reversible component of the total work done to introduce the solute charge density in the embedding dielectric, half of which is sent to polarize the dielectric itself and cannot be recovered by simply removing the charge distribution.

By choosing an appropriate $\{\chi\}_{\mathrm{n}}$ basis set, the problem stated in Eq. 2.50 can be converted in the diagonalization of the corresponding Fock matrix.

2.1.5 Non-electrostatic terms

As pointed out in introducing a brief explanation of the electrostatic contribution calculation resume, the interaction potential is usually seen as

the sum of different components, reflecting the main forces involved in the reversible coupling work of solute and solvent.

It is important, at this point, to premise that it is known in literature that the partitioning usually done is not a well posed problem from a theoretical point of view, since several coupling exists between each component and only the sum of all the contributions give rises to a meaningful state function, a properties which do not apply to the components taken separately.

However, as clearly stated in Truhlar's work, this does not represent necessarily a great inconvenient from a practical point of view, because many non electrostatic contribution and the definition itself of the cavity can be adjusted in order to partly re-absorb the missing contribution of the couplings.

This approach has conducted to the formulation of several solvation models, as the SMD model[25] which we used in our study, that can successfully reproduce experimental data despite the apparent theoretical limits.

The main contribution generally grouped under the label of "non electrostatic terms" and it can be shown that, in a many-body expansion, they arises from three-body terms in calculation of global interaction energy.[43] The most relevant contributions, according to the standard partitioning,[23] are

- cavitation energy;
- repulsion energy;
- dispersion energy

The cavitation contribution represents the energy which has to be spend in order to build the cavity in the dielectric bulk in which the solute molecule is contained. As stated in Tomasi et al, it can be conceived as the sum of the work done to create the cavity and the enthalpic variation linked to the resulting reorganization of the solvent molecules. All the process of cavity creation is done, according the charging parameter scheme, assuming all other form of interaction absent.

The repulsion energy can be successively calculated as the correction energy resulting from requiring the global antisymmetry of the wavefunction describing the system. This term, always repulsive and decaying as r^{-12}, arises from the overlap of the solute and solvent wavefunction, correcting an approximation assumed in the calculation of the electrostatic contributions, i.e. the complete absence of charge density outside the cavity.

The energy dispersion, finally, describes the stabilizing effects of the formation of instantaneous dipole moments: its contribution is always negative

as decays as r^{-6} and in first works, as in Pierotti's one,[36] it can be estimated simultaneously with repulsion by using Lennard-Jones potential for take into account interatomic interactions.

An important characteristic of the non electrostatic terms is the fact that they can be written in a form which explicitly depends on the solvent accessible surface (SAS)[23] via a set of semi-empirical parameters leading to values very close to complete the experimental free energies of solvation.

Truhlar's et al SMD model,[25] suggested by Gaussian 16[14] as the currently recommended choice for solvation energies calculation, largely exploits the possibility to fine tuning non electrostatic contribution related parameter in order to provide, according to the authors, an approach which can be considered universal, i.e. suitable to successfully describe solutes both neutral or charged in terms of easy accessible solvent macroscopic properties.

The model relies on the partition of the solvation free energy in sum

$$\Delta G_{\mathrm{sol}} = \Delta G_{\mathrm{ENP}} + G_{\mathrm{CDS}} + \Delta G_{\mathrm{c}}^{0} \tag{2.51}$$

where electrostatic effects are included in the first ΔG_{ENP} term (with ENP acronym to recall the electronic, nuclear and polarization contribution) and cavitation, repulsion-dispersion and structural solvent modifications included in the second G_{CDS} term, the final term taking into account energetic contribution from changes in concentration from gas to liquid phase, if required.

The electrostatic contribution are calculated in the framework of the IEF-PCM model using a cavity build as overlapping, nuclear-centered spheres with an optimized radius, depending on the partial charges and called intrinsic Coulomb radii.

Non electrostatic term is formulated as combination of surface areas atom-dependent areas and two set of parameters, atomic and molecular surface tension and include a different set of radii known in literature as Bondi's radii.

Atomic and molecular and surface tension are expressed as combinations of several quantities of particular interest. In fact, the atomic surface tension is written as a combination of the refractive index, Abraham's hydrogen bond acidity and basicity, while the molecular surface tension is written as function of the macroscopic surface tension for the solvent-air interface and the fraction of aromatic carbons and halogens. The coefficients entering in the formulation of both these surface tensions are properly fit using a very large training set of reference solvent and solute mixture, resulting in a final model which posses an average error on solvation energies of few kcal mol^{-1}.[25]

2.2 Classical Molecular Dynamics (MD)

2.2.1 Theoretical background

As described in Section 2.1, DFT has radically modified the last development of computational quantum mechanics by allowing the simulation of larger molecular aggregates with a computational effort significantly lower compared to other Hartree-Fock and post-HF methods.

It is important, however, to clearly note that DFT alone does not represent the final receipt to simulate every kind of system at a quantum mechanical level. The computational efforts required to simulate larger and larger systems rapidly increases with the number of atoms and thus the number of basis function describing the KS operator. For this reason, pure quantum mechanical simulations are usually limited in time or in the system size, a circumstance which can represent an issue in the study of complex atomic structures, as the intricate topology of organic polymers.

A possible way to overcome this intrinsic limitations not only of DFT but of all ab-initio techniques is provided by Classical Molecular Dynamics (MD), and have its origins in the same Born-Oppenheimer approximation[5] used to simplify Schrödinger equation in the same formulation of DFT.

At a very fundamental level, in fact, Born-Oppenheimer approximation can be reduce to the statement that electronic and nuclear motion are characterized by completely different timescales, implying that the evolution of a system in the limit of very long times is usually not influenced by the instantaneous state of the electrons but rather from their average, i.e. time-averaged, evolution.

The core of Classical MD resides precisely in finding a proper way to construct meaningful and useful averages of properties emerging from the electronic state of each aggregate and include them in a scheme in which only atomic nuclei are explicitly simulated with trajectories following the laws of Classical Dynamics.

This approach, in which all quantum mechanical details of the investigated system are not lost but re-summed into simulation specific parameters, as the bond average lengths and force-constants, allows to significantly reduce the computational resources needed to produce realistic and larger atomic aggregates and makes possible to investigate the behavior at timescales up to hundred (also thousand) of nanoseconds ($\sim 10^{-7}$s), several order of magnitudes above the typical electronic processes times ($\sim 10^{-12}$s).

Regardless the involved procedure adopted, classical Molecular Dynamics is based on the assumption that, in a model system with N atoms, the ith

atom, treated as a point particle, experiences a force $\vec{F}_i$ which is the gradient of a given potential energy U_i evaluated at the position of the ith particle

$$\vec{F}_i = -\vec{\nabla} U_i \tag{2.52}$$

From $\vec{F}_i$ the acceleration $\vec{a}_i$ is then calculated according to Newton's second law of dynamics and numerically integrated respect to time t in order to give the instantaneous velocity $\vec{v}_i$ and position $\vec{r}_i$ of each atom. The sampling unit Δt named timestep is used to discretize the whole simulation time T in order to numerically solve the Newton's equations.

Several integration schemes are possible to achieve this goal. One of the most frequently used is the velocity-Verlet algorithm, based on three Taylor expansions involving the timestep Δt to update the positions $\boldsymbol{r}_i$ and the velocities $\boldsymbol{v}_i$

$$\begin{aligned} \boldsymbol{r}_i(t+\Delta t) &= \boldsymbol{r}_i(t) + \Delta t\ \dot{\boldsymbol{r}}_i(t) + (\Delta t)^2 \frac{\ddot{\boldsymbol{r}}_i(t)}{2} + o((\Delta t)^3) \\ &= \boldsymbol{r}_i(t) + \Delta t\ \boldsymbol{v}_i(t) + (\Delta t)^2 \frac{\boldsymbol{F}_i(t)}{2m_i} + o((\Delta t)^3) \end{aligned} \tag{2.53}$$

$$\begin{aligned} \boldsymbol{v}_i(t+\Delta t) &= \boldsymbol{v}_i(t) + \Delta t\ \dot{\boldsymbol{v}}_i + (\Delta t)^2 \frac{\ddot{\boldsymbol{v}}_i}{2} + o((\Delta t)^3) \\ &= \boldsymbol{v}_i(t) + \Delta t\ \frac{\boldsymbol{F}_i(t)}{m_i} + (\Delta t)^2 \frac{\ddot{\boldsymbol{v}}_i(t)}{2} + o((\Delta t)^3) \end{aligned} \tag{2.54}$$

To maintain the $o((\Delta t)^3)$ accuracy, the second time derivative of each velocity $\ddot{\boldsymbol{v}}_i(t)$ is calculated in terms of the acceleration $\dot{\boldsymbol{v}}_i$ using the forward difference

$$\ddot{\boldsymbol{v}}_i = \frac{\dot{\boldsymbol{v}}_i(t+\Delta t) - \dot{\boldsymbol{v}}_i(t)}{\Delta t} + o((\Delta t)^3) = \frac{1}{m_i\ \Delta t}(\boldsymbol{F}_i(t+\Delta t) - \boldsymbol{F}_i(t)) + o((\Delta t)^3) \tag{2.55}$$

Eq. 2.54 is thus restated as

$$\boldsymbol{v}_i(t+\Delta t) = \boldsymbol{v}_i(t) + \frac{\Delta t}{2m_i}(\boldsymbol{F}_i(t+\Delta t) + \boldsymbol{F}_i(t)) + o((\Delta t)^3) \tag{2.56}$$

The system made up by the two equations Eq. 2.53 and Eq. 2.56 represents the core of the velocity-Verlet algorithm, and is computationally implemented using the following cyclic scheme to update positions and velocities.

Given the initial $\boldsymbol{r}_i(t)$, $\boldsymbol{v}_i(t)$ and the forces $\boldsymbol{F}_i(t)$

1. positions are updated to $\boldsymbol{r}_i(t+\Delta t)$ using Eq. 2.53;

2. the new forces $\boldsymbol{F}_i(t+\Delta t)$ are calculated as $\boldsymbol{F}_i = -\boldsymbol{\nabla} U_i$ without overwriting the previous $\boldsymbol{F}_i(t)$ values;

3. velocities are updated to $\boldsymbol{v}_i(t+\Delta t)$ using Eq. 2.56.

The cyclic instruction are repeated m times, m being the ratio between the total simulation time T and the timestep Δt.

A choice particularly important in the computational setup for MD simulations is the choice of the timestep Δt. In order to achieve the highest possible accuracy, the integration of the motion equation should require a timestep as little as possible. However, this choice is not computationally feasible since it would require very long simulation times. By contrast, excessive large values for Δt are related to a global numerical instability of the whole simulation.[17] A good criterion[9] is represented by taking the largest vibrational typical frequency $\nu_{\max}$ of the system and to set Δt as

$$\Delta t < \frac{1}{\nu_{\max}} \tag{2.57}$$

2.2.2 Force fields

As clearly expressed in Eq. 2.52, the key ingredient of every Classical MD simulation is the potential energy U_i calculated at each ith atomic position resulting from the mutual interactions of the N atoms in the system.

The functional form as well as the parametrization of the overall function U is referred to as force field.

Several interactions are usually considered to describe accurately the behavior of large aggregates of atoms, arising not only from pure quantum mechanical effects, as the specific characteristic of a chemical bond, but also by forces which can described classically, as long range Coulombic interaction.

A common practice adopted in the parametrization of all force fields is to break down the overall potential energy U as the sum of these different contributions, and distinguishing between short-range and long-range interactions. Short-range contributions are referred to as bonding terms and long-range interactions are described as non-bonding. The U functions is thus written as

$$U = U^{\text{bonded}} + U^{\text{non-bond}} \tag{2.58}$$

The U^{bond} term can be written as the sum of three many-body functions associated with the properties of the covalent bond between interacting atoms, namely

$$U^{\text{bonded}} = U^{\text{bonds}} + U^{\text{angles}} + U^{\text{torsion}} \tag{2.59}$$

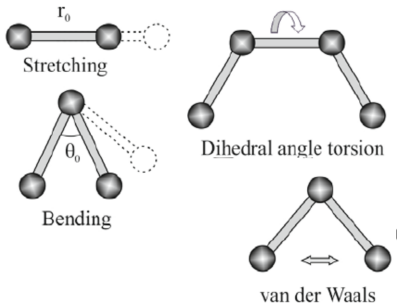

Figure 2.1: Schematic representation of the main terms of AMBER force field (adapted from Ref.[31])

where U^{bonds}, U^{angles} and U^{torsion} are a 2-, 3- and 4-body functions.

The functional form of the n-body function is used to divide the force fields in two main classes, I and II.

In Class I force-fields, the motion of atoms is treated using the harmonic approximation. These force fields, in which the bond and angle term are quadratic, are frequently used to model organic systems.

In Class II force-fields, high order to correction to the harmonic approximation, mainly cubic terms, are introduced to include the effects of anharmonicity.

AMBER[8] is a Class I force-field, the harmonic approximation is used to describe the motion of the atoms around their equilibrium positions and under the influence of the bonding, short-range interactions and the three terms in Eq. 2.59 are written as

$$\begin{aligned} U^{\text{bonds}} &= \sum_{i}^{n_b} k_i (r_i - r_i^{\text{eq}})^2 \\ U^{\text{angles}} &= \sum_{i}^{n_a} q_i (\theta_i - \theta_i^{\text{eq}})^2 \\ U^{\text{torsion}} &= \sum_{i}^{n_t} w_i (1 + \cos(n\phi_i - \phi_i^{\text{eq}})) \quad (n \text{ integer}) \end{aligned} \tag{2.60}$$

where k_i, q_i, w_i are numerical coefficients obtained by fitting from experimental data or computational estimates, r_i the inter-atomic distance between two atoms, θ_i the angle formed by 3 bounded atoms and ϕ the dihedral angle between 4 bounded atoms. The sums in Eq. 2.60 run on the total number of bonds, angles and dihedrals, respectively.

The n integer entering in torsional contribution accounts for the n-fold periodicity interaction, reflecting the intrinsic symmetry in the dihedral angle.

Two long-range non-bonding contribution constitutes the $U^{\text{non-bond}}$ in Eq.2.58, the electrostatic (Coulombic) potential and the Lennard-Jones energy

$$U^{\text{non-bond}} = U^{\text{elec}} + U^{\text{LJ}} \tag{2.61}$$

which are calculated in terms of the mutual r_{ij} distance between the ith and the jth atom constituting an unbounded pair as, respectively,

$$\begin{aligned} U^{\text{elec}} &= \sum_{\text{non-bond}} \frac{q_i q_j}{r_{ij}} \\ U^{\text{LJ}} &= \sum_{\text{non-bond}} 4\varepsilon_{ij} \left(\frac{\sigma_{ij}}{r_{ij}^{12}} - \frac{\sigma_{ij}}{r_{ij}^{6}} \right) \end{aligned} \tag{2.62}$$

where q_i, q_j are the fixed partial charges of the involved atoms and ε, σ the numerical coefficients accounting for repulsive interaction from exclusion principle ($\sim r^{-12}$) and dispersion (or van der Waals) term ($\sim r^{-6}$).

2.2.3 Thermostats and barostats

One of the most interesting properties of velocity-Verlet integration scheme is its symplectic nature, a term describing the fact that the volume of the N-atom system in phase space is conserved during the dynamical evolution.

As consequence, the total energy $E = K + U$, the sum of the kinetic K and potential U energies, is conserved with great accuracy. The properties of the system arising from statistical averages are thus well-described in the framework of the microcanonical ensemble, where the total number N, the volume V and E are fixed at their initial values (for this reason, this ensemble is also referred to as NVE).

Unfortunately, the NVE ensemble very rarely reproduce the experimental conditions in which the properties of interest are measured. In these cases. in fact, one or more intensive thermodynamical properties of the sample are usually fixed, as the temperature T or the pressure p.

In order to reproduce in classical MD simulations this conditions, a possible approach is constituted by the introduction of additional terms in the global Hamiltonian $\hat{\mathcal{H}}$, a methodology called extended Lagrangian formalism. These modifications to $\hat{\mathcal{H}}$ implies the introduction of a fictitious drag term ξ in Eq. 2.52 to correct the accelerations $\ddot{\boldsymbol{r}}_i$ as

$$\ddot{\boldsymbol{r}}_i = \frac{\boldsymbol{F}_i}{m_i} - \frac{\xi}{m_i} \dot{\boldsymbol{r}}_i \tag{2.63}$$

where the functional form of ξ is derived directly from the corrections applied to $\hat{\mathcal{H}}$.

As case of particular interest, to keep T temperature constant in a N atom system with V volume (NVT or canonical ensemble), the ξ parameter as derived in the formulation of Nosé and Hoover (the so-called NH thermostat) must obey the differential equation

$$\frac{d\xi}{dt} = \frac{\sum_i v_i^2 - 3Nk_{\mathrm{B}}T_r}{Q} \tag{2.64}$$

where T_r is the target temperature, v_i the modulus of the velocities of the particles and Q the mass associated with the s additional degree of freedom added in $\hat{\mathcal{H}}$ to describe the heat bath in a system with g independent momentum-degrees of freedom

$$\hat{\mathcal{H}} = \sum_i \frac{\boldsymbol{p}_i^2}{2m_i s^2} + \frac{1}{2}\sum_{i\neq j} U_{ij} + \frac{p_s^2}{2Q} + gk_{\mathrm{B}}T\log(s) \tag{2.65}$$

In many software suites used for classical MD simulations, as LAMMPS, the entity of M can be regulated via a damping or relaxation time τ, which is generally recommended to set at $\sim 100\Delta t$.

The overall Nosé-Hoover dynamics, generating trajectories in accordance with the canonical distribution for a system at temperature T, results to be determined by the set of equations involving the generalized momenta and coordinates p_i, q_i

$$\begin{aligned}
\dot{p}_i &= -\frac{\partial V(\boldsymbol{q})}{\partial q_i} - \frac{p_i p_\eta}{Q} \\
\dot{q}_i &= \frac{p_i}{m_i} \\
\dot{p}_\eta &= \sum_{i=1}^{N} \frac{p_i^2}{m_i} - Nk_{\mathrm{B}}T \\
\dot{\eta} &= \frac{p_\eta}{Q}
\end{aligned} \tag{2.66}$$

A significant improvement in accuracies is obtained if the single thermostat in original NH approach is replaced by a chain of M coupled thermostats, each one with its own Q_M inertia. Only the first (j=1) thermostat in the constructed chain interacts directly with the N-particle system, the jth one (for $j > 1$) interacting only with its two neighbours $j-1, j+1$ in the chain.

It can be shown[27] that the dynamical equations for the generalized momenta p_i and p_η are modified in

$$\begin{aligned}
\dot{p}_i &= -\frac{\partial V(\boldsymbol{q})}{\partial q_i} - \frac{p_i p_{\eta_{(1)}}}{Q_1} \\
\dot{p}_{\eta_{(1)}} &= \sum_{i=1}^{N} \frac{p_i^2}{m_i} - N k_{\mathrm{B}} T - \frac{p_{\eta_{(1)}} p_{\eta_{(2)}}}{Q_2} \\
\dot{p}_{\eta_{(j)}} &= \frac{p_{\eta_{(j-1)}}^2}{Q_{j-1}} - k_{\mathrm{B}} T - \frac{p_{\eta_{(j)}} p_{\eta_{(j+1)}}}{Q_{j+1}} \quad \text{for } 1 < j < M \\
\dot{p}_{\eta_{(M)}} &= \frac{p_{\eta_{(M-1)}}^2}{Q_{M-1}} - k_{\mathrm{B}} T
\end{aligned} \tag{2.67}$$

A similar approach can be applied to set constant the system pressure (giving the NH barostat) allowing to generate results consistent with isothermal-isobaric ensemble (NPT).

2.3 Marcus theory

The elementary process in which an electron is exchanged between two distinct molecular aggregates following the basic scheme

$$\mathrm{D}_{\mathrm{sol}}^{-} + \mathrm{A}_{\mathrm{sol}}^{+} \rightleftharpoons \mathrm{D}_{\mathrm{sol}}^{+} + \mathrm{A}_{\mathrm{sol}}^{-} \tag{2.68}$$

is conventionally referred to as electron-transfer reaction between a donor D and an acceptor A in the common solvent environment.

The construction and rigorous formalization of electron-transfer reactions in the framework of the Quantum Mechanics is of paramount importance to understand a very large class of evidences from biochemical, chemical and physical experiments, a goal which has been successfully achieved mainly by the Nobel laureate Rudolph Marcus in the past century.

In this Section, the key points and most important ingredient which have been used in Chapter 5 to estimate the electrical conductivity of realistic PEDOT samples are summarized, reminding to the vast literature available[2,3,32] for a deeper understanding.

Referring to Eq.2.68, the starting point for the derivation of Marcus hopping rate κ, defined as the frequency at which each elementary electron transfer takes place, is the recognition of the importance of fluctuations of atomic coordinates of the donor and the acceptor molecule as well as the surrounding solvent molecules.

The energetic balance related to the hopping process of a charge, in fact, includes not only the individual contribution from the donor and the acceptor

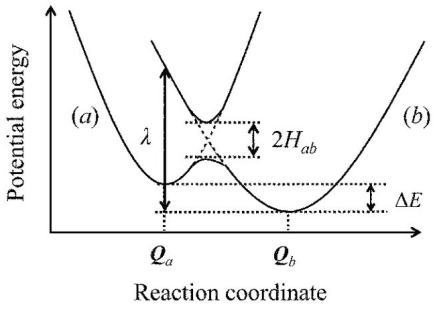

Figure 2.2: Schematic representation of the Marcus' parabolae for the general redox in Eq. 2.68[40]

but also the non-negligible cost of the reorganization of the orientational degree of freedom of the solvent molecules, which is particularly important when the process occurs in a polar solvent as water.

Relying on a specific application of BO approximation to the molecular case, the Franck-Condon principle, the specific state of the system in Eq. 2.68 before and after the charge transfer is studied in terms of the nuclear coordinates q_i, implicitly depending on the electronic wavefunction.

To give a visual representation of the method, usually the $E(q_i)$ surface, which is in principle a function of all the N atomic degrees of freedom (including the surrounding solvent molecules), is plotted for the special case of a single variable function E_q, in the form of two displaced parabolae (as in Fig. 2.2 for the case in Eq. 2.68)

The intersection point between the reactants and products parabolae determines the overall hopping rate κ, which can be stated in the form[24]

$$\kappa = \kappa_0 \exp\left(-\frac{\Delta G^\dagger}{k_B T}\right) \tag{2.69}$$

where κ_0 prefactor is determined, essentially, by the overlap of the electronic wavefunctions of D and A and $\Delta G^\dagger$ the Gibbs free energy of activation.

For most applications, the hopping rate in Eq. 2.69 reads as[24]

$$\kappa_0 = \frac{2\pi}{\hbar}|H_{AD}|^2 \sum_\omega \zeta_\omega p(\omega) \tag{2.70}$$

where H_{AD} is the charge transfer integral, ζ the Franck-Condon factor for the vibrational frequency ω multiplied for its corresponding probability $p(\omega)$.

At this point, by treating all the nuclear coordinates q_i of the reactants in terms of harmonic quantum oscillators and the solvent environment ori-

entational contribution classically, Eq. 2.70 can be recasted[24] in the form

$$\kappa = \frac{2\pi}{\hbar} \frac{|H_{\mathrm{AD}}|^2}{\sqrt{4\pi\lambda k_{\mathrm{B}} T}} \exp\left(-\frac{(\Delta G_0 + \lambda)^2}{4\lambda k_{\mathrm{B}} T}\right) \tag{2.71}$$

where ΔG_0 is the Gibbs free energy of reaction and λ the reorganization energy, a contribution associated with transition of each molecules in Eq. 2.68 from one E_{q_i} hypersurface to the other, as explained in detail in Chapter 5.

Bibliography

[1] La meccanica ondulatoria di un atomo con un campo centrale non coulombiano. parte i. teoria e metodi. *Raccolta di articoli per il complesso didattico-metodico elettronico multimediale sulla disciplina guillemotleft fisica dell'atomo e fenomeni atomici guillemotright / otv. ed. Shundalov MB; BSU, Facoltà di Fisica.*

[2] Vincenzo Balzani. *Electron transfer in chemistry.* Vch Verlagsgesellschaft Mbh, 2001.

[3] Paul F Barbara, Thomas J Meyer, and Mark A Ratner. Contemporary issues in electron transfer research. *The Journal of Physical Chemistry*, 100(31):13148–13168, 1996.

[4] A. D. Becke. Density-functional exchange-energy approximation with correct asymptotic behavior. *Phys. Rev. A*, 38:3098–3100, Sep 1988.

[5] Max Born and Robert Oppenheimer. Zur quantentheorie der molekeln. *Annalen der physik*, 389(20):457–484, 1927.

[6] Brian Harold Bransden, Charles Jean Joachain, and Theodor J Plivier. *Physics of atoms and molecules.* Pearson education, 2003.

[7] E Cances, Benedetta Mennucci, and J Tomasi. A new integral equation formalism for the polarizable continuum model: Theoretical background and applications to isotropic and anisotropic dielectrics. *The Journal of chemical physics*, 107(8):3032–3041, 1997.

[8] DA Case, IY Ben-Shalom, SR Brozell, DS Cerutti, TE Cheatham III, VWD Cruzeiro, TA Darden, RE Duke, D Ghoreishi, MK Gilson, et al. Amber 2018; 2018. *University of California, San Francisco.*

[9] Jong-In Choe and Byungchul Kim. Determination of proper time step for molecular dynamics simulation. *Bulletin of the Korean Chemical Society*, 21, 04 2000.

[10] Christopher J Cramer. *Essentials of computational chemistry: theories and models*. John Wiley & Sons, 2013.

[11] R. Ditchfield, W. J. Hehre, and J. A. Pople. Self-consistent molecular-orbital methods. ix. an extended gaussian-type basis for molecular-orbital studies of organic molecules. *The Journal of Chemical Physics*, 54(2):724–728, 1971.

[12] Enrico Fermi. Un metodo statistico per la determinazione di alcune priorieta dell'atomo. *Rend. Accad. Naz. Lincei*, 6(602-607):32, 1927.

[13] V Fock. „selfconsistent field "mit austausch für natrium. *Zeitschrift für Physik*, 62(11-12):795–805, 1930.

[14] M. J. Frisch, G. W. Trucks, H. B. Schlegel, G. E. Scuseria, M. A. Robb, J. R. Cheeseman, G. Scalmani, V. Barone, G. A. Petersson, H. Nakatsuji, X. Li, M. Caricato, A. V. Marenich, J. Bloino, B. G. Janesko, R. Gomperts, B. Mennucci, H. P. Hratchian, J. V. Ortiz, A. F. Izmaylov, J. L. Sonnenberg, D. Williams-Young, F. Ding, F. Lipparini, F. Egidi, J. Goings, B. Peng, A. Petrone, T. Henderson, D. Ranasinghe, V. G. Zakrzewski, J. Gao, N. Rega, G. Zheng, W. Liang, M. Hada, M. Ehara, K. Toyota, R. Fukuda, J. Hasegawa, M. Ishida, T. Nakajima, Y. Honda, O. Kitao, H. Nakai, T. Vreven, K. Throssell, J. A. Montgomery, Jr., J. E. Peralta, F. Ogliaro, M. J. Bearpark, J. J. Heyd, E. N. Brothers, K. N. Kudin, V. N. Staroverov, T. A. Keith, R. Kobayashi, J. Normand, K. Raghavachari, A. P. Rendell, J. C. Burant, S. S. Iyengar, J. Tomasi, M. Cossi, J. M. Millam, M. Klene, C. Adamo, R. Cammi, J. W. Ochterski, R. L. Martin, K. Morokuma, O. Farkas, J. B. Foresman, and D. J. Fox. Gaussian 16 Revision C.01, 2016. Gaussian Inc. Wallingford CT.

[15] Douglas Rayne Hartree. The wave mechanics of an atom with a non-coulomb central field. part ii. some results and discussion. In *Mathematical Proceedings of the Cambridge Philosophical Society*, volume 24, pages 111–132. Cambridge University Press, 1928.

[16] Pierre Hohenberg and Walter Kohn. Inhomogeneous electron gas. *Physical review*, 136(3B):B864, 1964.

[17] Sangrak Kim. Issues on the choice of a proper time step in molecular dynamics. *Physics Procedia*, 53:60–62, 12 2014.

[18] W. Kohn and L. J. Sham. Self-consistent equations including exchange and correlation effects. *Phys. Rev.*, 140:A1133–A1138, Nov 1965.

[19] Lev Davidovich Landau and Evgenii Mikhailovich Lifshitz. *Quantum mechanics: non-relativistic theory*, volume 3. Elsevier, 2013.

[20] Chengteh Lee, Weitao Yang, and Robert G. Parr. Development of the colle-salvetti correlation-energy formula into a functional of the electron density. *Phys. Rev. B*, 37:785–789, Jan 1988.

[21] Mel Levy. Universal variational functionals of electron densities, first-order density matrices, and natural spin-orbitals and solution of the v-representability problem. *Proceedings of the National Academy of Sciences*, 76(12):6062–6065, 1979.

[22] Kenny B Lipkowitz and Donald B Boyd. *Reviews in Computational Chemistry 6*. Wiley Online Library, 1995.

[23] F Javier Luque, C Curutchet, J Munoz-Muriedas, A Bidon-Chanal, I Soteras, A Morreale, JL Gelpi, and Modesto Orozco. Continuum solvation models: Dissecting the free energy of solvation. *Physical Chemistry Chemical Physics*, 5(18):3827–3836, 2003.

[24] R.A. Marcus and Norman Sutin. Electron transfers in chemistry and biology. *Biochimica et Biophysica Acta (BBA) - Reviews on Bioenergetics*, 811(3):265 – 322, 1985.

[25] Aleksandr V Marenich, Christopher J Cramer, and Donald G Truhlar. Universal solvation model based on solute electron density and on a continuum model of the solvent defined by the bulk dielectric constant and atomic surface tensions. *The Journal of Physical Chemistry B*, 113(18):6378–6396, 2009.

[26] Richard M Martin. *Electronic structure: basic theory and practical methods*. Cambridge university press, 2020.

[27] Glenn J. Martyna, Michael L. Klein, and Mark Tuckerman. Nosé–hoover chains: The canonical ensemble via continuous dynamics. *The Journal of Chemical Physics*, 97(4):2635–2643, 1992.

[28] A. D. McLean and G. S. Chandler. Contracted gaussian basis sets for molecular calculations. i. second row atoms, z=11–18. *The Journal of Chemical Physics*, 72(10):5639–5648, 1980.

[29] Benedetta Mennucci, E Cances, and J Tomasi. Evaluation of solvent effects in isotropic and anisotropic dielectrics and in ionic solutions with a unified integral equation method: theoretical bases, computational implementation, and numerical applications. *The Journal of Physical Chemistry B*, 101(49):10506–10517, 1997.

[30] Burkhard Miehlich, Andreas Savin, Hermann Stoll, and Heinzwerner Preuss. Results obtained with the correlation energy density functionals of becke and lee, yang and parr. *Chemical Physics Letters*, 157(3):200 – 206, 1989.

[31] Amin Nickkholgh and Parya Keyvani. Finite element modeling of two different cnt/polymer composites: Cnt/pmma and cnt/pmpv. *2011 IEEE Nanotechnology Materials and Devices Conference, NMDC 2011*, 10 2011.

[32] Abraham Nitzan. *Chemical dynamics in condensed phases: relaxation, transfer and reactions in condensed molecular systems*. Oxford university press, 2006.

[33] Robert G Parr. Density functional theory of atoms and molecules. In *Horizons of quantum chemistry*, pages 5–15. Springer, 1980.

[34] Juan Luis Pascual-Ahuir and Estanislao Silla. Gepol: An improved description of molecular surfaces. i. building the spherical surface set. *Journal of Computational Chemistry*, 11(9):1047–1060, 1990.

[35] Lucjan Piela. *Ideas of quantum chemistry*. Elsevier, 2006.

[36] Robert A Pierotti. Aqueous solutions of nonpolar gases1. *The Journal of Physical Chemistry*, 69(1):281–288, 1965.

[37] B. Roos. A new method for large-scale cl calculations. *Chemical Physics Letters*, 15(2):153 – 159, 1972.

[38] Giovanni Scalmani and Michael J Frisch. Continuous surface charge polarizable continuum models of solvation. i. general formalism. *The Journal of chemical physics*, 132(11):114110, 2010.

[39] P. J. Stephens, F. J. Devlin, C. F. Chabalowski, and M. J. Frisch. Ab initio calculation of vibrational absorption and circular dichroism spectra

using density functional force fields. *The Journal of Physical Chemistry*, 98(45):11623–11627, 1994.

[40] Yuta TAKADA, Masaki Okoshi, Minoru HOSHINO, Ishikawa Atsushi, Makoto ISIKAWA, and Hiromi Nakai. Theoretical study on excess-electron transfer in dna based on the marcus theory. *Journal of Computer Chemistry, Japan*, 13:242–249, 01 2014.

[41] Edward Teller. On the stability of molecules in the thomas-fermi theory. *Rev. Mod. Phys.*, 34:627–631, Oct 1962.

[42] Llewellyn H Thomas. The calculation of atomic fields. In *Mathematical Proceedings of the Cambridge Philosophical Society*, volume 23, pages 542–548. Cambridge University Press, 1927.

[43] Jacopo Tomasi, Rosanna Bonaccorsi, Roberto Cammi, and Francisco J Olivares del Valle. Theoretical chemistry in solution. some results and perspectives of the continuum methods and in particular of the polarizable continuum model. *Journal of Molecular Structure: THEOCHEM*, 234:401–424, 1991.

[44] Jacopo Tomasi and Maurizio Persico. Molecular interactions in solution: an overview of methods based on continuous distributions of the solvent. *Chemical Reviews*, 94(7):2027–2094, 1994.

[45] Sigeo Yomosa. Theory of the excited state of molecular complex in solution. *Journal of the Physical Society of Japan*, 36(6):1655–1660, 1974.

Chapter 3

Computational approach to PEDOT polymerization

3.1 Chapter outline

The conceptual backbone of computational simulations of PEDOT polymerization is based on (i) accurate evaluations of the Gibbs free energies and (ii) a reactive Molecular Dynamics (MD) step in which chain growth and spatial reorganization take place, eventually in a concurrent dynamic.

In this Chapter data production protocol and validation are presented, followed by the description of the results and the proposed interpretation.

Initially, the computational implementation for Gibbs free energies ΔG calculations is presented, followed by the results of trial calculations performed to assess the validity of the method.

The $\Delta G(n)$ for PEDOT polymerization is then calculated as a function of the final chain length of the product expressed in monomeric units n and the results are compared with the available experimental data.

The inclusion of ΔG in the polymerization algorithm, which allows to include the DFT description of the process in the context of a Molecular Dynamics (MD) simulations is then presented. The computational results for the characterization of the micromorphologies of the final samples and the comparison of XRD simulated spectra are the topic of the last two sections.

3.2 Ab-initio approach to the polymerization

In order to overcome the problems represented by the energy barriers and the absence of an experimental information to definitely clarify the nature of

proton scavenger identity, we focused only on the global energetic balance of the reaction, getting rid of the kinetics (and so long, of the barriers, which are however still important): in other term, we focused on the stationary state, assuming that all the barriers are overcome.

By means of DFT calculations, as explained in Section 1.3, we evaluated the Gibbs Free Energy variation for the reaction previously described and using different combination of molecules as proton scavengers. In order to achieve this goal, the Gibbs Free Energy evaluated for each isolated molecule in vacuum is corrected by adding additional terms taking into account its interaction with the solvent, namely the ethanol. Since polymerisation proceeds spontaneously until $\Delta G(n)$ (where n is the EDOT number of unity which made up the olygomer) maintains a negative value, estimating the critical n_c value at which $\Delta G(n)$ is nearest to zero can give an indication about the maximum chain length.

Studying $\Delta G(n)$ for different combinations of proton scavengers allows also to establish if more scavengers combination are possible (i.e. more than one choice makes polymerisation energetically favorable), to show how the chain length could be affected by the reactants choice.

3.3 Computational implementation

Standard Gibbs Free energy of a reaction in solution ΔG^*_{sol} can be written as a sum of three contributions, according to

$$\Delta G^*_{\text{sol}} = \Delta G_0 + \Delta G^{0\to *} + \Delta G_{\text{sol}} \tag{3.1}$$

where ΔG_0 is the Gas-phase Free Gibbs energy of reaction, $\Delta G^{0\to *}$ is the thermodynamic correction taking into account the transition from gas-phase state to standard condition (1M concentration) and finally ΔG_{sol} is the solvation Gibbs Free energy arising from solute-solvent interactions for each reactant and product.

Electronic structure calculations can be successfully exploited to evaluate the first and the last terms of the right member of equation Eq. 3.1 by using the Gaussian 16 simulation package.[9]

Starting from the first term of summation in Eq. 3.1, as explained in detail in Ochterski's technical report,[22] the evaluation of Gibbs free energy in vacuo (i.e. assuming the simulated molecule in a gas phase at Standard Pressure and Temperature conditions, STP[1]) is based on the applications of incremental corrections to the pure ab-initio zero-point energy E_0 each one naturally arising from the two main thermodynamic identities for internal

[1] T=298,15 K, p=1 atm

thermal energy E and molar entropy s_{mol} as obtained by manipulation of the standard form stated by McQuarrie's textbook.[20] The evaluation of the global $q(V,T)$ partition function of the simulated molecule

$$\begin{aligned} s_{\mathrm{mol}} &= \frac{S}{n} = R\left(1 + \ln\left(q(V,T)\right) + T\left(\frac{\partial \ln q}{\partial T}\right)_V\right) \\ E &= N k_{\mathrm{B}} T^2 \left(\frac{\partial \ln q}{\partial T}\right)_V \end{aligned} \tag{3.2}$$

where R and k_{B} are the gas and Boltzmann constant, respectively and N the number of particles at temperature T in the volume V.

By partitioning $q(V,T)$ in its translation q_t, rotational q_r, vibrational q_v and electronic q_e contributions as

$$q(V,T) = q_t q_r q_v q_e \tag{3.3}$$

the general forms for each contribution to s and E can be eventually obtained.

Referring to the cited work for all the calculations technicalities,[22] after summation of all the contributions arising from translational, rotational, vibrational motions and from electronic contribution, the overall thermal energy E_{tot} and molar entropy S_{tot} are combined to obtain the corrections $H_{\mathrm{corr}}, S_{\mathrm{corr}}$ to be applied to the zero point energy E_0 in order to obtain the enthalpy H and Gibbs free energy G_0 for the simulated molecule. Formally

$$\begin{aligned} G_0 &= E_0 + G_{\mathrm{corr}} \\ &= E_0 + (H_{\mathrm{corr}} - T S_{\mathrm{tot}}) \end{aligned} \tag{3.4}$$

where H_{corr}, the correction for enthalpy, is given by $E_0 + k_{\mathrm{B}} T$.

For the general reaction scheme

$$\mathrm{A} + \mathrm{B} \rightleftharpoons \mathrm{C} + \mathrm{D} \tag{3.5}$$

the Gibbs free energy variation ΔG_0 is evaluated as a difference between the sum of Gibbs Free energies of each product and the sum of those of each reactant, namely

$$\begin{aligned} \Delta G_0 &= \sum_{\text{products}} G_0 - \sum_{\text{reactants}} G_0 \\ &= G_0(\mathrm{C}) + G_0(\mathrm{D}) - G_0(\mathrm{A}) - G_0(\mathrm{B}) \end{aligned} \tag{3.6}$$

It is noteworthy that in the process of calculation of the gas-phase Gibbs free energy an important role is played by the analysis of vibrational frequencies required to estimates the vibrational contribution.

One very important condition to obtain accurate results is that the molecular structure under examination must be in its ground state in order to exclude the presence of imaginary frequencies, automatically excluded from the analysis by Gaussian 16 internal routine.[9,22]

To this aim, in all the structures analyzed, in the present work is assumed that before every G_0 calculation a preliminary geometrical optimization has been performed at the same level of theory (i.e. same functional and basis set) used for subsequent vibrational analysis and, by direct inspection, it has been excluded the existence of imaginary frequencies associated with the final, relaxed structure.

The evaluation of the third term in summation in Eq. 3.1, the solvation energy ΔG_{sol}, follows a slightly different protocol.

It is assumed as starting point for each calculation on reactants and products their specific full relaxed in vacuo molecular structure. G_{sol} for the specified molecule is then evaluated as the difference between the single point energy calculated in vacuo E_{ns} and the corresponding energy, at fixed geometry, including the presence of the self-consistent reaction field induced by the implicit solvent E_{s}

$$G_{\mathrm{sol}} = E_{\mathrm{s}} - E_{\mathrm{ns}} \tag{3.7}$$

where in E_{s} both electrostatic and non-electrostatic contributions are included via SMD implicit solvent model[18] in the context of the Integral Equation Formalism implemented in Polarizable Continuum Model (IEF-PCM).[4,21]

Starting from G_{sol}, the reaction ΔG_{sol} is then evaluated as in Eq. 3.6.

Finally, the thermodynamic correction $\Delta G^{0\to *}$ is summed as reported in Eq. 3.1. The origin of this term resides in the fact that all gas-phase standard state values (assumed in G_0 calculation) describe each molecule entering in the reaction as an ideal gas at standard conditions (P=1 bar and T=298.15 K), which does not correspond to the actual conditions experienced by the molecule in solution.

Thus, a correction to convert to a standard state of $\frac{1}{V^*} = 1$ mol L^{-1} concentration at $p = 1$ atm is calculated and added[15,26] according to

$$\Delta G^{0\to *} = \Delta \mathrm{n}\ RT\ \ln\left(\frac{\tilde{R}T}{pV^*}\right) \tag{3.8}$$

where Δn is the difference between the sum of moles of products and the sum of moles of reactants, R and $\tilde{R}$ are the universal gas constant (the product of Boltzmann and Avogadro constant $R = k_{\mathrm{B}}N_{\mathrm{A}}$) must be expressed[15] in J mol^{-1} K^{-1} and L atm mol^{-1} K^{-1}, respectively.

Table 3.1: Dissociation enthalpies ΔH_{298} (in kcal mol^{-1}) and entropies S (in cal mol^{-1} K^{-1}) for the six acids. The second and third columns report data available in Gutowski's work[12]) while the last four columns represent the results of the performed calculation at B3LYP/6-311G(d,p) and B3LYP/aug-cc-pvdz level.

Acid	Ref.[12]	experiment	B3LYP/6-311G(d,p)		B3LYP/aug-cc-pvdz	
	S	ΔH_{298}	S	ΔH_{298}	S	ΔH_{298}
HBr	47	323.5[3]	47.425	324.91	47.419	321.0
HCl	45	333.4[19]	44.605	329.53	44.595	330.1
HI	49	314.3[13]	49.444	316.68	49.444	316.7
H-HSO_4	74	312.5[2]	72.725	313.86	72.659	310.4
TfOH	89	305.4[16]	88.23	303.75	88.792	300.5
TsOH	104	n.a.	99.474	320.08	99.474	320.1

3.3.1 Assessment of validity

Before starting calculations on PEDOT's chains, preliminary tests were performed to check accuracies in evaluating of energies calculated by Gaussian09[17] and Gaussian16[9] suite of programs and to determine the best combination of functional and basis set to be used to obtain computational values closer to experimental available data.

As first test, the enthalpic ΔH_{298} and entropic S contributions for dissociation of the strong acids listed in Table 3.1 were calculated using Gaussian 16[9] and compared with the results reported in Gutowski's work,[12] where both DFT-simulated and experimental[2, 3, 13, 16, 19] values are available.

In order to calculate the enthalpy at 298K, ΔH_{298}, and the entropy S associated to the dissociation reaction of each HA strong acids in its conjugated bases A^- and a free proton H^+

$$HA \rightleftharpoons A^- + H^+ \tag{3.9}$$

each molecular species entering in Eq. 3.9 was first optimized using B3LYP functional.

To check the influence of the basis sets, two separate calculations were performed using 6-311g(d,p) and aug-cc-pvdz with the same B3LYP functional.

After optimization, the vibrational frequency calculations to obtain the thermochemistry data were carried on at the same level of theory, obtaining the results reported in the last four columns of Table 3.1, which were successively compared with the computational estimates for S in Gutowski's article and the experimental results for ΔH_{298} there used.

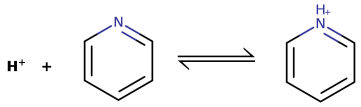

Figure 3.1: Schematic representation of the protonation of pyridine to pyridonium. Experimental Gibbs free energy in water solution $\Delta G^{\text{exp}} = -7.04$ kcal mol^{-1}.[25] $\Delta G^{\text{calc}} = -8.80$ kcal mol^{-1} with the adopted computational setup.

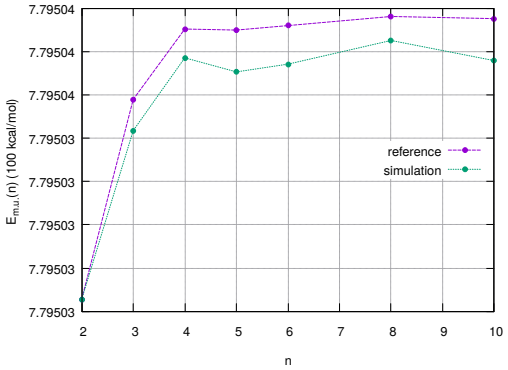

Figure 3.2: Energy Per Monomeric unit as a function of the overall number n of EDOT monomers in PEDOT olygomers with increasing chain length. Obtained data trend (green lines) is in fair agreement with data reported in Ref.[7] (purple line).

Both the adopted combinations tested are able to produce ΔH_{298} values in good agreement with available experimental data as well as S values in very good agreement with those reported in literature. In particular, it can be verified that mean square deviation on the analyzed sample of S amount to 2.1 cal mol^{-1} K^{-1} for both the combinations while deviations for ΔH_{298} are significantly lower (2.6 kcal mol^{-1}) if 6-311G(d,p) is used compared to aug-cc-pvdz case (3.6 kcal mol^{-1}).

For this reason, as well as the observed lower computational workload associated with the use of 6-311G(d,p) basis sets, all the subsequent calculations (including production data for PEDOT) were performed at B3LYP/6-311G(d,p) level of theory.

A second set of trial calculations was performed using B3LYP/6-311g(d,p) on PEDOT chains with chain length up to 10 monomeric units, to obtain the energy per monomer (EPM) as a function of EDOT number units n contained in each chain and comparing the resulting trend with data reported in Dkhissi's work[7] obtaining a fair agreement As third and final set

of trial calculations to check the accuracy of SMD implicit solvent model, the Gibbs free energy for the process of protonation of pyridine to pyridonium in water, as depicted in Fig. 3.1 and compared to the experimental value $\Delta G^{\text{exp}} = -7.04$ kcal mol^{-1} from Sacconi's work[25]

After performing the geometrical optimization and frequency calculations on both the molecular species in Eq. 3.1 (i.e. pyridine and pyridonium) at B3LYP/6-311g(d,p) level, Gibbs Free energy of the process, including solvation in water contribution, is estimated in $\Delta G^{\text{calc}} = -8.80$ kcal mol^{-1}, in fair agreement with experimental data.

3.4 Thermochemistry data for PEDOT

3.4.1 Computational protocol

In order to take into account the influence of proton scavenger used in PEDOT polymerization on the final micromorphology properties, the Gibbs free energy of reaction for all the six combinations of the three proposed scavengers (Pyridine Pyr, Tosylate TosOH, and water) was evaluated using Gaussian 09[17] and Gaussian 16[9] suites of software

$$
\begin{aligned}
&\mathrm{HX}_{n-1}\mathrm{H}^+ + \mathrm{HXH}^+ + 2\mathrm{Pyr} \rightleftharpoons \mathrm{HX}_n\mathrm{H} + 2\mathrm{PyrH}^+ \\
&\mathrm{HX}_{n-1}\mathrm{H}^+ + \mathrm{HXH}^+ + 2\mathrm{TosO}^- \rightleftharpoons \mathrm{HX}_n\mathrm{H} + 2\mathrm{TosOH} \\
&\mathrm{HX}_{n-1}\mathrm{H}^+ + \mathrm{HXH}^+ + 2\mathrm{H_2O} \rightleftharpoons \mathrm{HX}_n\mathrm{H} + 2\mathrm{H_3O}^+ \\
&\mathrm{HX}_{n-1}\mathrm{H}^+ + \mathrm{HXH}^+ + \mathrm{Pyr} + \mathrm{TosO}^- \rightleftharpoons \mathrm{HX}_n\mathrm{H} + \mathrm{PyrH}^+ + \mathrm{TosOH} \\
&\mathrm{HX}_{n-1}\mathrm{H}^+ + \mathrm{HXH}^+ + \mathrm{Pyr} + \mathrm{H_2O} \rightleftharpoons \mathrm{HX}_n\mathrm{H} + \mathrm{PyrH}^+ + \mathrm{H_3O}^+ \\
&\mathrm{HX}_{n-1}\mathrm{H}^+ + \mathrm{HXH}^+ + \mathrm{H_2O} + \mathrm{TosO}^- \rightleftharpoons \mathrm{HX}_n\mathrm{H} + \mathrm{H_3O}^+ + \ \mathrm{TosOH}
\end{aligned}
\tag{3.10}
$$

where $\mathrm{HX_nH}$, with $\mathrm{n} \geq 2$, is the PEDOT olygomer made up by n monomeric units.

Each one of the molecular structures entering on Eq. 3.10 was generated and preliminary optimized in Avogadro[14] molecular editor via the built-in facility, using Universal Force Field UFF.[24]

Each resulting pre-optimized structure was further relaxed at DFT/B3LYP/6-311G(d,p) level in order to obtain, after performing vibrational frequencies analysis, the G_0 gas-phase Gibbs free energy associated to the specified molecule. At this stage, the absence of imaginary frequency was verified by direct inspection of Gaussian output in order to assure the correct relaxation of the structure in a true local minimum of energy.

Gibbs free energy of reaction in vacuo for each proposed polymerization scheme was then evaluated according to Eq. 3.6.

Calculation of the solvation Gibbs free energy G_{sol} for each chemical species was performed using as starting point the atomic coordinates relaxed, as resulting from gas-phase calculations, and repeating the same steps for G_0 calculations, i.e. optimization and frequency analysis but now including the effects of solvent environment (assumed to be ethanol) using SMD implicit solvent model.

The solvation Gibbs Free energy associated to each molecule, G_{sol}, is then evaluated as the energy difference between the single point energies estimated in vacuo and in solution.

The free energy data set $\Delta G(n)^*_{\mathrm{sol}}$ for each scavengers combination, with $2 \leq \mathrm{n} \leq 16$, is finally calculated according to Eq. 3.1.

3.4.2 Results

The calculated ΔG_0 and $\Delta G(\mathrm{n})^*_{\mathrm{sol}}$ trend for increasing chain lengths n are depicted in Fig. 3.3a and Fig. 3.3b, respectively.

One of the first features which can be clearly observed in Fig. 3.3 is the large difference existing between the values estimated in vacuo and in solution, proving the impact of the ΔG_{sol} contribution in determining the final results.

The observed differences results in a shift of the values estimated in vacuo with respect to the ones estimated in solution, the amount of which is clearly strictly related to the specified combination of scavenger.

Since the polymerization reaction can spontaneously occur only when $\Delta G^*_{\mathrm{sol}}$ is negative, the position of 0 value is included as reference.

It can be observed that water alone (i.e. the combination of two water molecules as scavenger) results a poor reactant choice both in vacuo as well as in solvent ethanol. In the first case, no spontaneous polymerization is allowed, in the second case only dimerization can eventually take place in ethanol.

The presence of two pyridine molecules or one pyridine and one tosylate molecules, by contrast, is associated with an energetic trend suggesting that the accretion of chains is not energetically forbidden even for high molecular weights. It can be thus hypothesized that a further polymerization could be in these cases prevented by the local exhaustion of reactants, an hypothesis which will be tested by accurate polymerization dynamics simulation in the following part of this chapter.

All the others combinations appear, instead, to lead to spontaneous polymerization only for very limited chain lengths, with tosylate+water combination stopping at 6 monomeric units and pyridine+water or two tosylate at ~ 10 m.u.

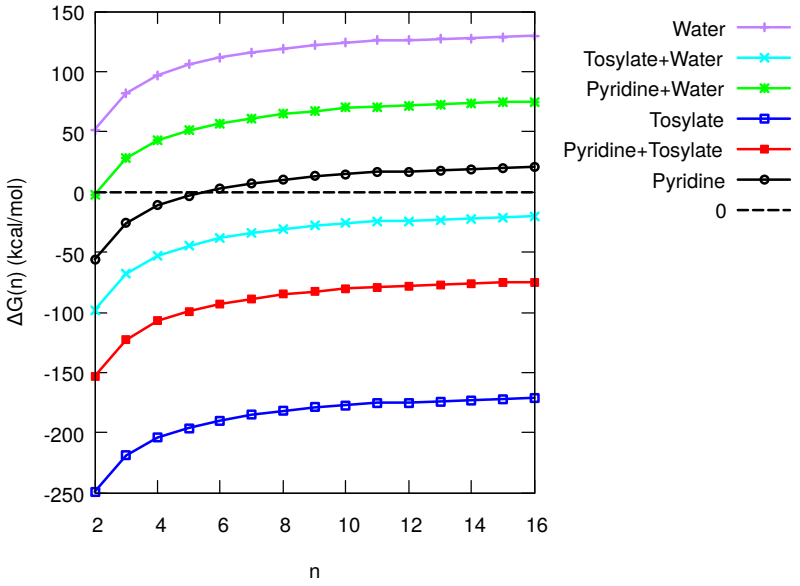

(a) in vacuum

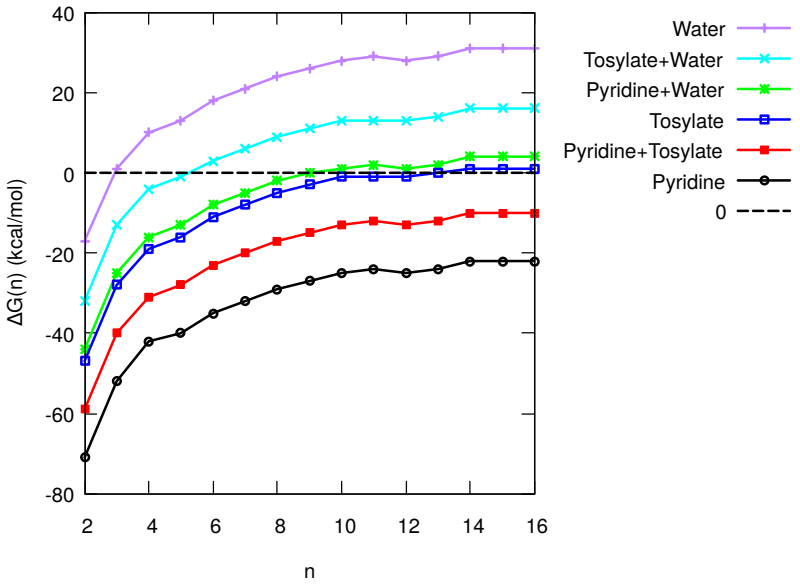

(b) in ethanol

Figure 3.3: Gibbs free energies calculated in (a) vacuum and (b) in ethanol (SMD implicit solvent model). 0 value (dashed black line) is included as reference level.

The observed trend of ΔG^*_{sol} is qualitatevely confirmed by the two work in literature. Firstly, it is experimentally established[6,28] that bases such as imidazole and pyridine act as inhibitors of the polymerization reaction, by raising the pH of the reaction environment and preventing activation of unwanted reaction channels.[29] Among all the combinations, tosylate seems to give rise to chain lengths that are in the order of 9 monomer units, consistent with the general notion according to which the chains of PEDOT have a limited length (between 5-15 monomers[10])

3.4.3 Interpretation of observations based on Gibbs free energies

To interpret the observations of the work of Fabretto et al.,[8] the trend of Gibbs free energies in vacuo (Fig.3.3a) could be possibly used as reference. The experimental conditions described[8] can in fact lead to the most probable conclusion that no solvent is present in the region in which the polymerization takes place in the vacuum chamber used. In fact, both water and butanol are eliminated from the substrate and from the experimental chamber, with the only exception constituted by the case in which the condensation of the steam is observed. This circumstance, which can be computationally simulated as polymerization in water solvent, is not meaningful since the formation of a liquid layer has been experimentally related to the formation of an inhomogeneous and poorly conductive film.[8]

It should be noted that the enthalpy contribution and the ΔG_0 shown in Fig.3.3a are calculated in STP conditions, while in the experiments[8] both the temperature and the pressure are notably different form STP values, being the pressure in the range $5 < p < 35$ mbar.

In order to take into account the difference in pressure and temperature between the adopted computational setup and the specific experimental conditions present in Fabretto's work[8] ($p = 0.01$ atm and $T = 50\ C$) were estimated in the specific case of dimerization, $n = 2$. The values appear, for all the combinations, systematically increased of $\sim 5\frac{\text{kcal}}{\text{mol}}$, a difference sufficiently small to assume that the trend shown in Fig. 3.3a is still valid under the experimental conditions described.

From thermodynamics considerations, it is observed that water cannot spontaneously act directly as proton scavenger, a conclusion not in contrast with experimental observation[8] since polymerization appears to occur in the presence of water vapor but above the tosylated iron (III) layer.

At the light of the new data provided in Fig.3.3, the tosylate, in the presence of steam, appears to function not only as oxidizant for the PEDOT molecules involved but also as a proton scavenger. From the analysis of

$\Delta G(n)$ curves, moreover, tosylate appear to be far more efficient than water for the latter purpose.

It appears clear that the description strictly faithful to the observed phenomenon can be summarized as follows. In the absence of water and pyridine, the mixture of EDOT and tosylate is not subject to any macroscopically appreciable reaction. In the presence of water vapor or pyridine, polymerization takes place.

In this sense, two tosylate molecules have the energy balance more favorable to make possible polymerization.

Clearly, even an energetically favored reaction can have a sufficiently high activation energy to prevent it from taking place, as can be speculated from the experimental data,[8] where the energy barrier for the reaction in which two tosylate anions are proton scavengers must be significantly high.

Since it is thermodynamically clear that water alone cannot act as a proton scavenger, it could possibly modify the height of the energy barrier.

At this point we can assume, for example, that the water induces a geometric distortion of the reaction intermediate which thus achieves a more favourable geometry from the energy point of view in order to allow the extraction of the protons.

As can be seen in Fig. 3.3, for chain lengths equal to 10 EDOT units, the Gibbs free energy is largely negative: the data therefore suggest that polymerization gives rise to chains of length extremely high.

On the other hand, the film formation mechanism briefly described in experiment[8] allows us to hypothesize that the chain length is limited by the chain coalescence process, which could compete with the chain growth. The formation of a conglomerate of chains, in fact, could limit even from a geometric point of view, the possibility that the ends of the chains grow.

The formation of a green film in the presence of pyridine and the absence of water can be explained on the basis of the energy results. The green coloration is interpreted by Fabretto et al.,[8] on the basis of the spectrographic analysis as due to the presence of short chains. If pyridine, like water, managed to lower the energy barrier allowing the tosylate to act as proton scavenger, the chains would also be extremely long. The fact that the chains are short, as shown experimentally, indicates that pyridine cannot act as a catalyst for the reaction. The tosylate is therefore inert as potential proton scavenger.

The combination of two pyridines as proton scavenger explains the reduced chain length from an energy point of view: ΔG_0 reaches zero for $5 < n < 6$.

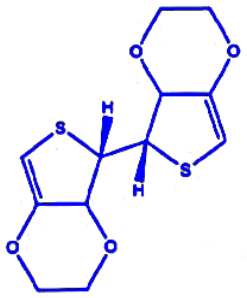

Figure 3.4: Reaction intermediate structure for the dimerization (n=2) case. It can be observed the presence of two out-of-plane protons, confering to the molecule a net $+2e$ charge.

3.4.4 Estimating the height of the barrier

To estimate the height of the barrier, referring to the polymerization mechanism known from the literature, the energy of the reaction intermediate for the case of dimerization has been calculated by means of Gaussian: the structure of the intermediate, with global charge $+2$, is schematized in Fig. 3.4 It turns out that the difference in energy ΔG_0 between the molecule shown in Fig. 3.4 and two EDOTs each with global charge $+1$ is equal to $220.778 \frac{\text{kcal}}{\text{mol}}$.

We observe that in the case of the dimerization in which the two tosylates act as proton scavengers, the global balance is $\Delta G(n=2) = -249.755 \frac{kcal}{mol}$, suggesting that as soon as the tosylate polymerization takes place, it releases enough energy to allow the remaining tosylate molecules to overcome the barrier.

The formation of more complex reaction intermediates, which involves temporary bonds with the proton scavengers considered, is not excluded as a hypothesis to explain the overcoming of the barrier in the case of 2 pyridines.

3.4.5 Combining reaction's scheme

Polymerisation of EDOT could occur in a solution containing a certain amount of water: since ΔG^*_{sol} for water-only proton scavengers scheme is always positive for all olygomers greater than dimer, this means that, provided all barriers are overcome for sufficient long times, catalysis reaction

$$\text{HX}_\text{n}\text{H} + 2\text{H}_3\text{O}^+ \rightleftharpoons \text{HX}_{n-1}\text{H}^+ + \text{HXH}^+ + 2\text{H}_2\text{O} \tag{3.11}$$

is energetically favorable. Provided a sufficient hydronia cations are available, long chain seem be unstable in solution.

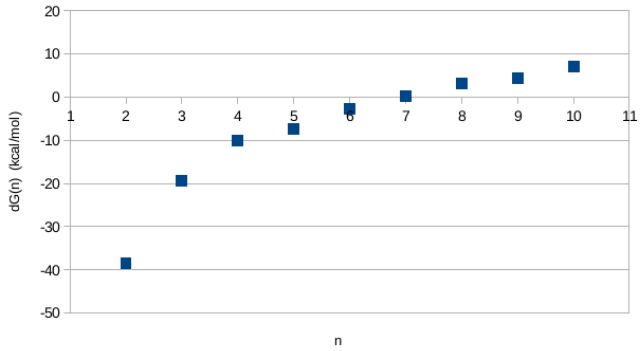

Figure 3.5: Gibbs Free energy for reaction Eq. 3.13 as a function of n and normalized for HX_nH units' number.

By the other hand, tosylate and pyridine are always present in solution and Gibbs Free energy analysis has shown that reaction

$$HX_{n-1}H^+ + HXH^+ + Pyr + TosO^- \rightleftharpoons HX_nH + PyrH^+ + TosOH \quad (3.12)$$

is characterised by a Gibbs Free energy negative for very large value of n. Hydronia acts thus as a polymerisation limiters.

Assuming, realistically, that hydronia, tosylate and pyridine are present in solution, we calculated the Gibbs Free energy of reaction

$$\begin{aligned} 2HX_{n-1}H^+ + 2HXH^+ + Pyr + TosO^- + 2H_2O \\ \rightleftharpoons 2HX_nH + PyrH^+ + TosOH + 2H_3O^+ \end{aligned} \quad (3.13)$$

and represented, as shown in Fig. 3.5 the Gibbs Free energy of reaction per HX_nH unit for this reaction. In this case we expect that PEDOT polymerisation proceeds until the energy increase for each HX_nH olygomer approaches to zero. The curve crosses the zero between $n = 6$ and $n = 7$ showing that polymerisation, provided that enough hydronia are presents, stops when a six m.u. olygomer is formed: this is in agreement with some literature works which report PEDOT chain's length to be between 5 and 15.

When the number of hydronia cations in solution are lowered, for example increasing basicity, an increment in chain is expected because the dominant reaction scheme goes back to be Eq. 3.12. In other terms, pH incrementation seems to have as side effect the suppression of catalysis reaction in Eq. 3.11

3.5 Simulating chains growth

3.5.1 Introduction

In this section, we will expose the procedure and results obtained in simulating the actual process of PEDOT chain growth using a novel computational protocol.

At the end of the previous section we presented the results of the Gibbs free energy of reaction of PEDOT synthesis, calculated at a DFT level, which represent the arrival point of the first step performed at the lowest affordable level of theory.

Gibbs free energies, by inclusion of the solvation contributions, calculated for each reaction stage resumes in a single scalar quantity all the quantum description of the system. In this chapter we provide the description and present the result of our computational algorithm properly nesting the information obtained at the previous stage in the more general framework of molecular dynamics (MD) simulation, which allows the analysis of large aggregates of atoms ($\sim 10^5$ in our simulations) otherwise not tractable in a full DFT approach.

3.5.2 The algorithm

The essence of the adopted polymerization algorithm is the use of a probabilistic, Markov based approach to simulate the process by which the olygomeric units (in the lower limit reducing to a single monomer), aggregates to form larger chains, with a probability p which is directly related to the microscopic detail of each reactant and embedded specifically in the Gibbs free energy.

Beside the specific characteristic, however, the mutual distance of the reactants also play a significant role in determining the possibility of a new bond to be created, which in this way can be seen as a function not only of the specific chemical species involved but also as function of the density and the time of polymerization (or, in an equivalent manner, to the degree of advance of the polymerization reaction itself).

Moreover, mutual distance is not the only factor influencing the reactivity and probability of aggregation, since the bond formation can be inhibited, even if distance is short enough, by the steric hindrance, due to the fact that not all the site of the molecule are active regions in which the bond itself can be created.

To recover both these dependence, which otherwise would be missed in the framework of pure probabilistic simulation, we simulate the dynamical behaviour of the aggregates of molecules in which the process of creation of

new bonds takes place, by means of the Molecular Dynamics.

As starting point, a collection of $N = 10^4$ EDOT monomers in a cubic simulation cell with $L = 11.8$ nm side is constructed. The number of monomers is chosen in order to reproduce in the volume of the cell fixed during the entire simulation, the average mass density ρ corresponding to the usually adopted concentration of EDOT in experiments.

The EDOT monomers are the only chemical species explicitly described in the simulation cell, no counterions (as PSS), no proton scavengers and no solvent molecules being present.

The absence of solvent and counterions is simply motivated by the fact that their contribution to the process of polymerization is already implicitly taken into account in the Gibbs free energy of reaction and thus the probability of creation of a new bond, while the absence of counterions as the PSS origins from the necessity not only to maintain a reasonable computational cost but also our interest in precisely isolate the effect exerted by the proton scavengers, more easily feasible if analysis is restricted to pristine EDOT samples.

The counterions choice, moreover, is not only something univocally determined but also problematic in simulations since several counterions have been experimented and reported in literature but very little study are present on their specific configurations and characteristics. In the case of PSS, to cite one of the most employed counterion, the presence of very extended chains and the broad chain distribution causes great problems in including it in the polymerization scheme designed for the EDOT and maintaining, at the same time, an affordable computational cost.

In any case, it should be underlined that we expect this counterions to play a role in polymerization mainly because of the steric and spatial impediments they pose to approaching of reactants, thus limiting the chain growth process, but which we choose, in a first approximation, to neglected.

A preliminary structural minimization followed by thermalization are performed. Pseudo-dynamic with conjugated gradient and a timestep as large as 1fs are used for minimization. Thermalization is achieved by using the Nosé-Hoover thermostat and barostat in the NPT ensemble imposing $T = 300$K and atmospheric pressure, with the dynamics simulated with a 0.5fs timestep until convergence to temperature and volume of equilibrium.

When the system is equilibrated, two stages are iteratively repeated, each one answering to the two interlinked aspect we are interested to simulate, (i) the probabilistic creation of a bond and (ii) the role of distance and topology, which we named *dynamical* and *coupling* step.

The *dynamical step* consists in a MD run in which the time evolution

of the atomic positions and velocities of the system is achieved by solving the Newton equations of motion using the velocity-Verlet algorithm, with interatomic forces described via bonding and non-bonding terms of the AMBER forcefield, with a 0.5fs timestep and temperature and pressure kept constant using the Nosé-Hoover thermostat and barostat. In order to avoid large pressure fluctuations, the relaxation time for the barostat was set to 0.5ps while for thermostat proved to be sufficient.

To provide an accurate description of electrostatic contributions, RESP (restrained electrostatic potential) atomic partial charges were calculated using Gaussian 16[9] and a particle-particle-particle mesh solver for long range electrostatic interactions and imposing a cut-off distance of 1.0nm for shorter range van der Waals interactions.

The dynamical step is followed by the *coupling step*, in which the bonds are actually created.

The intermolecular distance d of each couple of fragments which, according to the reaction scheme, can be possibly merge to form a larger olygomer is calculated. No bonds are formed if the distance between the molecules is larger than the imposed threshold of 3Å.

Conversely, if the molecules approach at a distance below the threshold, in order to take into account the statistical nature of a chemical bond creation, a probability proportional to the Boltzmann factor containing the ΔG_n free reaction energy

$$p \propto \exp\left(-\frac{\Delta G_n(\mathrm{B,B'})}{k_\mathrm{b}T}\right) \tag{3.14}$$

is calculated if the two molecules approaching are a monomer and an olygomer with $n-1$ monomeric units. Notice that the Gibbs free energy depends on the choice of the couple of proton scavenger B,B' adopted.

If the reaction is favourable ($\Delta G_n < 0$), the bond is always created by assuming $p = 1$ while in the case $\Delta G_n > 0$ we do not exclude a priori the possibility of formation of a new bond but choose to assign a probability as lower as the absolute value of the Gibbs free energy increases. Each time a bond is created, all the bond parameters (such as the angle and diehedral variables) are properly written in the LAMMPS[23] data file. Their values are successively relaxed and evolved in time in the subsequent dynamic step.

Polymerization is simulated for each proton scavenger combination by varying the associated ΔG_n(B,B') for a total of $3 \cdot 10^6$ dynamical steps, corresponding to $1.5 \cdot 10^2$ps. It's important to note, however, that this temporal extension has not relation with the experimental polymerization temporal

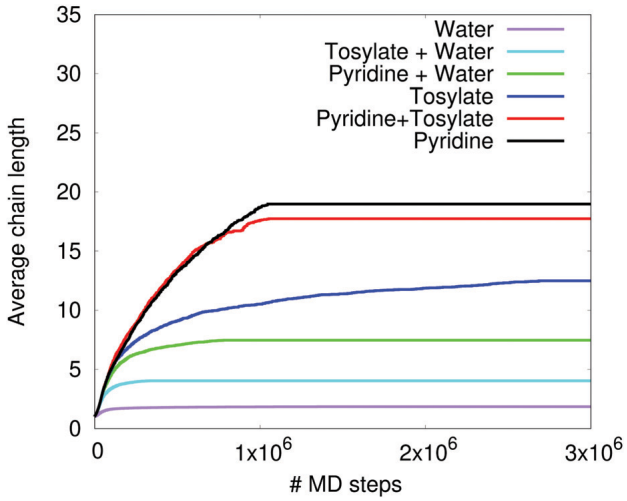

Figure 3.6: Average chain length during MD simulation for the different combination of scavengers employed.[5]

extension, since the Markov approach implemented in our algorithm to introduce new bond leads to a dynamics which is for certain verse accelerated if compared to the real microscopic dynamics.

3.5.3 Results

Average chain length

The evolution of average length of PEDOT chains formed during the Molecular Dynamics simulations for different combinations of proton scavengers are depicted in Fig. 3.6.

The results obtained are consistent with the analysis conducted on the Gibbs free energies of reactions. A very limited chain growth can be traced in water scavenged samples, with average chain length of $2-3$ monomeric units rapidly reaching its saturation values, while in pyridine scavenged samples the maximum average chain length ~ 20 monomeric units, is achieved after $\sim 10^6$ MD steps.

The chain growth process in samples scavenged using pyridine as one of the scavengers is limited by the initial concentration of the pyridine itself rather than energetics, which imposes a maximum number of bonds of $1.1 \cdot 10^4$ and is evidenced in Fig. 3.6 by the presence of clear plateau perfectly horizontal.

By contrast, in the case of pure tosylate based samples, the growth velocity, which can be defined as the first time derivative of the average chain

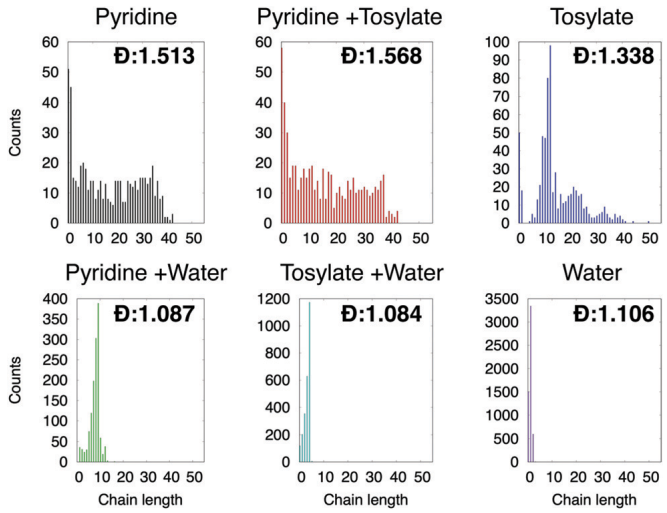

Figure 3.7: Chain length distribution at the end of MD simulations for the different combination of scavengers employed. The corresponding dispersity index is indicated for each distribution.[5]

length curve, gradually decreases as the polymerization process progresses but without reaching a plateau, a features which can be explained by the fact that the reaction, even if energetically favourable, is strongly limited by the increases distance between the reactants and the drastic diminution of unreacted monomers after the initial rapid growth.

In the case of tosylate based samples, in fact, the initial concentration of tosylate anions is sufficiently high to exclude its role in determining the final average chain length, with the concentration of monomers and the polymerization itself, limiting the monomers mobility, to play a crucial role in the observed drop of the reaction velocity.

Chain length multimodal distribution

A more detailed description of the impact of the proton scavengers choice on the polymerization can be obtained by the analysis of the chain length distribution and dispersity index D, defined as the ratio between the weight-average molecular mass M_w and the number-average molecular mass M_n

$$D = \frac{M_w}{M_n} = \frac{\sum_i n_i M_i^2}{\sum_i n_i M_i} \frac{\sum_i n_i}{\sum_i n_i M_i} \tag{3.15}$$

where n_i is the number of molecules with mass M_i. The index largely deviates from 1 in all the cases in which sizes of molecules or particles in the considered

ensemble is far from homogeneity and can be used to evidence the presence of multiple peaks in a distribution.

The chain length distributions and the corresponding dispersity index for each investigated combination of scavengers are reported in Fig. 3.7.

It can be observed that in the case of water and water+ tosylate cases, the samples are characterized by a conspicuous number of unreacted monomers and the distributions appear as a single and very narrow peak. This samples are thus composed by an aggregation of short chains, in contrast with the cases where pyridine and tosylate are present.

In particular, in the cases of pyridine and pyridine+tosylate scavenged samples, the chain length distribution extend to 40 monomeric units, indicating the presence of very long chains, a data which is consistent with the trend observed in Gibbs free energies of reaction, always sufficiently negative to make the polymerization process thermodynamically favourable. The distributions are very broad and no particular chain length in the range $1 - 40$ m.u. can be evidenced. Still, as in the water based samples, a significant fraction of unreacted monomers can be found, a data which support the idea that the convergence observed in the average chain length time evolution is dictated by the depletion of the scavenger. As possible experimental test for this hypothesis, it could be suggested to increase the amount of pyridine initially present in the starting solution in order to verify if, according to this explanation, longer chain length could be achieved.

The most interesting case, however, is represented by the pure tosylate scavenged samples, where the distribution is not only very broad but also displays the presence of three peaks corresponding to $\sim 12, 21, 35$ m.u.

This features, which is somewhat unexpected from the simple analysis of the free energy of reactions, reveals the existence of a multimodal distribution in the chain length for pristine PEDOT, a fact which, in our knowledge, as never be evidenced in literature.

Whitfield et al.,[27] however, evidenced in their review the fact that dispersity index can be properly tailored if the polymerization reaction requires an initiator. Since in our case of study the charged EDOT monomeric units can be interpreted as the initiator of the reaction, the observed multimodal distribution can be reasonable seen as a genuine effect induced by the tosylate rather than a mere artefact due to an unphysical condition of polymerization.

Moreover, according to Whitfield review,[27] the presence of a multimodal chain distribution can greatly impact on the transport properties of the polymer aggregate.

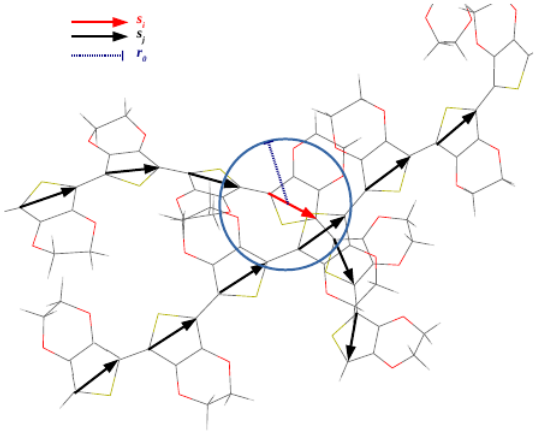

Figure 3.8: Schematic representation of definition of orientation vectors for the calculation of correlation parameter.[5]

Morphology and crystallinity

The influence of the proton scavenger combination used on the micromorphology of the simulated samples was evaluated by defining the crystallinity in terms of a pure geometrical parameter, the correlation of the orientation of each monomeric unit.

An orientational vector $\vec{s}_i$ was associated to each i-th thiophenic ring, with extremal points coinciding with the two carbon at the side of the sulphur atom (not belonging to the same chain) and the local spatial correlation $C(\vec{r})$ between the nearest neighbours has been evaluated as

$$C(\vec{r}) = \frac{1}{N} \sum_{|\vec{r}-\vec{r}_j|<r_0} |\vec{s}_i(\vec{r}) \cdot \vec{s}_j(\vec{r}_j)| \tag{3.16}$$

where the summation is extended on the monomers inside the sphere centered in $\vec{r}$ and radius $r_0 = 5$Å and divided for the total number of EDOT units N.

From the same definition of Eq. 3.16 it results that in regions characterized by a strong spatial correlation, $C(\vec{r})$ reaches it maximum while disorder configuration leads to values approaching zero, and the analysis of the quantity allows for a visual inspection of the regions with the higher degree of crystallinity (crystallites), where it is expected to found a long range ordering.

From definition Eq. 3.16, the fractional volume occupied by the crystal-

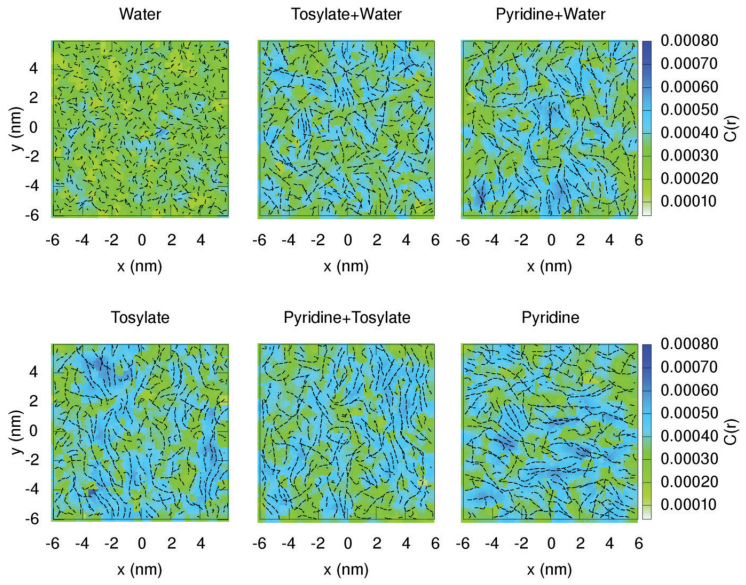

Figure 3.9: Correlation maps on a slab (1nm thickness) of each PEDOT sample analyzed, black segments representing the orientation of the monomeric EDOT units[5]

lites can be estimated by

$$v_{\mathrm{C}} = \frac{1}{V_{\mathrm{cell}}} \int \theta(C(\vec{r}) - C_{\mathrm{min}})\, dV \tag{3.17}$$

where the step function θ is used to restrict the volume integral on the region characterized by a $C(\vec{r})$ above the threshold $C_{\mathrm{min}} = 6 \cdot 10^{-4}$, chosen as half of the entire range of variation of the parameter in our samples, $(1-9)\cdot 10^{-4}$.

A section of the correlation maps produced for each sample is shown in Fig. 3.9, with $C(\vec{r})$ values displayed as a chromatic scale ranging from green (lowest ordered regions) to dark blue (high ordered regions).

The existence of crystallite domains is clearly visible in tosylate and pyridine based samples, while no relevant long range order seems to exist in pure water based sample. This data, if interpreted under the light of the chain length distributions, suggests the concurrent nature of polymerization and crystallization, since the presence of long PEDOT chains is strictly related with the emergence of larger crystallite domains.

This dependence is very evident if the fractional volume of crystallites is plot as a function of the average chain length, as in Fig. 3.10, where two behaviour distinctly emerges. At lower values of average chain length, a very

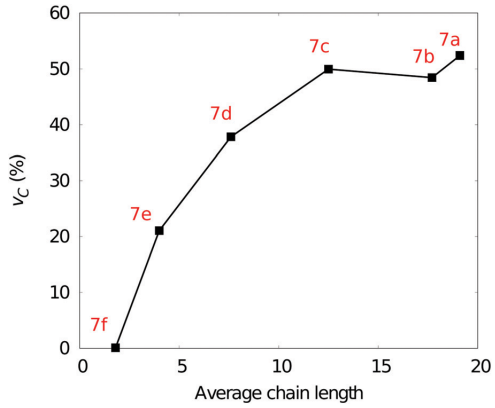

Figure 3.10: Fractional volume of crystallites v_C as function of the average chain length[5]

sharp increase of v_C can be traced, a growth which appears to arrive at a saturation value of $v_C^{max} \simeq 50\%$ in the right part of the interval.

XRD and time evolution

The dynamical evolution of micromorphology during the polymerization has been investigated by analysis of the radial distribution function restricted to the sulphur atoms $g_{S\text{-}S}(r)$ as depicted in Fig. 3.11 for the case of tosylate scavenged samples, shown as case of study.

Three main peaks have been clearly identified during the entire simulation run and the action of polymerization on their position consists in a shift toward lower values of r, indicating the formation of more compact structure inside the sample.

Moreover, a drastic reduction in the intensity of the first peaks is observed, which can be interpreted as an effect of the reduction of short chains and unreacted monomers.

As final validation of the simulation protocol, XRD spectra have been simulated using LAMMPS[23] and assuming incident wavelength $\lambda = 1.540$Å, following an approach reported in,[11] and compared with the experimental data from Aasmundtveit et al.[1] for tosylate scavenged PEDOT sample in presence of imidazole. The two curve are reported in Fig. 3.12.

The two peaks obtained from simulation ($2\theta = 11.7$ and $2\theta = 22.6$) are in good agreement with experiment ($2\theta = 12.1$ and $2\theta = 26.2$[1]), the main difference in the second peak attributed to $\pi - \pi$ stacking and possibly explained by the presence, in experimental conditions, of intermissing chemical species not explicitly simulated in our approach. A better agreement emerges

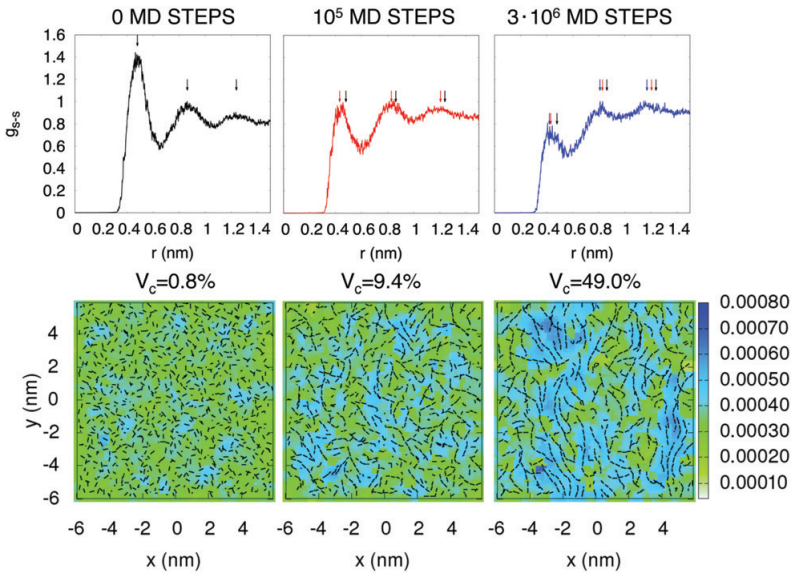

Figure 3.11: Time evolution of sulphur-sulphur radial distribution function, v_C and correlation map for tosylate based sample. The arrows in upper panel are introduced to evidence the variation in the position of the three main peaks during the polymerization process.[5]

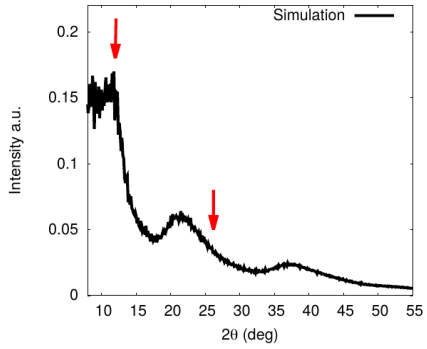

Figure 3.12: Simulated (black line) and experimental positions[1] (red arrows) of XRD peaks for tosylate scavenged PEDOT sample.

for the first peak which is attributed to lateral in-plane interaction between adjacent oligomers.

3.6 Conclusions

By including the effect of solvent in Gibbs free energy of reactions for several choice of proton scavengers, it emerged that the best combinations of proton scavengers to be employed in order to increase the chain length are pyridine and pyridine+tosylate.

By a novel computational tool which allows to include the information about the energetic of each choice of reactants in a modified Molecular Dynamics simulation, realistic micromorphologies of PEDOT samples were obtained, each one reflecting the characteristics dictated by the scavengers involved. In particular, it has been observed that combination containing tosylate and pyridine are characterized by broader chain length distributions, extending up to 40 monomeric units in pyridine cases, while water displayed the poorer performances in terms of volume occupied by crystallites and average chain length of resulting PEDOT sample.

By direct comparison of simulated XRD spectra with experimental positions of the main peaks associated to PEDOT sample polymerized using tosylate, it was found a good agreement with the position of the peak associated with the lateral in-plane interaction between monomeric units and small differences in the peak associated with $\pi - \pi$ stacking.

These differences, which can be safely attributed to force field parametrization and eventually the presence of intermissing molecules (not explicitly simulated in our code), do not impact on the assessment of validity of our polymerization algorithm, which suggest the formation of large crystalline regions in pyridine and tosylate scavenged samples.

The impact of the resulting different micromorphologies on the thermal transport properties and electric conductivity will be investigated in Chapter 4 and 5, respectively.

Bibliography

[1] KE Aasmundtveit, EJ Samuelsen, LAA Pettersson, O Inganäs, T Johansson, and R Feidenhans. Structure of thin films of poly (3, 4-ethylenedioxythiophene). *Synthetic Metals*, 101(1-3):561–564, 1999.

[2] Yuri Alexeev, Theresa L Windus, Chang-Guo Zhan, and David A Dixon. Accurate heats of formation and acidities for h3po4, h2so4, and h2co3 from ab initio electronic structure calculations. *International journal of quantum chemistry*, 102(5):775–784, 2005.

[3] C. Blondel, P. Cacciani, C. Delsart, and R. Trainham. High-resolution determination of the electron affinity of fluorine and bromine using crossed ion and laser beams. *Phys. Rev. A*, 40:3698–3701, Oct 1989.

[4] E Cances, Benedetta Mennucci, and J Tomasi. A new integral equation formalism for the polarizable continuum model: Theoretical background and applications to isotropic and anisotropic dielectrics. *The Journal of chemical physics*, 107(8):3032–3041, 1997.

[5] Antonio Cappai, Aleandro Antidormi, Andrea Bosin, Daniela Galliani, Dario Narducci, and Claudio Melis. Interplay between synthetic conditions and micromorphology in poly (3, 4-ethylenedioxythiophene): tosylate (pedot: Tos): an atomistic investigation. *Physical Chemistry Chemical Physics*, 21(16):8580–8586, 2019.

[6] D.M. de Leeuw, P.A. Kraakman, P.F.G. Bongaerts, C.M.J. Mutsaers, and D.B.M. Klaassen. Electroplating of conductive polymers for the metallization of insulators. *Synthetic Metals*, 66(3):263 – 273, 1994.

[7] A. Dkhissi, F. Louwet, L. Groenendaal, D. Beljonne, R. Lazzaroni, and J.L. Brédas. Theoretical investigation of the nature of the ground state in

the low-bandgap conjugated polymer, poly(3,4-ethylenedioxythiophene). *Chemical Physics Letters*, 359(5):466 – 472, 2002.

[8] Manrico Fabretto, Kamil Zuber, Colin Hall, and Peter Murphy. High conductivity pedot using humidity facilitated vacuum vapour phase polymerisation. *Macromolecular Rapid Communications*, 29(16):1403–1409, 2008.

[9] M. J. Frisch, G. W. Trucks, H. B. Schlegel, G. E. Scuseria, M. A. Robb, J. R. Cheeseman, G. Scalmani, V. Barone, G. A. Petersson, H. Nakatsuji, X. Li, M. Caricato, A. V. Marenich, J. Bloino, B. G. Janesko, R. Gomperts, B. Mennucci, H. P. Hratchian, J. V. Ortiz, A. F. Izmaylov, J. L. Sonnenberg, D. Williams-Young, F. Ding, F. Lipparini, F. Egidi, J. Goings, B. Peng, A. Petrone, T. Henderson, D. Ranasinghe, V. G. Zakrzewski, J. Gao, N. Rega, G. Zheng, W. Liang, M. Hada, M. Ehara, K. Toyota, R. Fukuda, J. Hasegawa, M. Ishida, T. Nakajima, Y. Honda, O. Kitao, H. Nakai, T. Vreven, K. Throssell, J. A. Montgomery, Jr., J. E. Peralta, F. Ogliaro, M. J. Bearpark, J. J. Heyd, E. N. Brothers, K. N. Kudin, V. N. Staroverov, T. A. Keith, R. Kobayashi, J. Normand, K. Raghavachari, A. P. Rendell, J. C. Burant, S. S. Iyengar, J. Tomasi, M. Cossi, J. M. Millam, M. Klene, C. Adamo, R. Cammi, J. W. Ochterski, R. L. Martin, K. Morokuma, O. Farkas, J. B. Foresman, and D. J. Fox. Gaussian 16 Revision C.01, 2016. Gaussian Inc. Wallingford CT.

[10] Daniela Galliani. *Poly(3,4-Ethylenedioxythiophene)(PEDOT) Based Materials For Thermoelectric Applications*. PhD thesis, Università degli Studi di Milano-Bicocca, 7 2017.

[11] Claudio Genovese, Aleandro Antidormi, Riccardo Dettori, Claudia Caddeo, Alessandro Mattoni, Luciano Colombo, and Claudio Melis. Linking morphology to thermal conductivity in pedot: an atomistic investigation. *Journal of Physics D: Applied Physics*, 50(49):494002, 2017.

[12] Keith E. Gutowski, John D. Holbrey, Robin D. Rogers, and David A. Dixon. Prediction of the formation and stabilities of energetic salts and ionic liquids based on ab initio electronic structure calculations. *The Journal of Physical Chemistry B*, 109(49):23196–23208, 2005. PMID: 16375283.

[13] D Hanstorp and M Gustafsson. Determination of the electron affinity of iodine. *Journal of Physics B: Atomic, Molecular and Optical Physics*, 25(8):1773, 1992.

[14] Marcus D Hanwell, Donald E Curtis, David C Lonie, Tim Vandermeersch, Eva Zurek, and Geoffrey R Hutchison. Avogadro: an advanced semantic chemical editor, visualization, and analysis platform. *Journal of cheminformatics*, 4(1):17, 2012.

[15] Junming Ho and Michelle L. Coote. First-principles prediction of acidities in the gas and solution phase. *WIREs Computational Molecular Science*, 1(5):649–660, 2011.

[16] Ilmar A Koppel, Robert W Taft, Frederick Anvia, Shi-Zheng Zhu, Li-Quing Hu, Kuang-Sen Sung, Darryl D DesMarteau, Lev M Yagupolskii, and Yurii L Yagupolskii. The gas-phase acidities of very strong neutral bronsted acids. *Journal of the American Chemical Society*, 116(7):3047–3057, 1994.

[17] H. B. Schlegel G. E. Scuseria M. A. Robb J. R. Cheeseman G. Scalmani V. Barone G. A. Petersson H. Nakatsuji X. Li M. Caricato A. Marenich J. Bloino B. G. Janesko R. Gomperts B. Mennucci H. P. Hratchian J. V. Ortiz A. F. Izmaylov J. L. Sonnenberg D. Williams-Young F. Ding F. Lipparini F. Egidi J. Goings B. Peng A. Petrone T. Henderson D. Ranasinghe V. G. Zakrzewski J. Gao N. Rega G. Zheng W. Liang M. Hada M. Ehara K. Toyota R. Fukuda J. Hasegawa M. Ishida T. Nakajima Y. Honda O. Kitao H. Nakai T. Vreven K. Throssell J. A. Montgomery Jr. J. E. Peralta F. Ogliaro M. Bearpark J. J. Heyd E. Brothers K. N. Kudin V. N. Staroverov T. Keith R. Kobayashi J. Normand K. Raghavachari A. Rendell J. C. Burant S. S. Iyengar J. Tomasi M. Cossi J. M. Millam M. Klene C. Adamo R. Cammi J. W. Ochterski R. L. Martin K. Morokuma O. Farkas J. B. Foresman M. J. Frisch, G. W. Trucks and D. J. Fox. Gaussian 09, revision a.02, 2016. Gaussian Inc. Wallingford CT.

[18] Aleksandr V Marenich, Christopher J Cramer, and Donald G Truhlar. Universal solvation model based on solute electron density and on a continuum model of the solvent defined by the bulk dielectric constant and atomic surface tensions. *The Journal of Physical Chemistry B*, 113(18):6378–6396, 2009.

[19] JDD Martin and JW Hepburn. Determination of bond dissociation energies by threshold ion-pair production spectroscopy: An improved d 0 (hcl). *The Journal of chemical physics*, 109(19):8139–8142, 1998.

[20] Donald A McQuarrie and John D Simon. *Molecular thermodynamics*. 1999.

[21] Benedetta Mennucci, E Cances, and J Tomasi. Evaluation of solvent effects in isotropic and anisotropic dielectrics and in ionic solutions with a unified integral equation method: theoretical bases, computational implementation, and numerical applications. *The Journal of Physical Chemistry B*, 101(49):10506–10517, 1997.

[22] Joseph W Ochterski. Thermochemistry in gaussian. *Gaussian Inc*, 1:1–19, 2000.

[23] Steve Plimpton. Fast parallel algorithms for short-range molecular dynamics. *Journal of Computational Physics*, 117(1):1 – 19, 1995.

[24] Anthony K Rappé, Carla J Casewit, KS Colwell, William A Goddard III, and W Mason Skiff. Uff, a full periodic table force field for molecular mechanics and molecular dynamics simulations. *Journal of the American chemical society*, 114(25):10024–10035, 1992.

[25] L Sacconi, P Paoletti, and M Ciampolini. Thermochemical studies. ii. thermodynamic quantities of neutralization of pyridine bases in water1. *Journal of the American Chemical Society*, 82(15):3831–3833, 1960.

[26] George C Shields and Paul G Seybold. *Computational approaches for the prediction of pKa values*. CRC Press, 2013.

[27] Richard Whitfield, Nghia P Truong, Daniel Messmer, Kostas Parkatzidis, Manon Rolland, and Athina Anastasaki. Tailoring polymer dispersity and shape of molecular weight distributions: methods and applications. *Chemical Science*, 10(38):8724–8734, 2019.

[28] Bjørn Winther-Jensen, Dag W. Breiby, and Keld West. Base inhibited oxidative polymerization of 3,4-ethylenedioxythiophene with iron(iii)tosylate. *Synthetic Metals*, 152(1):1 – 4, 2005. Proceedings of the International Conference on Science and Technology of Synthetic Metals.

[29] Bjørn Winther-Jensen and Keld West. Vapor-phase polymerization of 3,4 ethylenedioxythiophene: A route to highly conducting polymer surface layers. *Macromolecules*, 37(12):4538–4543, 2004.

Chapter 4

Thermal conductivity of PEDOT

4.1 Introduction

The study of heat propagation in organic polymers is of paramount importance for the realization of efficient thermoelectric devices, strategical in the ongoing search of large available and low-cost sources of energy.

Heat is in fact the final form in which all types of energies convert at the end of the process of production of electrical power, thermal energy is available in so a large amounts that any sufficiently efficient process of its conversion in electricity can potentially have an enormous impact in the world energy scenario, an impact largely influenced by the growing awareness of the risks linked to the use of fossil fuels as a driving force of the modern economy.

Large efforts have recently been done in order to increase the efficiency of existent thermoelectric generators (TEG), namely roughly described by the adimensional thermoelectric figure-of-merit

$$zT = \frac{\sigma S^2}{\kappa} T \tag{4.1}$$

in which S is the Seebeck coefficient, κ the overall thermal conductivity and σ the electrical conductivity, T representing the working temperature.

Organic conductive polymers seems to be the most suitable materials as constituents of active regions of TEG, since they can achieve by chemical doping relatively high electrical conductivity and Seebeck coefficients preserving an intrinsically low thermal conductivity.

Even if, at the state of the art, zT values are not sufficiently high in order to make possible a large scale use of organic based TEG, several works have been devoted to the scope of pushing forward the actual values of zT.

Refering to 4.1, the achievement of higher zT values in semiconductors junctions, in general, and in organic polymers, in particular, seems to be possible by significantly increasing the electrical conductivity while a sufficiently low thermal conductivity is maintained.

Among organic polymers, PEDOT seems to have emerged: it is in fact characterized by good electrical properties, such as an high hole mobility, air stability and a simple synthesis process which allow a large scale manufacturing.

As many other organic polymers, bulk PEDOT samples, usually synthesized with copolymer blends, also are generally regarded as thermal insulators because they display low thermal conductivities, in the range $0.20 - 0.38 \mathrm{Wm^{-1}K^{-1}}$ according to several experimental and computational values reported for PEDOT:Tos and PEDOT:PSS samples[1–4]) .

The presence of such low values of thermal conductivity is crucially determined by the overall micromorphology of the analysed samples and cannot be naively explained in terms of sum of the individual thermal conductivity of each PEDOT chain composing the aggregate. In fact, an individual polymer chain may have extremely high thermal conductivity, as Crnjar explained in his work,[5] where a systematic computational investigation is carried on PEDOT simplified geometries. According to this work, the interchains anharmonic interactions play a non negligible contribution in affecting the thermal transport in PEDOT and are directly responsible for the removal of an anomalous heat transport regime which appears to take place in single non-interacting chains. In this regime, the thermal conductivity κ appears to be related with the chain length L with the exponential law

$$\kappa \propto L^{(0.49 \pm 0.02)} \tag{4.2}$$

which is interpreted by authors as the scaling law evidencing the presence of the anomalous heat transport regime, a link suggested by literature[6]

This results have its roots in the first observations of Fermi, Pasta and Ulam[7] and have been confirmed by decades of discussion on anomalous heat conduction in one-dimensional lattices.[8] More recently, it was demonstrated by Zhang et al.[9] how temperature-induced morphology modifications can induce significant thermal conductivity variations in single chains and crystalline fibers of polyethylene, an effect confirmed in Polyamide 6[10] by analysis of Polydispersity Index. A possible explanation of this effect, pointing out

a clear dominance of thermal transport mediated by covalent bonds over nonbonded, inter-chain interactions (i.e. van der Waals), has been proposed by Luo et al.[11] invoking the increase of stiffness of polyethylene aggregates which manifest in the emergence of anisotropy in thermal transport.

Even if this observations mostly came up from simplified models, it is not far from true to assume as a commonly accepted fact that chain length plays a central role in determining transport properties of a material, referring to both thermal and electrical transport.

In the previous chapter it was extensively pointed out how the polymerization conditions, namely the proper choice of reactant (*proton scavengers*), greatly affect the micromorphology of the resultant pristine PEDOT samples: particularly efficient proton scavengers lead in fact to an increase both in maximum and average chain length. By means of Molecular Dynamics (MD) simulations it has been observed the impact of this chain distribution modifications on the degree of crystallinity, quantified using the fraction of volume occupied by crystalline regions surrounded by amorphous interfaces: as natural extension of that investigation, this Chapter explores the impact of the proton scavengers induced structure modifications on thermal transport properties. By means of standard molecular dynamics techniques the diagonal components of thermal conductivity tensor $\boldsymbol{\kappa}$ will be calculated and a modal analysis was performed in order to identify the impact of morphology on the vibrational modes involved.

4.2 Method

4.2.1 Thermal conduction from AEMD simulation

Estimations of thermal conductivity in materials can mainly exploit two different results from thermodynamics:

1. the relation between the autocorrelation of thermal j current and the κ thermal conductivity, a special case of Green–Kubo relations arising from the Fluctuation Theorem

$$\kappa_{ij} = \frac{1}{k_B T^2 V} \int_0^{+\infty} dt \ \langle j_i(t) j_j(0) \rangle \tag{4.3}$$

   where i, j denotes the direction along with the thermal current is analyzed during a NVE simulation performed on a sample thermalized homogeneously at a T temperature;

2. the phenomenological Fourier equation for nonequilibrium, diffusive heat transport linking the thermal current j arising from an existing

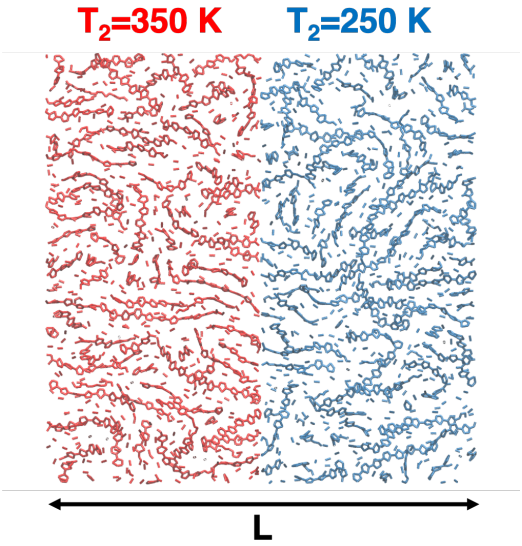

Figure 4.1: Scheme for AEMD simulation[12]

temperature gradient $\frac{\partial T}{\partial x}$

$$j_x = -\kappa \frac{\partial T}{\partial x} \tag{4.4}$$

While the first relation requires a well equilibrated system (and so it is usually referred to as EMD Equilibrium Molecular Dynamics), the estimation of κ using the Fourier law can be performed in both transient or steady Non Equilibrium Conditions.

The thermal conductivity will be estimated using transient non equilibrium conditions using the approach as described below.

4.2.2 Theory for transient analysis

A possible strategy, reported in literature,[13] for the evaluation of thermal conductivity with Molecular Dynamics technique is based on the analysis of the evolution of the temperature difference between two region of the sample, for which a theoretical solution can be easily found by solving the partial derivatives heat equation.

By assuming, as in the cases of interest for PEDOT thermal conductivity, cubic simulation cells with $2l$ side and cross section $\Sigma = 4l^2$, an orthonormal frame of reference is constructed with its origin at the centre of the cell and the three axes parallel to each side, as depicted in Fig. 4.1. Heat transport

is studied along the x axis for the subsequent derivation without loss of generality.

The temperature field $T(x, y, z, t)$ describing the temperature of each point of the sample at each time t is the solution of the general heat equation

$$\frac{\partial T}{\partial t} = \alpha^2 \nabla^2 T \tag{4.5}$$

where α^2 is the thermal diffusivity defined as combination of the thermal conductivity σ, the mass density ρ and the specific heat c

$$\alpha^2 = \frac{\sigma}{\rho c} \tag{4.6}$$

Density can be directly evaluated for each sample by using standard molecular dynamics softwares, as LAMMPS,[14] while the specific heat can be easily calculated from Dulong-Petit law for molar specific heat capacity provided that the investigated compound is well above its specific Debye's temperature. In the case of PEDOT, starting from the data reported in literature, suggesting a Debye temperature below 273K[15] or very close to 315K[16] in idealized crystalline structure, it was found that preliminary calculations using LAMMPS suite and AMBER force field[17] that this computational setup correspond to assuming this condition fulfilled in the range of temperature $250-350$K investigated, since no significant deviation from the Dulong-Petit value has been found.

Assuming the periodic boundary conditions

$$\begin{aligned} T(x = -l, t) &= T(x = l, t) \\ \left.\frac{dT}{dx}\right|_{x=-l} &= \left.\frac{dT}{dx}\right|_{x=l} \end{aligned} \tag{4.7}$$

the general solution for the heat equation, i.e. the temperature field $T(\boldsymbol{r}, t) = T(x, y, z, t)$ can be obtained by separation of the variables trough the ansatz

$$T(\boldsymbol{r}, t) = \phi(\boldsymbol{r})\psi(t) \tag{4.8}$$

and obtaining

$$\frac{1}{\psi}\frac{d\psi}{dt} = \frac{\alpha^2}{\phi}\ \nabla^2\phi \tag{4.9}$$

Introducing a scalar $\lambda > 0$ variable, the previous equation can be recasted in the form of a system of two equations

$$\begin{cases} \frac{1}{\psi}\frac{d\psi}{dt} = -\lambda \\ \frac{\alpha^2}{\phi}\ \nabla^2\phi = -\lambda \end{cases} \tag{4.10}$$

where the first differential equation has the solution

$$\psi(t) = a_2 e^{-\lambda t} \tag{4.11}$$

while the second differential equation can be solved by a further separation of the variables by factorization

$$\phi(\boldsymbol{r}) = X(x)Y(y)Z(z) \tag{4.12}$$

Now, since the heat propagation is studied along the x direction, provided that the system is sufficiently homogeneous, an hypothesis which can be tested *a posteriori*, it can be concluded, by exploiting axial symmetry, that the product $Y(y)Z(z)$ reduces to a simple multiplicative constant ϕ_0.

The $X(x)$ function can be obtained as solution of

$$\frac{d^2X(x)}{dx^2} + \frac{\lambda}{\alpha^2}X(x) = 0 \tag{4.13}$$

which has general solution

$$X(x) = c_1 \sin\left(\frac{\sqrt{\lambda}}{\alpha}x\right) + c_2 \cos\left(\frac{\sqrt{\lambda}}{\alpha}x\right) \tag{4.14}$$

and thus the temperature field assumes the form

$$T(\boldsymbol{r}, t) = e^{-\lambda t}\left(c_1 \sin\left(\frac{\sqrt{\lambda}}{\alpha}x\right) + c_2 \cos\left(\frac{\sqrt{\lambda}}{\alpha}x\right)\right) \tag{4.15}$$

where c_1 e c_2 are rewritten to absorb the constant values of a_2, ϕ_0.

It is straightforward to verify that by imposing the periodic boundary conditions, which restrict the value of λ to the discrete set

$$\lambda_m = \frac{\alpha^2\pi^2}{l^2}m^2 \tag{4.16}$$

the temperature field can be written as superposition of Fourier normal modes

$$T(\boldsymbol{r}, t) = \sum_{m=1}^{+\infty} e^{-\frac{\alpha^2\pi^2}{l^2}m^2 t}\left(c_1(m) \sin\left(\frac{m\pi}{l}x\right) + c_2(m) \cos\left(\frac{m\pi}{l}x\right)\right) \tag{4.17}$$

where $c_1(m)$ and $c_2(m)$ are coefficients fixed by the assigned initial profile $T(x, y, z, t = 0)$.

Imposing a step-like temperature difference between the left ($x < 0$) and right ($x > 0$) half of the simulation cell described by the equation

$$T(\boldsymbol{r}, t = 0) = \frac{T_1 - T_2}{2}\ \mathrm{sign}(x) + \frac{T_1 + T_2}{2} \tag{4.18}$$

by equating the 4.17 at $t = 0$

$$T(\boldsymbol{r}, 0) = \sum_{m=1}^{+\infty} \left(c_1(m)\ \sin\left(\frac{m\pi}{l}x\right) + c_2(m)\ \cos\left(\frac{m\pi}{l}x\right)\right) \tag{4.19}$$

with the Fourier series expansion of 4.18

$$T(\boldsymbol{r}, 0) = \left(\frac{T_1 - T_2}{2}\ \frac{4}{\pi} \sum_{m=0}^{\infty} \frac{1}{(2m+1)} \sin\left(\frac{(2m+1)\pi}{l}x\right)\right) + \frac{T_1 + T_2}{2} \tag{4.20}$$

the temperature field $T(\boldsymbol{r}, t)$ can be easily obtained

$$T(\boldsymbol{r}, t) = \frac{T_1 - T_2}{2} \sum_{m=0}^{+\infty} e^{-\frac{\alpha^2\pi^2}{l^2}(2m+1)^2 t} \left(\frac{4}{\pi} \frac{1}{(2m+1)} \sin\left(\frac{(2m+1)\pi}{l}x\right)\right) + \frac{T_1 + T_2}{2} \tag{4.21}$$

The evolution of the spatially averaged temperature difference ΔT between the two halves of the system results to be

$$\begin{aligned} \Delta T(t) &= \frac{1}{l} \int_0^l \left(T(x, t) - T(-x, t)\right) dx = \\ &= \frac{8(T_1 - T_2)}{\pi^2} \sum_{m=0}^{+\infty} \frac{1}{(2m+1)^2}\ e^{-\frac{\alpha^2\pi^2}{l^2}(2m+1)^2 t} \end{aligned} \tag{4.22}$$

It can be observed that in the asymptotic limit of $t \to +\infty$, the temperature as described in 4.21 approaches to the average $\frac{T_1+T_2}{2}$ for each x value, as expected for an homogeneous sample, while the spatially averaged temperature difference $\Delta T(t)$ in 4.22 approaches zero.

As final remark, it can be observed that all the temperature of each point is determined only by the time and the x coordinate. This is a consequence of the solution of the heat equation by separation of the variables which implies no dependence from y and z coordinate or, in other terms, in assuming the thermal conductivity tensor to be in the diagonal form.

To check the presence of non-negligible off-diagonal components, the temperature evolution along the axis perpendicular to the initially imposed temperature gradient can be monitored in order to evidence deviations from the expected isoplanes-profile.

No such deviations were detected in all the cases analyzed.

4.2.3 Computational implementation of transient analysis

All the simulations were performed on the samples produced by the polymerization algorithm. The heat transfer dynamics was studied using the LAMMPS[14] package: in all simulations the equations of motions have been integrated by the velocity-Verlet algorithm with a timestep of 0.5fs. Atomic bonds have been described using AMBER force field:[17] pairwise interactions were computed using the standard Lennard-Jones potential and adding a Coulombic interaction both within a cutoff radius of 10Å. Long-range interactions (i.e. exceeding cutoff radius) were computed using a particle-particle particle-mesh solver (pppm) with an accuracy of 10^{-4}kcal mol^{-1}Å^{-1}.

All heat transfer simulations were carried on cubic samples of 118Å per side in periodic boundary condition along each direction. Each sample contains 10^4 monomeric units.

In order to create the step-like temperature profile along the samples, two regions, one for each half of the sample, were defined and alternately equilibrated at the target temperature $T_1 = 350$K and $T_2 = 250$K using a Nosé-Hoover thermostat. During the thermostatation of each cube's half, the atoms in the other one were kept fixed in order to avoid any heat exchange during the thermostatting process. After the equilibration of both halves, the motion of all atoms in the cubic sample was simulated in NVE ensemble and the temperature of each half has been recorded during all the calculation.

The $\Delta T(t)$ data sets sampled were fitted using the series 4.22 with $\Delta T_0 = T_1 - T_2$ and α as fitting parameters. The series have been truncated at $m = 20$ since in preliminary test performed for each sample found that increasing the m value up to this limit leads to no increase in the accuracy of obtained κ values, as depicted in Fig.4.2 for one of the cases examined.

4.2.4 Modal analysis

Thermal conductivity as calculated from transient analysis does not directly offers a mean to deeply investigate the effect caused by different chain length distributions.

This is not a fault of the theory itself but instead a consequence of the macroscopical character of the Fourier law, which does not require a detailed knowledge of the mechanism by which, at a more fundamental level, the energy flows inside the investigated samples.

For these reasons, even if the analysis of thermal conductivity resulting from this approach can evidence differences between samples scavenged in a different fashion, an investigation aiming to elucidate the precise role of the chain length distribution must include a more fine description of the system,

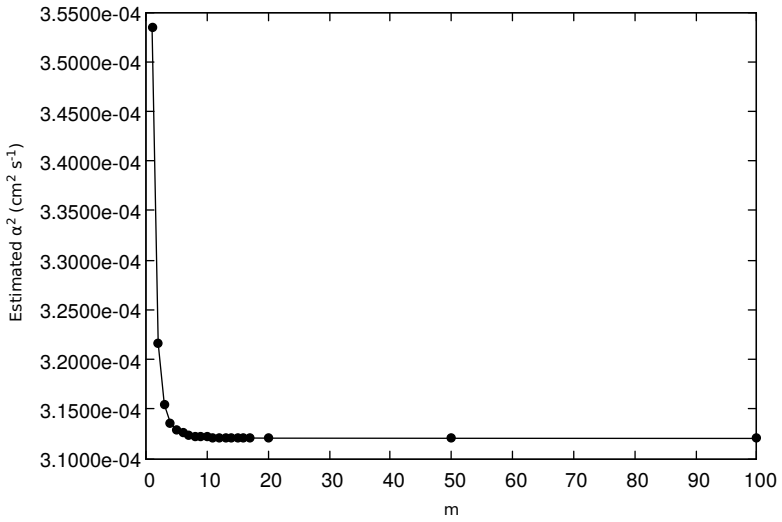

Figure 4.2: Thermal diffusivity α^2 derived from fitting of 4.22 on transient evolution obtained for one of the samples analyzed as function of the m cutoff imposed on the maximum term of the series. Convergence is achieved at $m = 20$ (relative difference below 0.01%)

at least at the atomic level.

The Green-Kubo Modal Analysis (GKMA)[18] can be seen as valuable tool to achieve this aim, being successfully employed in system in which translation invariance is partially or completely lacking, and the evaluation of a phononic group velocity or mean free paths is problematic or impossible, precluding the application of the standard techniques developed for pure crystalline systems.

GKMA applications ranges a large variety of non-crystalline systems, as amorphous carbon,[19] interfacial region[20] and nanoporous silicon, the latter being explored by Antidormi et al.,[21] whose strategy, hereafter summarized, inspired and have been applied in this work to reveal the impact of chain length distribution on PEDOT thermal conductivity by altering the dynamical state of motion of the atoms involved in the thermal energy transfer.

The central quantity of the GKMA is the dynamical matrix,[18,21] defined during a sufficiently long microcanonical simulation run in terms of the masses and the forces acting on the atoms

$$D_{l\alpha,j\beta} = -\frac{1}{\sqrt{m_l m_j}} \frac{\partial F_{l\alpha}}{\partial r_{j\beta}} \tag{4.23}$$

where m_l is the mass of the lth atom, $F_{l\alpha}$ the α Cartesian component of

the force acting on the lth atom and $r_{j\beta}$ the β Cartesian component of the displacement of the jth atom.

The diagonalization of the dynamical matrix 4.23 provides a basis set of $3N$ vectors (with N the total number of atoms) which are the eigenmodes $\mathbf{e}_{l,s}$ of the system. This frame of reference, which is strictly related with the real dynamical status of the system and it is thus not arbitrary as the xyz reference used for AEMD analysis, can be used to define a heat flux operator $\mathbf{Q}_s(t)$ at the atomic scale associated to each s eigenmode in the form

$$\mathbf{Q}_s(t) = \frac{1}{\Omega}\sum_{l=1}^{N}\left[E_l\dot{\mathbf{x}}_l(s,t) + \sum_{k=1}^{N}(\mathbf{F}_{lk}\dot{\mathbf{x}}_l(s,t)\mathbf{r}_{lk})\right] \tag{4.24}$$

where Ω is the total volume of the sample, E_l the total energy of the lth atom, $\mathbf{F}_{lk}$ is the force acting on the lth atom when the kth atom is displaced and $\mathbf{r}_{lk}$ the distance vector between the lth and kth atoms, while $\dot{\mathbf{x}}_l(s,t)$ represents the projections of the total velocity $\mathbf{v}_l$ of the lth atom onto the eigenvectors of the matrix given in eq.(4.23) according to

$$\dot{\mathbf{x}}_l(s,t) = (\mathbf{v}_l \cdot \mathbf{e}_{l,s})\mathbf{e}_{l,s} \tag{4.25}$$

The μ cartesian component of the total heat flux operator $q_\mu(t)$, entering in the Green-Kubo autocorrelation formula for each of the Cartesian component $\kappa_{\mu\nu}$ of the thermal conductivity tensor $\overleftrightarrow{\boldsymbol{\kappa}}$

$$\kappa_{\mu\nu} = \frac{\Omega}{k_B T^2}\int_0^\infty \langle q_\mu(t)\cdot q_\nu(0)\rangle\, dt \tag{4.26}$$

can be obtained by summing the corresponding $\mathrm{Q}_{\mu,s}(t)$ over the entire $3N$ set of eigenvectors, as

$$q_\mu(t) = \sum_{s=1}^{3N}\mathrm{Q}_{\mu,s}(t) \tag{4.27}$$

By substitution of 4.27 and 4.24 in 4.26, the average thermal conductivity, i.e.

$$\kappa = \frac{\kappa_{xx}+\kappa_{yy}+\kappa_{zz}}{3} \tag{4.28}$$

can be put in the form

$$\kappa = \frac{\Omega}{3k_B T^2}\int_0^\infty \left\langle \sum_{s=1}^{3N}\mathbf{Q}_s(t)\cdot\sum_{s'=1}^{3N}\mathbf{Q}_{s'}(0)\right\rangle dt \tag{4.29}$$

where the contribution the modes involved in heat transport is now clearly explicit.

The exact impact of every single sth mode on thermal conductivity can be quantified by defining the κ_s modal contribution as combination of the total heat flux operator 4.27 and rewriting 4.29 as

$$\kappa = \frac{\Omega}{3k_B T^2} \sum_{s=1}^{3N} \int_0^\infty \langle \mathbf{Q}_s(t) \cdot \mathbf{q}(0) \rangle \, dt = \sum_{s=1}^{3N} \kappa_s \tag{4.30}$$

The eigenvectors obtained by diagonalization of the dynamical matrix can be used to define another important quantity which describes the spatial extension of the modes involved in the process of heat transfer, the Participation Ratio (PR).[21]

For a system composed by N atoms, the PR is defined as

$$\mathrm{PR} = \frac{1}{N} \frac{\left(\sum_{l=1}^{N} \mathbf{e}_{l,s}^2 \right)^2}{\sum_{l=1}^{N} \mathbf{e}_{l,s}^4} \tag{4.31}$$

where $\mathbf{e}_{l,s}$ are derived from the diagonalization of the dynamical matrix.

The definition of PR makes possible to determine the spatial extension of each of the s modes involved in thermal transport. In fact, if the eigenmode analyzed involves a large group of atoms, i.e. if the spatial extension of the eigenmode is large, PR ~ 1, while in the case of localized modes the PR is very close to zero and decays as a function of the number of atoms N involved (PR $= O(N^{-1})$).[22] Starting from this different behavior, Allen et al.[22] proposed, by studying the paradigmatic case of amorphous silicon, a classification of extended modes in *diffusons*, for which the PR quickly decays to zero, and *propagons*, characterized by a larger and almost N-insensitive value of PR.

Finally, in order to better characterize the vibrational modes, it has been defined[21] the average coordination number, as the weighted number of bonds with first neighbors involved in a given mode. It is calculated as:

$$\bar{n}_s = \frac{\sum_{l=1}^{N} n_{C,l} \; e_{l,s}^2}{\sum_{l=1}^{N} e_{l,s}^2} \tag{4.32}$$

where $n_{C,l}$ is the coordination number of the lth atom, and $e_{l,s}^2$ is the squared modulus of its displacement vector.

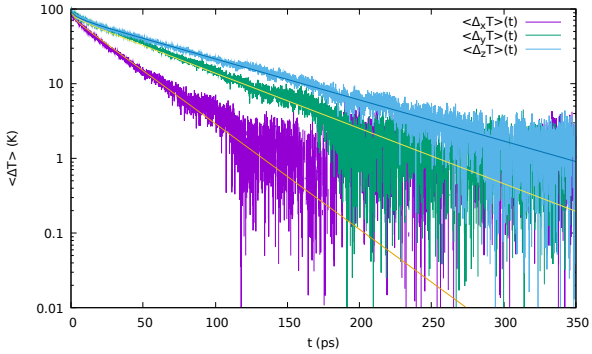

Figure 4.3: Evolution of average ΔT along the three directions of a **pyridine** sample: smooth lines represent the result of the fitting on simulated data. Semi-log scale is used.

4.3 Results

4.3.1 Dependence of thermal conductivity κ from adopted scavenger

The choice of the proton scavenger used in polymerization phase significantly impacts on the thermal conductivity of generated samples: as showed in Figures 4.3 – 4.8, in fact, scavenging affects not only the mean values of thermal conductivity $\bar{\kappa}$ but seems also to induce a significant amount of anisotropy in heat propagation.

This anisotropy induced effect appears to be maximal in pyridine scavenged samples, in which the drop of ΔT is very different according to the direction selected while is minimal in water scavenged sampels, where the time evolution of ΔT appears to be independent from the propagation direction analyzed.

Since the temperature difference ΔT profiles appears to be very noisy when values fall below $\sim 5K$, an ensemble average was performed for each sample, by varying the initial equilibration times and the resulting κ_x, κ_y, κ_z values were properly averaged: the results, shown in Fig. 4.9 and reported in Table 4.1, clearly confirm the existence of an anisotropy in heat propagation.

Since in the previous chapter was pointed out the influence of scavenging on final morphology of pristine PEDOT samples, in particular on average chain length and cristallyte fraction, and several works showed the impact of morphology on thermal transport properties, the connection existing between the proton scavenger used in polymerization and the resulting thermal conductivity can be explained as due by the modifications induced by the

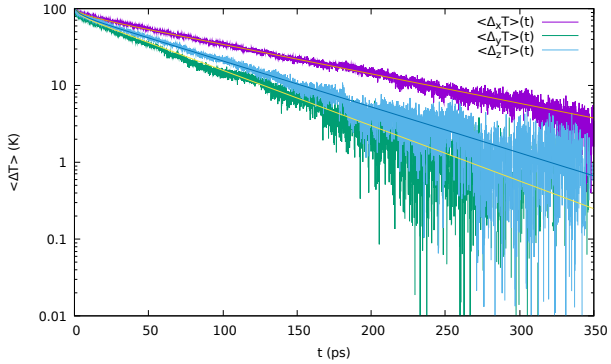

Figure 4.4: Evolution of average ΔT along the three directions of a **pyridine+water** sample: smooth lines represent the result of the fitting on simulated data. Semi-log scale is used.

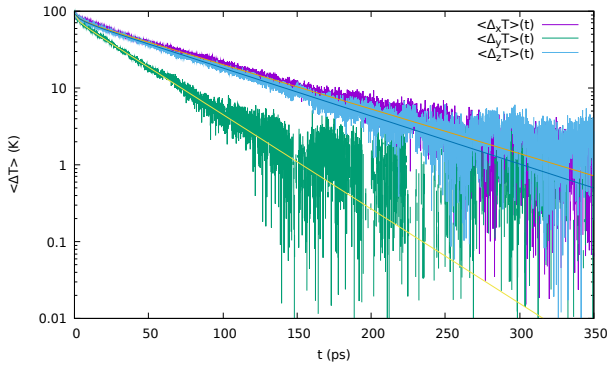

Figure 4.5: Evolution of average ΔT along the three directions of a **pyridine+tosylate** sample: smooth lines represent the result of the fitting on simulated data. Semi-log scale is used.

Table 4.1: Thermal conductivity $\kappa_{x,y,z}$ values for each sample reported in Fig. 4.9: all values are expressed in $\mathrm{WK^{-1}m^{-1}}$ unit

sample	κ_x	κ_y	κ_z
pyridine	0.36 ± 0.01	0.193 ± 0.005	0.145 ± 0.005
pyr+wat	0.103 ± 0.003	0.193 ± 0.003	0.155 ± 0.005
tosylate	0.128 ± 0.005	0.200 ± 0.008	0.305 ± 0.008
pyr+tos	0.156 ± 0.005	0.32 ± 0.01	0.17 ± 0.01
tos+wat	0.115 ± 0.0075	0.1225 ± 0.0075	0.093 ± 0.005
water	0.110 ± 0.003	0.1078 ± 0.0005	0.113 ± 0.003

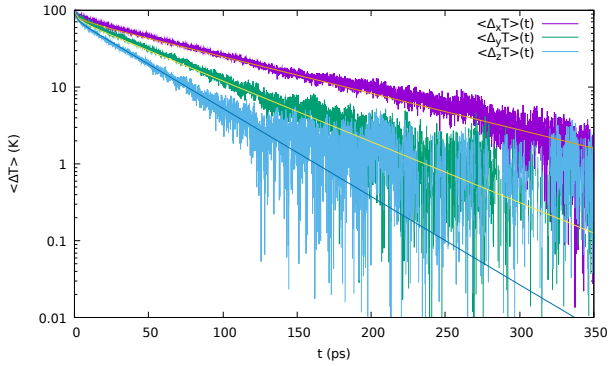

Figure 4.6: Evolution of average ΔT along the three directions of a **tosylate** sample: smooth lines represent the result of the fitting on simulated data. Semi-log scale is used.

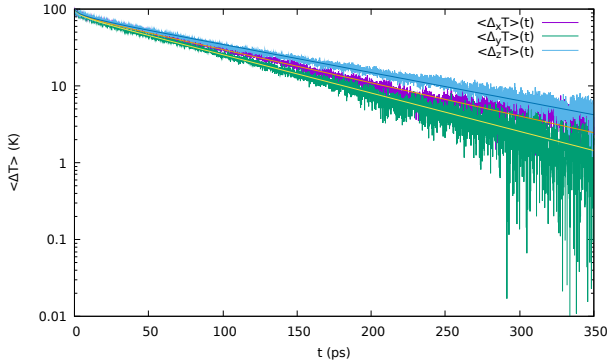

Figure 4.7: Evolution of average ΔT along the three directions of a **tosylate+water** sample: smooth lines represent the result of the fitting on simulated data. Semi-log scale is used.

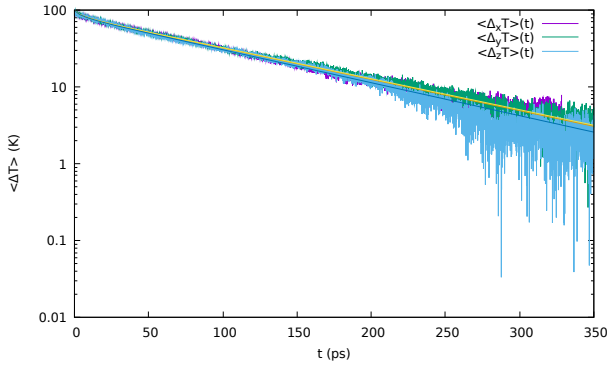

Figure 4.8: Evolution of average ΔT along the three directions of a **water** sample: smooth lines represent the result of the fitting on simulated data. Semi-log scale is used.

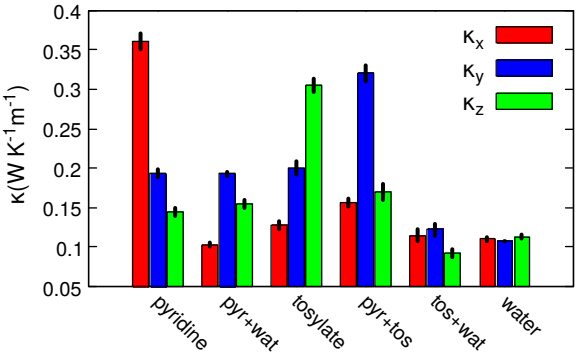

Figure 4.9: Thermal conductivity $\kappa_{x,y,z}$ values for each sample resulting from fitting an average ensemble of ΔT data collected in NVE simulation

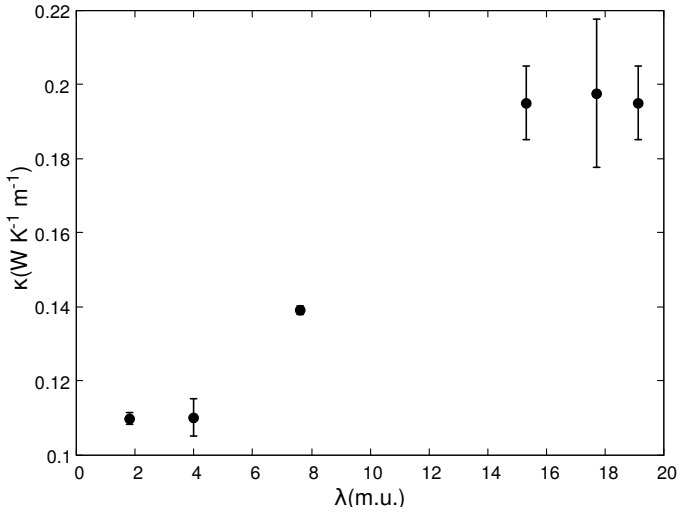

Figure 4.10: Average κ values of the samples analyzed plotted as a function of average chain length (expressed in monomeric units)

difference in scavenging on the final morphology of the samples. To better elucidate this dependence, in Fig. 4.10 the κ thermal conductivities are shown as a function of the average chain length characterizing the corresponding sample: the κ values depicted were obtained by averaging all values arising from each NVE simulation and averaging them regardless the direction of the heat flow, the error bar obtained as standard deviation of the population of spatial averages.

The analysis shows as the average κ thermal conductivity increases as the average chain length increase until a threshold value of ~ 15 monomeric units is achieved: then κ appears to stabilize around $\sim 0.2\mathrm{WK}^{-1}\mathrm{m}^{-1}$.

4.3.2 Longitudinal $\kappa_{\parallel}$ and transversal $\kappa_{\perp}$ thermal conductivities

The analysis reported has been extended in order to clarify two questions arising from the previous subsection: first, since during polymerization phase, the final chain orientation is unrelated to the axis orientation, it can easily question if previous thermal conductivity estimates are meaningful. The suggested dependence of κ from chain length can also be studied decomposing the thermal conductivities along the chain direction.

Referring to the first question, even if axis orientation is unrelated to the chain orientation, estimates of the three components of thermal conductivity κ are useful in order not only to elucidate the presence of an anisotropic

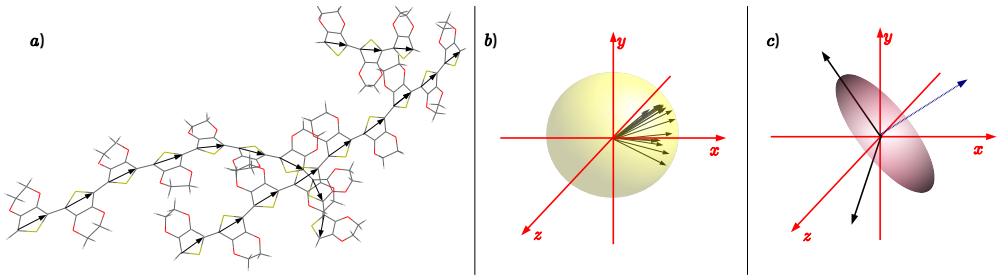

Figure 4.11: Graphical representation of the algorithm to find the direction of maximum alignment. In a) a normalized orientational vector is assigned to each monomeric unit and remapped as depicted in b) in order to generate a fictitious mass distribution lying on the surface of a sphere. Inertia tensor is calculated for this mass distribution in order to give the inertia elipsoid as in subfigure c).[12]

thermal transport but are also necessary to extract the mean κ value which permitted us to show the chain length dependence. Furthermore, even if samples show anisotropy, it can expected that in very large bulk samples the presence if different crystallite regions randomly orientated can mask the presence of anisotropy leading to a global spatially-averaged thermal conductivity, which still depends on average chain length but not on the direction of the imposed thermal gradient.

This is also the reason which lead to compute the spatially averaged $\bar{\kappa}$ on several samples polymerized with the same scavenger but different initial conditions in order to obtain a meaningful bulk value for thermal conductivity.

The adopted analysis protocol, as visually depicted in Fig.4.11 is reported below.

Starting from a polymerized sample using a specific proton scavenger it has been defined an orientation vector for each monomer present in the sample. The orientation vector is defined by the two carbon atoms of the thiophenic ring, and, as explained in the previous chapter, for the sake of this study the two carbon atoms are indistinguishable. After normalization, the representation of all the N orientation vector of the analyzed system in a reference in which all vector heads are in the origin is equivalent to N points lying in a sphere of unitary radius. In system characterized by long range order, it is expected to found all the points crowed around the two poles of the sphere corresponding to the direction of chain alignment. In amorphous structure, instead, the distributions of the points on the sphere is more homogeneous, since no special direction exists in the sample.

Table 4.2: Eigenvalues ε_i associated with the three axis of the inertia tensor calculated for each listed sample: all values are expressed in adimensional units

sample	$\varepsilon_{\parallel}$	$\varepsilon_{\perp 1}$	$\varepsilon_{\perp 2}$
pyridine	0.82	0.76	0.42
pyr+wat	0.81	0.70	0.49
tosylate	0.83	0.73	0.43
tos+pyr	0.77	0.73	0.50
tos+wat	0.78	0.65	0.57
water	0.70	0.66	0.64

In order to determine the direction along with the largest number of chains is aligned, a fictional unitary mass was attributed to each of the N points and all the components of the inertia tensor of the resulting mass distribution were computed. The mean direction of preferred alignment can then easily found by calculating the eigenvalues of the real non-negative defined matrix and looking for its column vector associated with the lowest eigenvalue: the comparison of eigenvalues magnitude can also provide a quantitative procedure to evaluate spatial anisotropy, which it has been graphically inspected analyzing using the projected density maps. The density maps for the pyridine and water scavenged samples are depicted in Figure 4.12.

The reported density maps clearly suggest, as confirmed by quantitative analysis carried on in the previous chapter and by eigenvalues evaluation (see Table 4.2) the existence of a consistent long range order in pyridine scavenged samples while water scavenged samples appears to be more amorphous. This effect which is consistent with data obtained for chain length distribution.

After the calculations of the three axis of inertia ellipsoid have been performed, the inertia and thermal conductivity tensors were simultaneously diagonalized in order to obtain the values of thermal conductivies along the three main axis directions. The off-diagonals entries resulted to be negligible respect the diagonal $\kappa_{\parallel}, \kappa_{\perp 1}, \kappa_{\perp 2}$ components, which are plotted for each samples in Fig. 4.13.

The results clearly confirm the role of chain length in determining the magnitude of the resulting thermal conductivity: it is in fact shown that samples characterized by longer chain (pyridine and pyridine+tosylate scavenged) exhibit higher in chain thermal conductivities compared to water scavenged samples, in which $\kappa_{\parallel}$ reaches its minimum, resulting indistinguishable from the two $\kappa_{\perp}$ components.

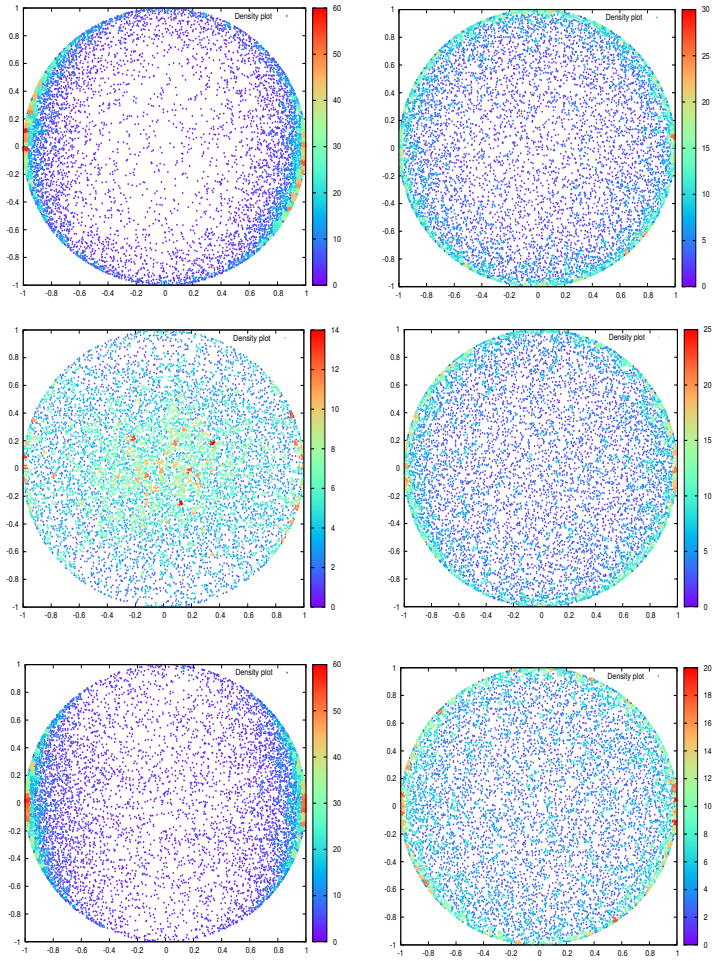

Figure 4.12: Density maps for pyridine (left) and water (right) polymerized samples projected in xy plane (first row), yz (second row) and xz (third row): the existence of long-range order structure with a preferential alignment direction is clearly visible in pyridine sample, while water sample appears more amorphous

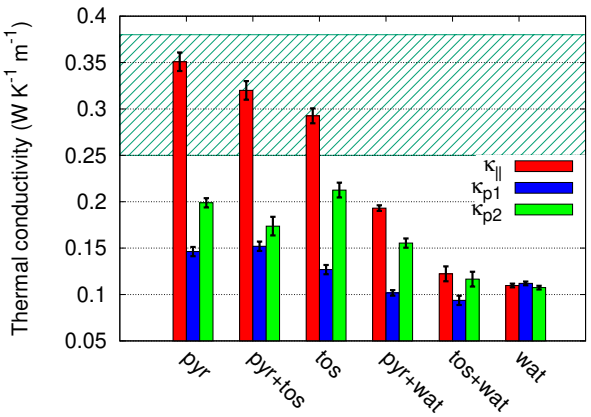

Figure 4.13: Thermal conductivities components along the direction of maximum alignment $\kappa_{||}$ and the two orthogonal directions $\kappa_{\perp 1,2}$[12]

It is interesting to observe that even if out-of-chain components result negligible respect to the $\kappa_{||}$ component in high anisotropic samples, a slight reduction is observed moving from pyridine scavenged samples to the water scavenged ones: this could possibly be explained by the fact that in amorphous-like samples the mean distance between monomeric units of different chains is greater than the corresponding distance in well crystallyzed samples, resulting in an increase in the interaction of monomers which can improve thermal transport.

4.3.3 Time evolution of κ during polymerization

The dependence of thermal conductivity from the chain length was also tested calculating the thermal conductivity on different samples at different stages of polymerization: the result, shown for each component and averaged in Fig. 4.14, clearly evidences the impact of increasing chain length on thermal conductivity. In particular, while along the direction of alignment of the maximum number of growing chains the increase of $\kappa_{||}$ is almost monotonic, along perpendicular directions could possibly read the signs of an internal reorganization in packing of the chains leading to sudden drop in $\kappa_{\perp}$ evolution in the last stage.

4.3.4 Modal analysis results

In order to provide additional characterization of the impact of morphological features on the vibrational modes (i.e. heat carriers) involved, a Green-Kubo modal analysis has been performed. In Fig.4.15 the average

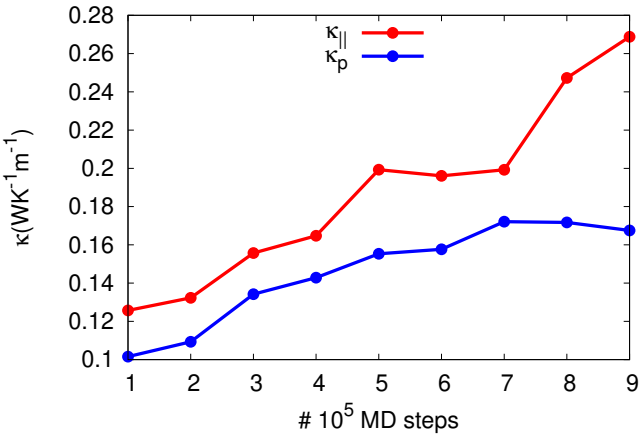

Figure 4.14: Thermal conductivities components of pyridine scavenged sample, $\kappa_{||}$ corresponding to the direction of alignment of the maximum number of growing chains[12]

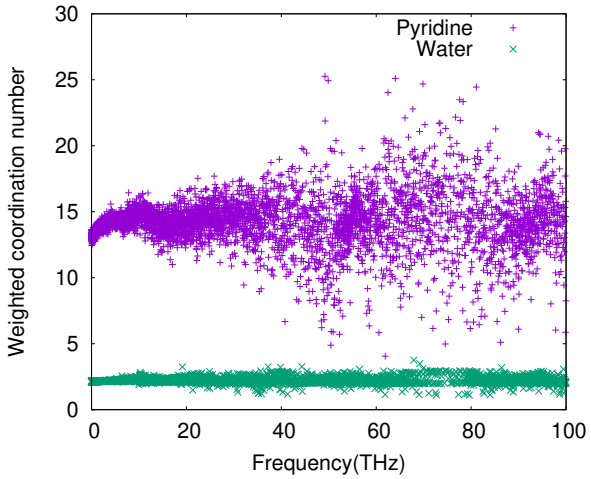

Figure 4.15: Average monomeric units involved in vibrational modes as function of the oscillation frequency for wat (purple) and pyr (green) samples[12]

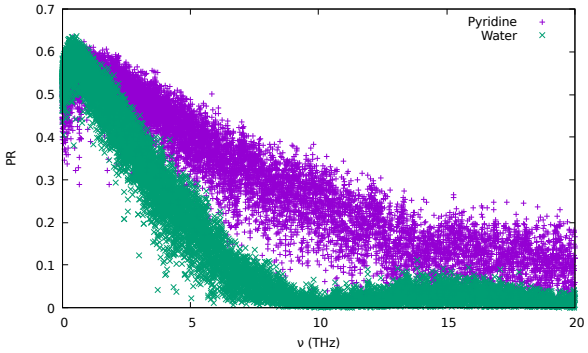

Figure 4.16: Estimated Participation Ratio (PR) as function of the frequency for wat (purple) and pyr (green) PEDOT samples[12]

weighted coordination number n_s (see eq.(4.32)) for pyr and wat samples is plotted as a function of the frequency ν of the vibrational eigenmodes.

Simulations indicate that the number of monomers involved in each vibrational modes in pyr samples is significantly higher compared to the one of wat samples. This is quite relevant in explaining the higher thermal conductivity corresponding to pyr samples, since the number of units involved in each vibrational mode is a direct measure of the spatial extent of the mode. It can be concluded that in pyr samples even low frequency vibrational modes are characterized by an overall extension of about $12 - 15$ monomeric units. Therefore, they are more effective in the thermal energy propagation if compared to the case of wat samples, in which the extent of each vibrational mode is limited to $2 - 3$ monomeric units in all the range of frequency investigated.

By further analyzing the corresponding participation ratio as defined in eq.(4.31) and reported in Fig.4.16, can be observed that in pyr samples the low frequency modes are more spatially extended compared to the case of pure wat samples. The participation ratio decays is in fact much slower than in the case of wat samples, determining a larger efficiency in propagating thermal energy. In the case of wat samples, on the other hand, the faster decay of PR indicates that such vibrational eigenmodes are spatially more confined. This property is detrimental in terms of thermal transport since eigenmodes above the frequency threshold of $\sim$ 5 THz cannot efficiently sustain extended heat currents along all the sample (Fig.4.17).

Our picture is confirmed by Fig.4.17 in which the normalized cumulative thermal conductivity κ_s (defined as in eq.(4.30)) is shown as a function of the frequency ν of the vibrational modes in the range $0 - 10$ THz. In both cases

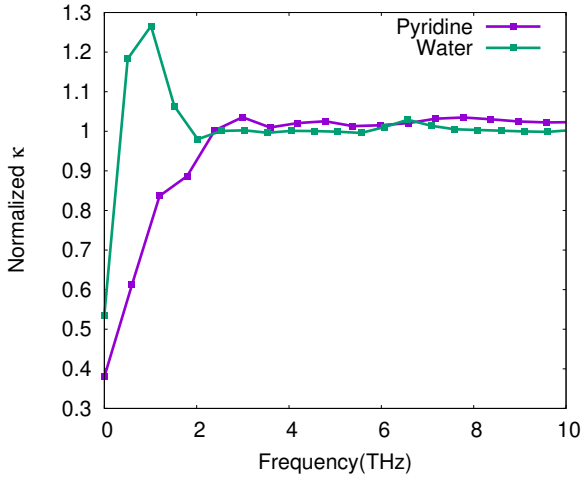

Figure 4.17: Normalized cumulative conductivity as function of the frequency for wat (purple) and pyr (green) samples.[12]

depicted in Fig.4.17 the cumulative thermal conductivity quickly converges to its final value at around 2 THz, however the approach is different: while in the case of pyr samples the convergence value is reached almost monotonically, in the case of wat samples, after an initial sharp increase, negative contributions are present in the range $1-2$ THz leading to a decrease of the cumulative thermal conductivity. This behavior, which is not in contrast with the definition of $\kappa_s(\nu)$ since the terms involved in Eq.(4.30) can also be non-positive, reveals the presence of a sharp decrease in the number of modes involved in heat propagation (the so called *propagons*)[21,23] in the range of frequency investigated and a corresponding increase in the number of modes related with a pure diffusion of the thermal energy (*diffusons*[21,23]).

Bibliography

[1] Luigi Cigarini, Alice Ruini, Alessandra Catellani, and Arrigo Calzolari. Conflicting effect of chemical doping on the thermoelectric response of ordered pedot aggregates. *Physical Chemistry Chemical Physics*, 20(7):5021–5027, 2018.

[2] Olga Bubnova, Zia Ullah Khan, Abdellah Malti, Slawomir Braun, Mats Fahlman, Magnus Berggren, and Xavier Crispin. Optimization of the thermoelectric figure of merit in the conducting polymer poly (3, 4-ethylenedioxythiophene). *Nature materials*, 10(6):429, 2011.

[3] HL Kwok. Thermal conductivity and zt in disordered organic thermoelectrics. *Journal of electronic materials*, 42(3):355–358, 2013.

[4] Kun Zhang, Jingjing Qiu, and Shiren Wang. Thermoelectric properties of pedot nanowire/pedot hybrids. *Nanoscale*, 8(15):8033–8041, 2016.

[5] Alessandro Crnjar, Claudio Melis, and Luciano Colombo. Assessing the anomalous superdiffusive heat transport in a single one-dimensional pedot chain. *Phys. Rev. Materials*, 2:015603, Jan 2018.

[6] Stefano Lepri, Roberto Livi, and Antonio Politi. Heat transport in low dimensions: introduction and phenomenology. In *Thermal transport in low dimensions*, pages 1–37. Springer, 2016.

[7] Kenichiro Aoki and Dimitri Kusnezov. Fermi-pasta-ulam β model: Boundary jumps, fourier's law, and scaling. *Physical review letters*, 86(18):4029, 2001.

[8] Stefano Lepri, Roberto Livi, and Antonio Politi. On the anomalous thermal conductivity of one-dimensional lattices. *EPL (Europhysics Letters)*, 43(3):271, 1998.

[9] Teng Zhang and Tengfei Luo. Morphology-influenced thermal conductivity of polyethylene single chains and crystalline fibers. *Journal of Applied Physics*, 112(9):094304, 2012.

[10] Nikoo Ghahramani and Mahmoud Rahmati. The effect of the molecular weight and polydispersity index on the thermal conductivity of polyamide 6: A molecular dynamics study. *International Journal of Heat and Mass Transfer*, 154:119487, 2020.

[11] Teng Zhang and Tengfei Luo. Role of chain morphology and stiffness in thermal conductivity of amorphous polymers. *The Journal of Physical Chemistry B*, 120(4):803–812, 2016. PMID: 26751002.

[12] Antonio Cappai, Aleandro Antidormi, Andrea Bosin, Dario Narducci, Luciano Colombo, and Claudio Melis. Impact of synthetic conditions on the anisotropic thermal conductivity of poly (3, 4-ethylenedioxythiophene)(pedot): A molecular dynamics investigation. *Physical Review Materials*, 4(3):035401, 2020.

[13] Claudio Melis, Riccardo Dettori, Simon Vandermeulen, and Luciano Colombo. Calculating thermal conductivity in a transient conduction regime: theory and implementation. *The European Physical Journal B*, 87(4):96, Apr 2014.

[14] Steve Plimpton. Fast parallel algorithms for short-range molecular dynamics. *Journal of Computational Physics*, 117(1):1 – 19, 1995.

[15] Shannon K Yee, Nelson E Coates, Arun Majumdar, Jeffrey J Urban, and Rachel A Segalman. Thermoelectric power factor optimization in pedot: Pss tellurium nanowire hybrid composites. *Physical Chemistry Chemical Physics*, 15(11):4024–4032, 2013.

[16] R.O. Agbaoye, P.O. Adebambo, J.O. Akinlami, T.A. Afolabi, Smagul Zh. Karazhanov, Davide Ceresoli, and G.A. Adebayo. Elastic constants and mechanical properties of pedot from first principles calculations. *Computational Materials Science*, 139:234 – 242, 2017.

[17] DA Case, IY Ben-Shalom, SR Brozell, DS Cerutti, TE Cheatham III, VWD Cruzeiro, TA Darden, RE Duke, D Ghoreishi, MK Gilson, et al. Amber 2018; 2018. *University of California, San Francisco*.

[18] Wei Lv and Asegun Henry. Direct calculation of modal contributions to thermal conductivity via green–kubo modal analysis. *New Journal of Physics*, 18(1):013028, 2016.

[19] Wei Lv and Asegun Henry. Phonon transport in amorphous carbon using green–kubo modal analysis. *Applied Physics Letters*, 108(18):181905, 2016.

[20] Hamid Reza Seyf, Kiarash Gordiz, Freddy DeAngelis, and Asegun Henry. Using green-kubo modal analysis (gkma) and interface conductance modal analysis (icma) to study phonon transport with molecular dynamics. *Journal of Applied Physics*, 125(8):081101, 2019.

[21] Aleandro Antidormi, Xavier Cartoixà, and Luciano Colombo. Nature of microscopic heat carriers in nanoporous silicon. *Physical Review Materials*, 2(5):056001, 2018.

[22] Philip B Allen, Joseph L Feldman, Jaroslav Fabian, and Frederick Wooten. Diffusons, locons and propagons: Character of atomie yibrations in amorphous si. *Philosophical Magazine B*, 79(11-12):1715–1731, 1999.

[23] Hamid Reza Seyf and Asegun Henry. A method for distinguishing between propagons, diffusions, and locons. *Journal of Applied Physics*, 120(2):025101, 2016.

Chapter 5

Charge transport and conductivity of PEDOT

5.1 Introduction

In the field of electronic materials adopting organic molecules as building blocks for devices, a special role is occupied by intrinsic conducting polymers..

As general common feature, intrinsic conducting polymers are characterized by the presence of sp^2 hybridized carbon orbitals which can form π molecular orbitals.

The peculiarity of π orbitals is the fact that the electrons nominally occupying them are at average distance larger compared to the electrons in more localized σ orbitals. This fact allow a conspicuous delocalization and makes them more suitable to transport the charge along the full extent of the molecular systems.

Charge transport results particularly efficient in intrinsic conducting polymers characterized by a quasi-linear carbon backbone. This kind of structures can be described in terms of two resonance structures in which alternating single and double bonds are present, as the case of polyacetylene and PEDOT, or in poly-aniline, in which nitrogen is present as well as carbon in the backbone.

In some situation, as in polyacetylene, however, the inherent symmetry which arises from resonance is usually broken, an interesting phenomenon called Peierls instability.[1]

This effect has important effects on the electronic structure. In the case

of poly-aniline, for example, it causes the opening of the HOMO-LUMO gap preventing the chains to acquire spontaneously a metallic conductive regime, whereas calculation of symmetric configuration suggest the overlap between HOMO-LUMO orbitals.

The formation of defects in the carbon backbone, however, is not always associated by the widening of HL gap. The addition of specific dopants to intrinsic conducting polymers, in fact, can also causes the introduction of new intra-gap levels, in strict analogy with the behavior observed in inorganic semiconductors as silicon.

These levels take origins from the transfer of an electron from the intrinsic conducting polymer to the dopant. The positive charge in intrinsic conducting polymer induces a structural deformation which causes positive charge localization named as polaron and its new intragap level associated.

The charge transport through polarons is strictly related with an another import features of the intrinsic conducting polymers involved in determining the overall electrical conductivity, the chain length.

In fact it can be shown using a very simple model known as the rectangular box approximation,[2] that as the chain length increases the corresponding HL gap gradually closes, a condition related, by definition, with the transition from insulating to a semi-metallic state.

It is, however, a generally recognized fact[3] that many properties can crucially influence σ as well as the thermal conductivity κ (analyzed in Chapter 4 of this Thesis): the doping level, the chain length (distribution) and the spatial organization of the chains, quantified as degree of crystallinity.

The mutual interaction of these factor introduces a degree of complexity which cannot be simply treated with the applications of the models used for inorganic semiconductors, since in the latter the periodicity allows, for some extent, a partial simplification of the quantum mechanical calculations required. The use of band model for intrinsic conducting polymers, for example, is frustrated by the broken of translational invariance.

An interesting insight is provided by the so called hopping models, in which transport is mainly governed by carrier hopping. The problem of charge transfer in hopping models is thus reviewed in terms of a percolation and all computational efforts are focused on the determination of the specific rate of percolation, or in more technical term, the hopping rate τ_0^{-1}.

A theory developed to study the problem of charge transfer in solution, the Marcus theory, can provide a valuable tool to estimate the actual value of τ_0^{-1}, In addition, a novel combination of the hopping model and Marcus theory is described in this Chapter together with its application on realistic micro-morphologies of PEDOT.

It is important to stress on the "realistic" adjective used. The lack of a clear, long-range symmetry in organic intrinsic conducting polymers, in fact, allows a vast panorama of micro-morphologies ranging from pure crystalline phase to amorphous structures. From a very essential point of view, these difference are due by the spatial organization (or packing) of the constitutive chains.

This circumstance must not be neglected since the difference in inter-molecular distances causes large effects in the overlap of delocalized π orbitals, the orbitals mainly involved in charge transport.

5.2 Computational approach

The starting point for the performed analysis is provided by the hopping rate κ according to Marcus[4] formalism

$$\kappa = \frac{2\pi}{\hbar} \frac{|H_{ab}|^2}{(4\pi k_B T \lambda)^{\frac{1}{2}}} \exp\left(-\frac{(\Delta G + \lambda)^2}{4\pi k_B T \lambda}\right) \tag{5.1}$$

where $|H_{ab}|^2$ is usually referred to as the charge transfer integral, defined as in Baumeier's work,[5] critically depending on the overlap between the orbitals affected by the charge transfer process; λ is the reorganization energy, i.e. the energy associated with the structural relaxation associated with the adiabatic transition from a neutral to a charged configuration of the molecules and the surrounding solvent environment and ΔG is the Gibbs free energy of reaction, including the solvation process, evaluated for the basic reaction scheme

$$\mathrm{A}^+ + \mathrm{B} \rightleftharpoons \mathrm{A} + \mathrm{B}^+ \tag{5.2}$$

as the proper sum of the Gibbs Free energies $G^{\mathrm{q}}_{\mathrm{X}}$ associated with each X chemical species with q total charge, as

$$\Delta G_{\mathrm{AB}} = G_{\mathrm{B}^+} + G_{\mathrm{A}} - G_{\mathrm{A}^+} - G_{\mathrm{B}} = \Delta G_{\mathrm{B}} - \Delta G_{\mathrm{A}} \tag{5.3}$$

All the energies are calculated at a DFT level using the B3LYP/6-311G(d,p) functional-basis set combination and the SMD solvation model[6] to take into account, implicitly, the effect of the surrounding solvent. In coherence with Chapter 3, ethanol was assumed as implicit solvent.

For this reason, the same summation scheme for the calculation of the Gibbs free energy as adopted in the Chapter 3 has been used, namely

$$\Delta G_{\mathrm{AB}} = \Delta G^0_{\mathrm{AB}} + \Delta G^{\mathrm{solv}}_{\mathrm{AB}} \tag{5.4}$$

where the superscript "0" references to the values estimated in vacuo while the symbol "solv" indicates the contribution due to the reorganization of the

solvent. No further thermodynamic corrections are here required since no variation of the number of moles is present for the reaction scheme in Eq. 5.2.

In order to simplify the following calculations, it is very useful to redefine the scale of energy used in Eq. 5.1. It is in fact possible to verify that by defining the u energy unit as

$$u = 4\pi k_{\mathrm{B}} T \simeq 0.32486 \text{ eV} \tag{5.5}$$

the Gibbs free energies of reaction and the reorganization energies can therefore be rewritten in the form of adimensional parameters

$$\begin{cases} \tilde{\lambda} = u^{-1}\lambda \\ \Delta\tilde{G} = u^{-1}\Delta G \end{cases} \tag{5.6}$$

and the Eq. 5.1 becomes

$$\begin{aligned} \kappa &= \frac{|H_{ab}|^2}{2k_{\mathrm{B}}T\hbar} \times \frac{1}{\sqrt{\tilde{\lambda}}} \exp\left(-\frac{(\Delta\tilde{G}+\tilde{\lambda})^2}{\tilde{\lambda}}\right) \\ &= \frac{1}{\tau_0} \times f(\Delta\tilde{G}, \tilde{\lambda}) \end{aligned} \tag{5.7}$$

where τ_0 and the function f of the adimensional parameters $\Delta\hat{G}$ and $\hat{\lambda}$ are defined as

$$\begin{aligned} \tau_0 &= \frac{2k_{\mathrm{B}}T\hbar}{|H_{ab}|^2} \\ f(\Delta\tilde{G}, \tilde{\lambda}) &= \frac{1}{\sqrt{\tilde{\lambda}}} \exp\left(-\frac{(\Delta\tilde{G}+\tilde{\lambda})^2}{\tilde{\lambda}}\right) \end{aligned} \tag{5.8}$$

It can be clearly observed that an accurate evaluation of the Gibbs free energy and the reorganization energy is crucial in determining the hopping rate of the system because of the presence of an exponential dependence in the parametric function $f(\Delta\tilde{G}, \tilde{\lambda})$.

In order to better clarify the influence of these energies on κ, it is interesting and useful to highlight some properties of the universal $f(\Delta\tilde{G}, \tilde{\lambda})$ function by analysing the iso-contours of the its natural logarithm

$$\ln(\kappa) = -\ln(\tau_0) + \ln\left(f(\Delta\tilde{G}, \tilde{\lambda})\right) \tag{5.9}$$

which can be rewritten as

$$\ln(\kappa) = -\frac{1}{2}\tilde{\lambda} - \frac{(\Delta\tilde{G}+\tilde{\lambda})^2}{\tilde{\lambda}} + \text{constant} \tag{5.10}$$

It can be preliminary observed that the Eq. 5.10 fails when the reorganization energy is zero $\tilde{\lambda} = 0$. This circumstance, however, is forbidden from a physical point of view since the energy difference associated with the charge transfer process in a molecule is always different from zero.

In contrast, for a given value of $\tilde{\lambda}$, no divergence arises by imposing a null Gibbs free energy of reaction. The resulting one-variable function, instead, reaches its maximum when no energy difference is present and this can corresponds, for example, to the case in which the charge transfer process 5.2 takes place between molecules of the same chemical specie, i.e. to the elemental reaction

$$A^+ + A \rightleftharpoons A + A^+ \tag{5.11}$$

As general rule of thumb, whenever you have an increase in the absolute value of the Gibbs free energy, $\Delta\tilde{G}$, an extreme favourable reaction is occurring if $\Delta\tilde{G} \ll 0$, while $\Delta\tilde{G} \gg 0$ leads to an exponential decay of the hopping rate, provided that the same or a very similar value of the reorganization energy is associated with all these mechanisms.

However, it must be stressed that, in realistic models, the reorganization energy and the Gibbs free energy are mutually dependent, even if the functional form of this dependence is difficult to be identified, since both the quantities are functions of the overall number of the molecular degrees of freedom of the involved chemical species in charge transfer.

Finally, it must also be noted that the factorization given in Eq. 5.7 does not justify, from a rigorous perspective, the possibility to completely separate calculations for the pre-factor τ_0 and for the universal f function. This is due to the fact that the charge transfer integral in τ_0 can be parameterized in terms of the molecular degrees of freedom affecting the reorganization energy and the reaction energy.

Because of these interconnecting dependencies, the direct application of Eq. 5.1 to the treatment of charge transport in a complex system (as our PEDOT sample), shares a common and critical point which was evidenced in the modelization of the polymerization scheme.

In this case the problem is represented by the complex interconnection between the basic quantities $|H_{ab}|$, ΔG and λ influencing the overall hopping rate .

In the specific cases of the study of charge transport mechanism in PEDOT by direct and recursive application of Eq. 5.1, the first crucial choice operated was a clear separation and treatment of the intra-chain charge transport, involving monomeric units belonging to the same PEDOT chain, and the inter-chain transport, in which the unit of charge is transferred from

a chain to another.

From a rapid analysis of the vast existing literature[7–12] it emerges that the modelization of charge transfer by Eq. 5.1 was applied only in the analysis of hopping between different molecular units, while no work was found in literature addressing the problem of intrachain transport by direct application of Eq. 5.1.

Intrachain transport is, instead, extensively analyzed in the framework of valence and conduction band theory requiring, however, a degree of crystallinity of the micromorphology which, in some cases, can often results unrealistic, even if they can provide interesting insight and an upper limit to mobilities and electrical conductivities.

Given this state of the art context, it seems interesting and worth of preliminary investigation to probe and verify whether if by assuming as starting point the micromorphologies generated by a realistic simulation of the polymerization, is possible to treat intrachain charge transport in PEDOT in the framework of Marcus-Abraham-Miller formalism and obtain mobilities comparable with experimental reported values or, in the worst scenario, at least confirming the universally accepted notion that intrachain transport overwhelms interchain one by one or two order of magnitude.

In the two following section the conceptual and computational protocol adopted to numerically treat these two different regimes is presented.

5.3 Interchain transport

Modelization of intrachain charge transport in PEDOT chains is achieved by direct exploitation of Marcus formula Eq.5.1 following an approach inspired by Evans'[13] and Deng's[14] work on charge percolation on amorphous systems.

Two very general underlying hypothesis are here stated in order to proceed. First (i) it has been assumed that charge transport in PEDOT is essentially mediated by holes in HOMO orbitals rather than electrons in LUMO, an assumption suggested by the fact that PEDOT is usually employed as an hole transport layer and the commonly used chemical doping is a p-doping from almost all experimental and technical applications; moreover, (ii) it is assumed that only the terminal monomeric units represent the active sites for inter-chain charge transfer by hopping, since in non-terminal units intra-chain transfer is dominant.

Starting from these assumptions, for each generated PEDOT sample the terminal monomeric units of each chain were identified and the position of their centre of mass were collected.

This elaboration makes possible to select all the isolated monomers, all

Table 5.1: Total number of active monomeric units for hopping interchain transport calculated from the corresponding chain length distribution n_{a}^{t}

sample	n_{a}^{t}
pyridine	1085
tosylate	1260
water	9395
pyr+tos	1132

the dimers and all the two extremities of each chain made up by $N \geq 3$ monomeric units.

The total number n_{a} of hopping active sites for each investigated sample is reported in Table 5.1 as derived from a direct calculation on the corresponding chain length distribution using the formula

$$n_{\mathrm{a}}^{t} = N_{\mathrm{HXH}} + 2\sum_{m\geq 2} N_{\mathrm{HX_mH}} \tag{5.12}$$

In the new simulation defined to study interchain transport, all the possible active sites for hopping are defined as combination of two monomers with a distance between the corresponding centers r_i within a cut-off radius r_0. For each ith couple we estimated the product

$$\kappa_i r_i^2 P_i \tag{5.13}$$

where κ_i is the site-specific hopping rate. P_i is the probability of charge transfer resulting from the occurrence of M available parallel channels and namely defined as

$$P_i = \frac{\kappa_i}{\sum_{j=1}^{M} \kappa_j} \tag{5.14}$$

where κ_i is the hopping rate for the ith transfer site under investigation and the sum runs over all the concurrent M sites.

By summing over all the total number of active monomeric units and excluding double summation over the same sites, a hole diffusion coefficient according to the Einstein formulation can be determined as[13,14]

$$D_h = \frac{1}{6}\sum_i \kappa_i r_i^2 P_i \tag{5.15}$$

and the resulting hole mobility reads as[13]

$$\mu_h = \frac{e}{k_B T} D_h \tag{5.16}$$

A critical point in evaluating each individual product 5.13 arises from the site specific nature of this quantity, which would require a specific calculation for each site of ΔG, λ and H_{ab} involved in κ_i.

This approach results to be computationally very expensive, since it would require several ab-initio calculations on monomeric couples. An alternative approach is suggested by the fact that both diffusion coefficient D_h and hole mobility μ_h are intrinsically time and spatial averages of the underlying real time process of charge transfer. This would generate an over-amount of information compared to the quantities accessible from a macroscopic and experimental point of view.

In detail, we estimated the transfer integral H_{ab} in a significative ensemble of mutual positions of two monomers. Fixed the position of the first monomeric units at the centre of spherical coordinates system (r, θ, ϕ), the second monomeric unit was placed at a distance r ranging from 3 to 10 Å by also varying the mutual inclination, at fixed distance.

The averaged H_{ab} value of transfer integral was successively calculated as

$$\langle H_{ab}(r) \rangle = \int d\theta \int d\phi H_{ab}(r, \theta, \phi) \tag{5.17}$$

and described,[15] in terms of a radial exponential decay

$$\langle H_{ab} \rangle = H_0 \exp(-\beta r) \tag{5.18}$$

and thus

$$|\langle H_{ab} \rangle|^2 = H_0^2 \exp(-2\beta r) \tag{5.19}$$

where the two parameters H_0^2 and 2β are determined by fitting in $H_0^2 = 216.43937$ eV^2 and $2\beta = 2.351806$ Å^{-1}.

It was further found that the simple relation Eq. 5.19 fails for distances below 2 Å which is expected because at very small intermonomeric separations spatial anisotropy is sufficiently high to prevent the assumption of radial symmetry in the formulation of $\langle H_{ab}(r) \rangle$ as function of just r.

This fact does not represent a serious limitation to the present approach since the presence of monomeric units involved in interchain transport at such low distance is almost impossible because of steric hindrance. However this failure at small distances but represents an issue in the case of intrachain transport.

A similar procedure was performed to estimate the universal function f depending on $\Delta\tilde{G}$ and $\tilde{\lambda}$, related to the the total length of the chain.

In this case, the chain length distributions (see Chapter 3) can be efficiently exploited in order to estimate the averages.

By considering the charge transfer process between two olygomers having m and n monomeric units

$$\mathrm{HX_nH^+ + HX_mH \rightleftharpoons HX_nH + HX_mH^+} \tag{5.20}$$

two auxiliary specific functions are defined as

$$\Delta\tilde{G}_{\mathrm{mn}} = \tilde{G}_{\mathrm{m}} - \tilde{G}_{\mathrm{n}} \tag{5.21}$$

$$\tilde{\lambda}_{\mathrm{mn}} = \frac{1}{2}(\tilde{\lambda}_{\mathrm{m}} + \tilde{\lambda}_{\mathrm{n}}) \tag{5.22}$$

where each $\tilde{G}_{\mathrm{m}}$ and $\tilde{\lambda}_{\mathrm{n}}$ term is calculated at B3LYP/6-311G(d,p) level and including reaction solvent field with SMD model as, respectively

$$\tilde{G}_{\mathrm{m}} = G(\mathrm{HX_mH^+}) - G(\mathrm{HX_mH}) \tag{5.23}$$

$$\tilde{\lambda}_{\mathrm{m}} = E^{\mathrm{neq}}(\mathrm{HX_mH^+}) - E^{\mathrm{eq}}(\mathrm{HX_mH^+}) + E^{\mathrm{neq}}(\mathrm{HX_mH}) - E^{\mathrm{eq}}(\mathrm{HX_mH}) \tag{5.24}$$

where neq and eq superscripts in Eq. 5.24 refers to the geometry at which the energy E of the aggregate is evaluated. More specifically, if the molecule is neutral, "eq" refers to the energy evaluated with molecular geometry relaxed at the ground state, while "neq" refers to the energy evaluated with the molecular geometry relaxed in the charged configuration.

After direct ab initio calculations, reported in Table 5.2, it was found that Eq. 5.23 and Eq. 5.24 can be described in terms of sum of exponential as

$$\tilde{G}_l = Ae^{-\alpha l} + Be^{-\beta l} + Ce^{-\gamma l} \tag{5.25}$$

and

$$\tilde{\lambda}_l = \lambda_1 e^{-\chi_1 l} + \lambda_2 e^{-\chi_2 l} \tag{5.26}$$

The resulting fitting function, displayed in Fig. 5.1, makes possible to easily proceed in the averaging.

The averaging process performed can be stated in the general form

$$\langle f(\Delta\tilde{G}, \tilde{\lambda})\rangle = \iint dx_i dx_j f(\Delta\tilde{G}(x_i, x_j), \tilde{\lambda}(x_i, x_j))\Omega(x_i, x_j) \tag{5.27}$$

where $\Omega(x_i, x_j)$ is a suitable probability density function which depends on the x_i and x_j lengths of the chains involved. The basic requirement for Ω is to fulfill the normalization condition

$$\iint dx_i dx_j \ \Omega(x_i, x_j) = 1 \tag{5.28}$$

Table 5.2: Calculated G_n, λ_n, $\tilde{G}_n$ and $\tilde{\lambda}_n$ for olygomers containing n monomeric units as resulting from DFT calculations at B3LYP/6-311G(d,p) level including ethanol solvent through SMD implicit solvent model.[6]

n	G_n(eV)	λ_n(eV)	$\tilde{G}_n$	$\tilde{\lambda}_n$
1	5.776625	1.465760	17.781579	4.511895
2	4.925796	1.191410	15.162561	3.667392
3	4.568686	1.005280	14.063307	3.094448
4	4.354676	0.874406	13.404542	2.691592
5	4.207618	0.777098	12.951869	2.392059
6	4.093014	0.698612	12.599096	2.150464
7	3.965237	0.635507	12.205773	1.956215
8	3.880355	0.582395	11.944490	1.792725
9	3.787900	0.535638	11.659895	1.648798
10	3.749619	0.494634	11.542059	1.522580
11	3.762624	0.458885	11.582091	1.412538
12	3.731435	0.424638	11.486085	1.307119
13	3.651881	0.39386	11.241202	1.21238
14	3.660069	0.366187	11.266406	1.1272
15	3.644008	0.341378	11.216968	1.050828

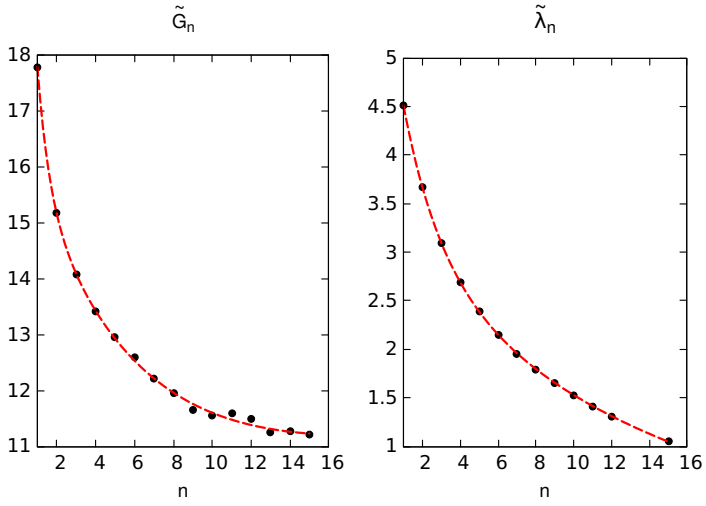

Figure 5.1: Calculated $\tilde{G}_n$ and $\tilde{\lambda}_n$ for olygomers with n chain length (black dots) and the superimposed fit functions (red dashed line)

Table 5.3: Calculated $\gamma = \frac{1}{2\hbar k_B T}\langle f(\Delta\tilde{G}, \tilde{\lambda})\rangle$, interchain diffusion coefficient D_{inter} and mobility μ_{inter} for holes in each investigated sample.

sample	γ ($eV^{-2}ps^{-1}$)	$D_{\text{inter}}(cm^2s^{-1})$	$\mu_{\text{inter}}(cm^2V^{-1}s^{-1})$
pyr	7.60193468	0.079906	3.0908
tos	6.05431348	0.11811	4.5687
wat	8.08951238	4.3228	167.20
pyr+tos	6.91424801	0.10544	4.0785

In the case of interchain charge transfer process involving a discrete set of n_a^t (as in Table 5.1) terminal monomeric units, it is reasonable to write Ω as the product of the individual probability

$$\Omega(x_i, x_j) = \frac{n_i n_j}{(n_a^t)^2} \tag{5.29}$$

where n_i and n_j represents the number of terminations belonging, respectively, to chains with length x_i and x_j, specifically obtained by the chain length distribution function

$$n_i = \begin{cases} N(\text{HXH}), \\ 2N(\text{HX}_\text{i}\text{H}), \quad \text{i} \geq 2 \end{cases} \tag{5.30}$$

where $N(\text{HX}_\text{n}\text{H})$, the chain length distribution function, is the number of chains with n monomeric units.

Given the discrete nature of the degree of freedom involved, Eq. 5.27 is thus calculated in the form of a sum

$$\langle f(\Delta\tilde{G}, \tilde{\lambda})\rangle = \frac{1}{(n_a^t)^2} \sum_{i,j} f(\Delta\tilde{G}_{ij}, \tilde{\lambda}_{ij}) N(\text{HX}_\text{i}\text{H}) N(\text{HX}_\text{j}\text{H}) \zeta_i \zeta_j \tag{5.31}$$

with $\zeta_i = 1$ if $i = 1$ and 2 otherwise.

Resulting $\gamma = \frac{1}{2\hbar k_B T}\langle f(\Delta\tilde{G}, \tilde{\lambda})\rangle$ for all investigated samples are reported in Table 5.3 in $eV^{-2}ps^{-1}$ units.

By introducing Eq. 5.19 in Eq. 5.13 for each ith site of a specific sample, averaged on its specific chain length distribution, we obtain

$$\kappa_i r_i^2 P_i = \gamma H_0^2 r_i^2 \exp(-2\beta r_i) \left(\frac{\exp(-2\beta r_i)}{\sum_j \exp(-2\beta r_j)} \right) \tag{5.32}$$

where summation is restricted on the j sites at a distance below a cutoff radius r_0.

After summation, inter-chain hole diffusion coefficient and mobility according to Eq. 5.15 and Eq. 5.16, respectively, are determined. Values are reported in Table 5.3. Among all the values of interchain mobility in Table 5.3, water is characterized by highest value, at least two order of magnitude above the others, while pyridine is characterized by lowest value.

Very similar values. instead, are present for all the other combination of scavengers adopted.

5.4 Intrachain transport

The treatment of intrachain charge transport follows the theoretical framework described in the previous section.

Starting from PEDOT olygomer HX_nH, the elemental intrachain charge transfer event consists in a hole moving along the same HX_nH molecule from the mth unit to the subsequent $(m+1)$th one, according the scheme

$$HX_1 \dots X_m^+ X_{m+1} \dots X_nH \rightleftharpoons HX_1 \dots X_m X_{m+1}^+ \dots X_nH \tag{5.33}$$

it is straightforward to verify that, according to the definitions Eq. 5.21 and Eq. 5.22, the Gibbs free energy and reorganization energy associated with the entire process are

$$\Delta\tilde{G}_{mm} = \Delta\tilde{G}_{intra} = 0 \tag{5.34}$$

$$\tilde{\lambda}_{mm} = \lambda_m \tag{5.35}$$

The only energy involved in the process is thus the contribution associated with the reorganization, which is averaged for each sample according its chain length distribution N_{HX_nH}.

In the case of intrachain transport, however, the total sites available for the charge transfer reads as

$$n'_a = \sum_{m\geq 2} mN_{HX_mH} \tag{5.36}$$

with summation starting from 2 since no intrachain transport can take place in the isolated monomers.

By redefining the probability density function Ω associated with each chain length distribution, the final form of the averaged universal function f takes the form

$$\langle f(\Delta\tilde{G}, \tilde{\lambda})\rangle = \frac{1}{(n'_a)} \sum_{m\geq 2} f(0, \tilde{\lambda}_m) mN_{HX_mH} \tag{5.37}$$

Table 5.4: Calculated $\gamma = \frac{1}{2\hbar k_B T}\langle f(\Delta\tilde{G}, \tilde{\lambda})\rangle$, intrachain diffusion coefficient D_{intra} and mobility μ_{intra} for holes in each investigated sample.

sample	γ ($eV^{-2}ps^{-1}$)	$D_{\text{intra}}(cm^2s^{-1})$	$\mu_{\text{intra}}(cm^2V^{-1}s^{-1})$
pyr	203.549	147.627	5710.21
tos	170.769	17.0795	660.635
wat	8.08951	0.0147273	0.569653
pyr+tos	251.007	187.115	7237.6

Referring to the inaccuracy of the radial approximation (Eq. 5.19) for short distances, direct calculations of $|H_{ab}(n)|^2$ for fragments with increasing chain length n in the range [2:15] monomeric units were performed.

Starting from a optimized chains with length n, two fragments were defined as the two portions with length $\frac{n}{2}$ which are separated by a $C-C$ bond length $\delta = 1.4144$ Å, as resulting from the optimization

The corresponding $|H_{ab}(n)|^2$ was successively averaged according

$$\langle |H_{ab}|^2 \rangle = \frac{1}{n'_a} \sum_{m \geq 2} |H_{ab}(m)|^2 \; m N_{\text{HX}_\text{m}\text{H}} \tag{5.38}$$

assuming for all $m \geq 15$ the value found at $m = 15$.

The resulting values of averaged γ prefactor, mobility and the diffusion coefficient for intrachain charge transport are reported in Table 5.4.

As expected, it was found for all the samples but water that intrachain transport is more efficient than its interchain counterparts, which thus acts as the main bottleneck of the overall mobility.

In particular, the presence of pyridine+tosylate is associated with higher intrachain hole mobilities, followed by the two pyridine combination and the two tosylate.

5.5 Total average mobility

In order to extract an overall hole mobility for each sample by combining the intrachain and interchain obtained values, it was found reasonable to apply the Matthiessen's rule

$$\frac{1}{\mu_h} = \frac{1}{\mu_{\text{intra}}} + \frac{1}{\mu_{\text{inter}}} \tag{5.39}$$

since the terminal monomeric sites in which charge is transferred by hopping from one chain to another can be considered, ideally, as a scattering event perturbing the coherent transport in a long PEDOT chain.

Table 5.5: Overall hole mobility μ_{h} calculated by combining intra- and inter- mobilities using Matthiessen's rule

sample	$\mu_{\mathrm{h}}(\mathrm{cm}^2\mathrm{V}^{-1}\mathrm{s}^{-1})$
pyr	3.089
tos	4.537
wat	0.5677
pyr+tos	4.076

The only exception is constituted by the water samples where interchain transport (Table 5.3) appears to dominate over its intrachain counterpart (Table 5.4). Also in this case, however, applicability of Matthiessen's rule was found plausible, with intrachain charge flow interfering with pure hopping interchain transport.

The resulting mobilities, listed in Table 5.5, display a non monotonical behaviour, which after an initial increase with average chain length, decreases in the case of pyridine samples, were very long chains (up to 32 m.u.) are present.

As can be observed by the analysis of the values reported in Table 5.2 and 5.4, this drops is due to the fact that even if intrachain hole transport monotonically increases with chain length, the hopping rate for interchain transfer in pyridine is lower compared to the pyridine+tosylate and tosylate scavenged samples.

This is effect is directly connected with two aspects inherent to the micromorpholgy of the samples, i.e. (i) the large distance between interchain active sites due the presence of very long chains, which directly affects the magnitude of $|H_{ab}(r)|^2 \propto \exp(-\beta r)$ and (ii) to a significant decrease of the γ factor due to the specific energetic balance of the charge transfer reaction.

Unfortunately, at the best of our knowledge, no systematic experimental is present in literature describing the exact behaviour of mobility μ_h as a function of chain length and all the computational estimates are performed on very crystalline (and unrealistic) structures, in which an arbitrary unitary cell is defined in order to properly apply the band model.

However, since electrical conductivity can be easily calculated given the hole density in the sample, in order to test the obtained results, preliminary calculations have been performed to produce the molecular Total Density of States (TDOS) (Fig. 5.2) for each PEDOT chain included in the simulation box.

It is, in fact, reasonable to expect that the presence of very large chains

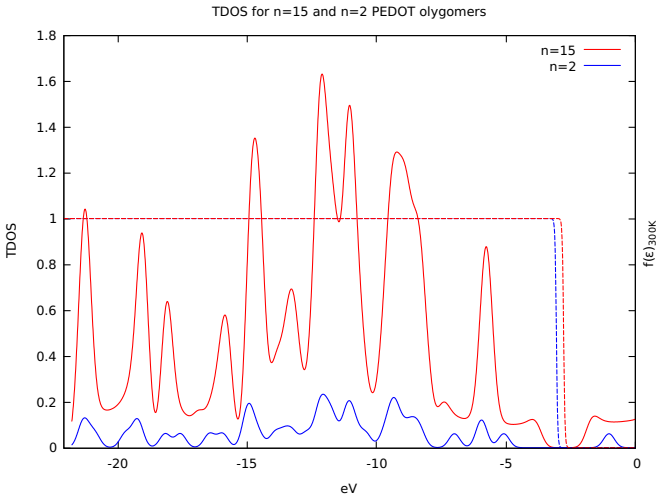

Figure 5.2: Calculated TDOS for PEDOT olygomers with 15 (red solid curve) and 2 (blue solid curve) m.u.chain length. Corresponding Fermi-Dirac distributions (dashed curve) at 300K are superimposed.

in pyridine due to an overall drop of the HOMO-LUMO gap and the shift of Fermi level as chain length increases (values reported in Table 5.6)

Preliminary calculations show that the estimated intrinsic (thermal activated) hole density n_h can vary from $\sim 5.6\ 10^{10}\text{cm}^{-3}$ to $\sim 2.4\ 10^{15}\text{cm}^{-3}$ when average chain length of a monodisperse sample (with an overall number of 10'000 monomeric units) increases from 5 to 15 monomeric units.

5.6 Intrinsic hole concentrations

The concentration of hole in intrinsic (non doped) PEDOT chains is evaluated by combining the total density of states (TDOS) $g_i(E)$ for each ith molecule contained in the investigated sample with volume V and the Fermi-Dirac distribution for hole $f_{h,i}(E)$

$$f_{h,i}(E) = \frac{1}{1 + \exp\left(\frac{\epsilon_\text{F} - E}{k_\text{B} T}\right)} \tag{5.40}$$

which in the more general case are combined according to

$$n_h = \frac{1}{V} \sum_i \int_{-\infty}^{\epsilon_\text{F}} g_i(E) f_{h,i}(E) dE \tag{5.41}$$

Table 5.6: HOMO-LUMO gap Δ, Fermi energy ϵ_F, distance between HOMO level and Fermi energy, HOMO and LUMO energies (all in eV units) as functions of the olygomers chain length n expressed in monomeric units. $n = \infty$ corresponds to a dimer simulated in PBC along chain direction. A remarkable reduction can be observed in transition from $n = 2$ to $n = 15$ chain length. All data are calculated using Gaussian 16[16] suite at DFT/B3LYP/6-311G(d,p) level.

n	Δ(eV)	ϵ_F(eV)	$\lvert\epsilon_F - E_{\mathrm{H}}\rvert$ (eV)	E_{H}(eV)	E_{L}(eV)
1	5.7144720	-3.1479350	2.8572360	-6.0051710	-0.2906990
2	4.0661430	-3.0478925	2.0330715	-5.0809640	-1.0148210
3	3.3158160	-2.9804360	1.6579080	-4.6383440	-1.3225280
4	2.9031010	-2.9379175	1.4515505	-4.3894680	-1.4863670
5	2.6471230	-2.9101485	1.3235615	-4.2337100	-1.5865870
6	2.4750660	-2.8894270	1.2375330	-4.1269600	-1.6518940
7	2.3544370	-2.8738215	1.1772185	-4.0510400	-1.6966030
8	2.2655380	-2.8618620	1.1327690	-3.9946310	-1.7290930
9	2.1988150	-2.8520115	1.0994075	-3.9514190	-1.7526040
10	2.1466510	-2.8440795	1.0733255	-3.9174050	-1.7707540
11	2.1057260	-2.8373580	1.0528630	-3.8902210	-1.7844950
12	2.0727450	-2.8317255	1.0363725	-3.8680980	-1.7953530
13	2.0447450	-2.8259435	1.0223725	-3.8483160	-1.8035710
14	2.0235200	-2.8228680	1.0117600	-3.8346280	-1.8111080
15	2.0048260	-2.8192630	1.0024130	-3.8216760	-1.8168500
16	1.9891790	-2.8161195	0.9945895	-3.8107090	-1.8215300
20	1.9454240	-2.8068680	0.9727120	-3.7795800	-1.8341560
22	1.9309740	-2.8036160	0.9654870	-3.7691030	-1.8381290
25	1.9150280	-2.7998880	0.9575140	-3.7574020	-1.8423740
27	1.9069740	-2.7979560	0.9534870	-3.7514430	-1.8444690
32	1.8745110	-2.8145145	0.9372555	-3.7517700	-1.8772590
∞	1.85347	-2.783405	0.926735	-3.710140	-1.856670

Table 5.7: Intrinsic hole concentrations $n_h(\lambda)$ at 300K for monodisperse samples with chain length λ in range $2-32$ monomeric units

λ	$n_h(\lambda)$ (cm^{-3})
1	$3.9696675\ 10^{-15}$
2	$1.0142062\ 10^{-1}$
3	$1.1066254\ 10^{5}$
4	$2.8127250\ 10^{8}$
5	$3.1201642\ 10^{10}$
6	$7.5572440\ 10^{11}$
7	$6.1271810\ 10^{12}$
8	$2.7917480\ 10^{13}$
9	$9.4906186\ 10^{13}$
10	$2.9675626\ 10^{14}$
11	$6.7800330\ 10^{14}$
12	$7.5894642\ 10^{14}$
13	$8.1517738\ 10^{14}$
14	$1.2374121\ 10^{15}$
15	$1.2342776\ 10^{15}$
16	$1.3161294\ 10^{15}$
20	$1.8129169\ 10^{15}$
22	$2.0311944\ 10^{15}$
25	$2.2914507\ 10^{15}$
27	$2.5008525\ 10^{15}$
32	$2.7501537\ 10^{15}$

with TDOS for each molecule (EDOT olygomer) is extracted through Multiwfn software[17] from single point calculation of orbitals population at DFT B3LYP/6-311G(d,p) on the geometry optimized at the same level of theory using Gaussian 16.[16]

In order to proceed with the integration, a normalized Gaussian broadening function with FWHM= 0.5 eV is assigned at each TDOS peak. The lowest energy of integration interval is chosen at $\sim$ 2418.15eV, where Fermi-Dirac distribution is substantially zero.

Table 5.7 reports our calculations for the intrinsic hole concentrations for monodisperse samples with chain length n and a total of 10^4 monomeric units.

Since data for increasing chain length show an overall convergence behaviour, the logarithm of concentrations, $\log10(n_h)$, were fitted using the

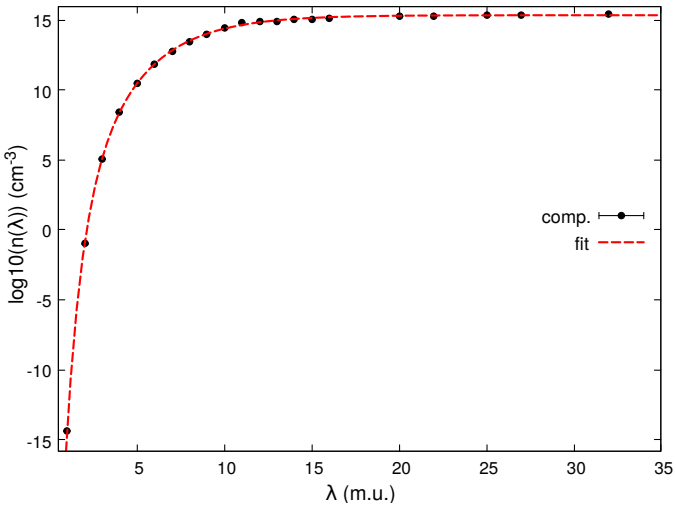

Figure 5.3: Calculated intrinsic hole concentrations n_h (black points) reported in Table 5.7 and fitted $n_h(\lambda)$ (red dashed line) for pristine monodisperse PEDOT samples with increasing chain length. A saturation concentration ($n_h(\lambda \to \infty)$) can be extrapolated in $(3.15 - 3.56) \cdot 10^{15}\text{cm}^{-3}$ from fitting procedure.

decay trial function

$$f(\lambda) = A + b\,\exp(-c\lambda) + d\,\exp(-s\lambda) \tag{5.42}$$

which, as depicted in Fig. 5.3, was found to describe reasonably well the observed data trend with the values of parameters fixed by the fitting procedure, with a final reduced $\chi^2_r = 5.5\ 10^{-2}$ (denoting a remarkable over-fitting)

$$\begin{aligned} A &= 15.3532 \pm 0.02945 \\ b &= -40.5661 \pm 0.9271 \\ c &= 1.17079 \pm 0.06273 \\ d &= -23.6575 \pm 1.2 \\ s &= 0.320407 \pm 0.009025 \end{aligned} \tag{5.43}$$

In the limit of very large chain length $\lambda \to \infty$, a possible estimate of the intrinsic hole concentrations results in $n_h = (2.25 - 2.76) \cdot 10^{15}\text{cm}^{-3}$.

The estimated hole concentrations and the resulting electrical conductivities due by hole contributions calculated according to the formula

$$\sigma = e\mu_h n_h \tag{5.44}$$

Table 5.8: Intrinsic hole concentrations n_h at 300K for the investigated samples, overall hole mobilities and resulting conductivities

sample	n_h (cm^{-3})	$\mu_h(cm^2V^{-1}s^{-1})$	$\sigma(\Omega^{-1}cm^{-1})$
pyr	$1.91032\ 10^{15}$	3.089	$9.4544097\ 10^{-4}$
tos	$1.54071\ 10^{15}$	4.537	$11.199537\ 10^{-4}$
wat	$4.34560\ 10^{5}$	0.5677	$3.9525651\ 10^{-14}$
pyr+tos	$1.81038\ 10^{15}$	4.076	$11.822728\ 10^{-4}$

for the investigated samples are listed in Table 5.8.

Several interesting results emerge by analysis of reported data.

First, it can be clearly noticed that all the samples are characterized by very low electrical conductivity, which is something expected in undoped PEDOT.

Beside this consideration, the huge impact of chain length distribution on σ, as suggested in the previous Section, is here demonstrated. While water sample can be in fact considered a pure insulator, all the samples with a broader chain length distribution and a greater average chain length are characterized by electrical conductivities with order of magnitude of $10^{-4} - 10^{-5}\ \Omega^{-1}cm^{-1}$. Such an increase is mainly due to the corresponding increase of the hole density due to the occurrence of longer chains.

Finally, it can be observed that the increase of hole densities in pyridine compared to the tosylate case partially compensates the reduction in hole mobility μ_h. By direct comparing pyridine with tosylate case, for example, despite an observed reduction of 31.91% of mobility, the corresponding drop in electrical conductivity σ amount to 15.58%.

5.7 Extrinsic hole concentrations

Following the computational results in Zozoulenko's work[18] indicating that pristine (i.e. as polymerized) PEDOT samples naturally possess a 33% hole doping level, a new estimate of electrical conductivity σ was performed using as starting point the underlying chain length distribution.

The overall hole density N_h is calculated in the doped case as

$$N_h = \frac{1}{V} \sum_{m \geq 3} \text{int}\left(\frac{m}{3} N(\text{HX}_\text{m}\text{H})\right) \tag{5.45}$$

where the int function (integer part) is introduced to exactly reproduce the insertion of 1 hole every three monomeric units in the simulation box with side $l = 118$ Å. The calculated hole concentrations and the resulting electri-

Table 5.9: Extrinsic hole concentrations N_h estimates for the investigated samples, overall hole mobilities and resulting conductivities

sample	N_h (cm^{-3})	$\mu_h(cm^2V^{-1}s^{-1})$	$\sigma(\Omega^{-1}cm^{-1})$
pyr	$1.99327\ 10^{21}$	3.089	$9.86492\ 10^2$
tos	$2.00605\ 10^{21}$	4.537	$1.45821\ 10^3$
wat	$3.66396\ 10^{20}$	0.5677	$3.33257\ 10$
pyr+tos	$1.95492\ 10^{21}$	4.076	$1.27666\ 10^3$

Table 5.10: Comparison with experimental data[19]

sample	$\sigma_h(\Omega^{-1}cm^{-1})$	$\sigma^{exp}(\Omega^{-1}cm^{-1})$
pyr	986.492	191 ± 17
tos	1458.21	352 ± 58
pyr+tos	1276.66	128 ± 4

cal conductivities are presented in Table 5.9.

As in the case of pure intrinsic (thermal activated) data, also in this case it can be noted that all the polymerized samples are characterized by hole concentrations of the same order of magnitude (10^{21}) while water-scavenged sample (almost unpolymerized) concentrations is remarkably lower but still comparable with pyridine and tosylate cases.

For this reason, mobilities play in extrinsic case a more important role in determining the electrical conductivity σ, which reaches its maximum in tosylate-scavenged samples ($\sim 1400\Omega^{-1}cm^{-1}$).

5.8 Comparison with experimental data

The hopping computational model described is still in a very early stage of development. However, we tried to compare the obtained values for σ and μ_h with the experimental data present in literature to verify if the model is able to recognize at least at a qualitative level, the observed trends.

In the case of the hole mobilities, our data are of the same order of magnitude with the corresponding experimental values reported.[20]

For a comparison of electrical conductivity, in Table 5.10 our values of σ_h for pyridine, tosylate and pyridine+tosylate samples are compared with the corresponding experimental data provided by Marquez and Narducci.[19] The experimental samples were generated using the chemical coating polymerization technique. In all the samples, the iron(III) tosylate is simultaneously used as oxidant for the polymerization and dopant.[19] A commercial solution of iron(III)tosylate in buthanol at 40% w/w, the CLEVIOS^{TM} CB 40,

was diluted to reach 30% concentration.[19] Pyridine is eventually added to control the reaction kinetics before deposition and successive heating.[19]

The values reported in Table 5.19 refer, respectively, to samples synthesized using the initial molar ratios

- EDOT: $Fe(Tos)_3$ = 1:2.55, with label "tos" in our Table;
- EDOT: $Fe(Tos)_3$: pyridine=1:2.55:1.10 ("pyr+tos");
- EDOT: $Fe(Tos)_3$: pyridine=1:2.55:2.00 ("pyr").

The overall σ_h absolute values largely overestimate the experimental σ^{exp} data, a circumstance which can possibly related with an overstimate of the charge carrier density in our calculations. It is however possible to observe that our calculations as well as the experiments are able to predict the highest value of σ in tosylate sample.

The emergence of tosylate as the best scavenger for σ_h can be related to the observed presence of the peak in chain length distribution discussed in Chapter 3 and related to the tie chains connecting crystallite proposed by Salleo[21] as the origin of efficient electronic transport.

As future perspective, a possible strategy to improve the accuracy of the developed method could be related to the explicit calculation of the quantities involved in the hopping rate, by avoiding the averaging procedure.

Bibliography

[1] Z. G. Soos and G. W. Hayden. Dimerization and peierls instability in polyacetylene. *Molecular Crystals and Liquid Crystals Incorporating Nonlinear Optics*, 160(1):421–432, 1988.

[2] Edward L Wolf. Quantum nanoelectronics. *An Introduction to Electronic Nanotechnol*, 2009.

[3] Magatte N. Gueye, Alexandre Carella, Jérôme Faure-Vincent, Renaud Demadrille, and Jean-Pierre Simonato. Progress in understanding structure and transport properties of pedot-based materials: A critical review. *Progress in Materials Science*, 108:100616, 2020.

[4] Rudolph A. Marcus. Electron transfer reactions in chemistry. theory and experiment. *Rev. Mod. Phys.*, 65:599–610, Jul 1993.

[5] Björn Baumeier, James Kirkpatrick, and Denis Andrienko. Density-functional based determination of intermolecular charge transfer properties for large-scale morphologies. *Phys. Chem. Chem. Phys.*, 12:11103–11113, 2010.

[6] Aleksandr V Marenich, Christopher J Cramer, and Donald G Truhlar. Universal solvation model based on solute electron density and on a continuum model of the solvent defined by the bulk dielectric constant and atomic surface tensions. *The Journal of Physical Chemistry B*, 113(18):6378–6396, 2009.

[7] Jerzy Paczkowski and Zdzislaw Kucybala. Generalization of the kinetic scheme for a dye-photosensitized free-radical polymerization initiating system via an intermolecular electron-transfer process. application of marcus theory. *Macromolecules*, 28(1):269–273, 1995.

[8] Jerzy Paczkowski and Zdzislaw Kucybala. Generalization of the kinetic scheme for photoinduced polymerization via an intermolecular electron transfer process. 2. application of the marcus theory. *Macromolecules*, 29(15):5057–5064, 1996.

[9] Catarina M Paquete and Ricardo O Louro. Unveiling the details of electron transfer in multicenter redox proteins. *Accounts of Chemical Research*, 47(1):56–65, 2014.

[10] Dmitry Godovsky. Modeling the ultimate efficiency of polymer solar cell using marcus theory of electron transfer. *Organic Electronics*, 12(1):190–194, 2011.

[11] Riccardo Volpi, Racine Nassau, Morten Steen Norby, and Mathieu Linares. Theoretical study of the charge-transfer state separation within marcus theory: the c60-anthracene case study. *ACS applied materials & interfaces*, 8(37):24722–24736, 2016.

[12] Lekshmi Sudha Devi, Mohammad K Al-Suti, Carsten Dosche, Muhammad S Khan, Richard H Friend, and Anna Kohler. Triplet energy transfer in conjugated polymers. i. experimental investigation of a weakly disordered compound. *Physical Review B*, 78(4):045210, 2008.

[13] David R. Evans, Hyunwook S. Kwak, David J. Giesen, Alexander Goldberg, Mathew D. Halls, and Masahito Oh-e. Estimation of charge carrier mobility in amorphous organic materials using percolation corrected random-walk model. *Organic Electronics*, 29:50 – 56, 2016.

[14] Wei-Qiao Deng and William A. Goddard. Predictions of hole mobilities in oligoacene organic semiconductors from quantum mechanical calculations. *The Journal of Physical Chemistry B*, 108(25):8614–8621, 2004.

[15] R.A. Marcus and Norman Sutin. Electron transfers in chemistry and biology. *Biochimica et Biophysica Acta (BBA) - Reviews on Bioenergetics*, 811(3):265 – 322, 1985.

[16] M. J. Frisch, G. W. Trucks, H. B. Schlegel, G. E. Scuseria, M. A. Robb, J. R. Cheeseman, G. Scalmani, V. Barone, G. A. Petersson, H. Nakatsuji, X. Li, M. Caricato, A. V. Marenich, J. Bloino, B. G. Janesko, R. Gomperts, B. Mennucci, H. P. Hratchian, J. V. Ortiz, A. F. Izmaylov, J. L. Sonnenberg, D. Williams-Young, F. Ding, F. Lipparini, F. Egidi, J. Goings, B. Peng, A. Petrone, T. Henderson, D. Ranasinghe, V. G. Zakrzewski, J. Gao, N. Rega, G. Zheng, W. Liang, M. Hada, M. Ehara, K. Toyota,

R. Fukuda, J. Hasegawa, M. Ishida, T. Nakajima, Y. Honda, O. Kitao, H. Nakai, T. Vreven, K. Throssell, J. A. Montgomery, Jr., J. E. Peralta, F. Ogliaro, M. J. Bearpark, J. J. Heyd, E. N. Brothers, K. N. Kudin, V. N. Staroverov, T. A. Keith, R. Kobayashi, J. Normand, K. Raghavachari, A. P. Rendell, J. C. Burant, S. S. Iyengar, J. Tomasi, M. Cossi, J. M. Millam, M. Klene, C. Adamo, R. Cammi, J. W. Ochterski, R. L. Martin, K. Morokuma, O. Farkas, J. B. Foresman, and D. J. Fox. Gaussian˜16 Revision C.01, 2016. Gaussian Inc. Wallingford CT.

[17] Tian Lu and Feiwu Chen. Multiwfn: A multifunctional wavefunction analyzer. *Journal of Computational Chemistry*, 33(5):580–592, 2012.

[18] Donghyun Kim and Igor Zozoulenko. Why is pristine pedot oxidized to 33%? a density functional theory study of oxidative polymerization mechanism. *The Journal of Physical Chemistry B*, 123(24):5160–5167, 2019. PMID: 31124678.

[19] Arturo Klaus Marquez Guaman and Dario Narducci. personal communication, 2020.

[20] Yow-Jon Lin, Jhe-You Lee, and Shang-Min Chen. Changing electrical properties of pedot:pss by incorporating with dimethyl sulfoxide. *Chemical Physics Letters*, 664:213 – 218, 2016.

[21] Scott Himmelberger, Koen Vandewal, Zhuping Fei, Martin Heeney, and Alberto Salleo. Role of molecular weight distribution on charge transport in semiconducting polymers. *Macromolecules*, 47(20):7151–7157, 2014.

Chapter 6

Conclusions and future perspectives

At the end of this Thesis, several conclusions can be stated, answering to the questions raised in Chapter 1.

The use of a multiscale approach, combining the quantum level information of the Gibbs free energies of reactions ΔG with the classical evolution simulated via Molecular Dynamics, has been proved successful to elucidate the role of the reactants used in PEDOT polymerization.

In particular, the analysis of the free energies as resulting from DFT calculations, clearly suggested that pyridine and tosylate anions can be identified as the proton scavengers.

By contrast, water, which have been proposed as possible proton scavenger, according to the performed calculations is very unlikely related to the process of scavenging. This conclusion does not exclude, however, that water could possibly play a role in driving the polymerization.

The specific chemical species of proton scavenger involved in the polymerization was proved crucial in affecting the micromorphologies of the *in silico* simulated samples.

Starting from a monodisperse distribution of isolated EDOT monomers, in fact, the adopted polymerization algorithm has produced, after MD simulation steps, PEDOT samples with completely different morphologies.

These differences were quantified by using three main descriptors, (i) the chain length distribution $n(\lambda)$, (ii) the volume occupied by the crystallites V_{C} and (iii) the average chain length $\langle\lambda\rangle$.

It was observed that all the scavenger combinations giving rise to signif-

icantly low ΔG of reaction are related with an increase of both $\langle\lambda\rangle$ and V_{C}, suggesting that the enhance of chain length leads to an increase of the overall crystallinity of the samples. In other terms, the performed simulations suggest that the emergence of long range order phase is crucially determined by the adopted proton scavenger.

More interestingly, it was found that the increase of the "efficiency" of the proton scavenger is linked with a progressive broadening of the chain length distribution $n(\lambda)$, with water scavenged-samples characterized by the narrowest $n(\lambda)$, while in the case of pyridine $n(\lambda)$ ranges from 1 up to 32 monomeric units of length. Moreover, by evaluating the Polidispersivity (PDI), a non trivial behaviour of $n(\lambda)$ was found in the case of tosylate scavenged samples, where a tri-modal distribution was observed. In particular, the occurrence of one specific peak at 13 monomeric units is compatible with the recent hypothesis of the crucial role played in carrier transport of "tie chains" responsible for charge transfer between the crystallites.

A direct comparison of the simulated XRD spectrum with the experimental data was used to assess the validity of the computational protocol, which was able to reproduced the position of the $\pi - \pi$ interchain stacking distance in fair agreement with experiments.

The morphologies resulting from the role of different proton scavengers were related, as expected, with very different behaviour in terms of both thermal and charge transport properties.

In particular, we focused on the calculation of: (i) the thermal conductivity κ, (ii) the hole mobility μ_h and (iii) the hole contribution to electrical conductivity σ_h. σ and κ, in fact, are directly related with the thermoelectric figure of merit zT.

In the case of thermal transport, evaluated using classical Molecular Dynamics, the role of proton scavenger proved to be crucial in determining the onset of an anisotropy, which we explained in terms of the chain length distribution by decomposing the thermal conductivity in a parallel $\kappa_{||}$ and perpendicular $\kappa_{\perp}$contribution to the chain directions.

It was found that as the chain length increases, the raise of $\kappa_{||}$ is faster than the one observed for $\kappa_{\perp}$, a behavior which was monitored at different stages of polymerization.

As due to the effect of chain length on the thermal conductivity, morphologies generated using pyridine or tosylate molecules as scavengers are characterized by a higher thermal conductivity than water based samples.

Electronic transport, evaluated in terms of percolation of charge with hopping rates estimated using Marcus theory, are also largely affected by the morphology.

The morphologies generated by the combinations of pyridine and pyridine+tosylate show relatively high values of σ_h, with the highest σ value reached in the case of tosylate scavenged samples.

Our calculations are able to identify tosylate as the best scavenger in terms of electronic conductivity σ_h. This results is confirmed by the experimental data showing the same preminence of tosylate over other scavenger choices.

However the overall σ_h absolute values are largely different from experiment which could be possibly related to the difficulty in estimating and controlling the charge carrier density, crucial in determining σ_h.

The next step in order to further characterize the carrier transport properties will be the explicit calculation of the quantities involved in the hopping rate by avoiding the averaging procedure.

Furthermore we plan to further refine the computational procedure in order to estimate the Seebeck coefficient and fully characterize the thermoelectric zT figure of merit.

Finally we plan to characterize the micromorphological features of PEDOT by exploiting coarse graining approaches using the same polymerization algorithm.